

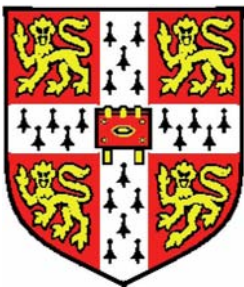
Physical phenomena of thin surface layers

Katherine Ruth Thomas

Supervisor

Prof. Dr. Ullrich Steiner

A dissertation submitted for the degree of Doctor of Philosophy
July 2010



University of Cambridge
Cavendish Laboratory
Wolfson College

Declaration

This dissertation is the result of my own work and includes nothing which is the outcome of work done in collaboration except where specifically indicated in the text. I declare that no part of this work has been submitted for a degree or any other qualification at this or any other university. This dissertation does not exceed the word limit of 60,000 words set by the Physics and Chemistry Degree Committee.

Katherine R. Thomas. July 2010

Abstract

Physical phenomena of thin surface layers – *Katherine R. Thomas*

This thesis explores different physical phenomena observed in, or involving thin surface films. Thin surface layers are ubiquitous. Found in nature and used in almost every aspect of daily life, thin surface films are invaluable. While the applications and roles may be varied, to be used effectively, the physical properties of these films and the factors influencing their stability need to be well understood.

Surfaces can have a strong effect on the stability of thin films. In thin films of polymer blends, wetting layers rich in one component often form at the film interface prior to phase separation. Here the formation of these wetting layers are seen to result in destabilisation of the film, even when the blend is far from phase coexistence. A spinodal like instability with a characteristic wavelength is shown to form. A theoretical model is developed, which describes the observed behaviour in terms of coupled height and composition fluctuations in the wetting layer.

Spin coating is a common technique for the formation of thin polymer films. Films formed in this way however, are often seen to exhibit anomalous properties, which strongly differ from that of the bulk behaviour of the material. Here the rheological properties and stored stresses in spin cast films are explored, with focus on the role that the casting solvent plays in the properties of the film. The results suggest that the observed deviation comes from a lowered density of chain entanglements. The effective viscosity and residual stresses in the as-spun film are seen to strongly depend on the casting solvent properties and the solvent-polymer interactions.

The use of organometallic polymers as precursors for the formation of magnetic ceramics is investigated. Emphasis is placed on doping the polymers with metallic compounds prior to pyrolysis, allowing for the formation of technologically interesting metallic alloys, without the need for new polymers to be synthesised. The formation of iron-palladium alloys is demonstrated using this method. These are highly desirable due to their potential use in hard-disk drive technologies.

Thin films can be used to influence the optical signature of a material and are widely used in nature to produce vibrant, pure, iridescent colours. Here the optical properties of the tropical plant *Selaginella willdenowii* are explored. The bright blue colouration is seen to arise from a multilayer lamella structure on the upper surface of the leaves. Light is important to plants, who use it both as an energy source and an environmental signal. Blue iridescence occurs in a wide range of plant species, suggesting that it has some adaptive benefit. These are considered and discussed.

Acknowledgements

This thesis is a result of work carried out in the Thin Films and Interfaces at the Cavendish Laboratory, University of Cambridge and was funded through a studentship from the Engineering and Physical Sciences Research Council.

I would like to start by thanking my supervisor Prof. Ullrich Steiner, whose knowledge, enthusiasm, advice and support guided me throughout my research. I would particularly like to thank Ulli for allowing and encouraging me to take a three month sabbatical to undertake a research project in industry. The opportunity was invaluable. Not all supervisors would have been so understanding or relaxed about my absence.

My thanks goes to all members of the Thin Films and Interfaces group past and present for their help, friendship and support both in and out of the lab. To Alexis Chennievre who worked with me for 3 months during his masters project on the electrohydrodynamic instabilities, in particular on vapour annealing of the films. To Rosa Poetes for all her help and advice with the ellipsometric measurements. To Natalya Yufa and Silvia Vignolini who proofread large parts of this manuscript. To Maik Scherer for solving all my LaTeX problems. And to Mathias Kolle who helped amongst other things, with the optical measurements of the ferns.

Imaging in its different forms was an important part of the work carried out in this thesis and could not have been achieved without the help of a number of people. I would like to thank Chrissie Prichard and Jeremy Skepper for their help and advice on embedding the ferns for TEM imaging. JJ Rickard for the many hours spent with me trying every possible technique to get the best image possible of the ferns. Richard Langford and Eric Tapley for your help with FIB milling.

I was fortunate to have enthusiastic, unstinting input from several external collaborators, without whom parts of the story told here would have been incomplete. Dr. Nigel Clarke at the University of Durham, whose model was modified to explain the behaviour seen in the polymer blends. Dr. Heather Whitney and Dr. Beverley Glover at the department of Plant sciences for providing the biological perspective on the role that iridescence might play in tropical ferns.

To my parents who have always been there for me. Thank you for your constant support and encouragement in everything I have done; I would not have made it here without it. To my sister and best friend Anne, for your unique perspective on life and for keeping me sane. Hugs and waves. To Sam.

CONTENTS

1	Introduction	1
2	Theoretical Background	5
2.1	Polymer blends	6
2.1.1	Flory-Huggins theory	6
2.2	Thin film stability	10
2.2.1	Van der Waals forces and the Hamaker constant	15
2.3	Stability of polymer blend thin films	16
2.4	Electrohydrodynamic instabilities	20
3	Wetting induced instabilities in miscible polymer blends	25
3.1	Materials and methods	28
3.2	Optical properties of the pure polymers	33
3.3	Results	35
3.3.1	Surface enrichment	36
3.3.2	Surface instabilities	40
3.4	Conclusions	46
4	Out of equilibrium dynamics of thin polymer films	49
4.1	Materials and methods	56
4.1.1	Optical observation of instabilities	61
4.2	Results and discussion	64
4.2.1	Toluene	64
4.2.2	Trans-decalin	70
4.2.3	Chloroform, MEK and THF	77
4.2.4	Vapour annealing	81

4.3	Conclusions	84
5	Residual stress in thin polymer films	87
5.1	Materials and methods	89
5.2	Results and discussion	90
5.2.1	Cantilever bending	93
5.3	Conclusions	97
6	Palladium doped polymer precursors for magnetic ceramics	99
6.1	Materials and methods	102
6.2	Results	107
6.3	Discussion	116
6.4	Conclusions	120
7	Iridescence in tropical ferns	121
7.1	Introduction	124
7.2	Theoretical Background	128
7.2.1	A single interface	128
7.2.2	A single thin film on a substrate	130
7.2.3	Multilayer reflections	131
7.3	Materials and Methods	132
7.4	Results	137
7.4.1	Modelling	141
7.5	Discussion	144
7.6	Possible adaptive advantages of iridescence	147
7.7	Conclusions	150
8	Conclusions	153
	Bibliography	161
	List of publications	183

INTRODUCTION

This thesis is formed of a number of projects all with the common theme of surfaces and thin films. The variety of projects is a result of three main factors. Firstly that I chose to take an internship sabbatical half way through my PhD, secondly that I had and took the opportunities to collaborate with a wide variety of different scientists and finally that everything worked (well almost)!

Thin surface films or layers are ubiquitous. Found both in nature and in many technological applications, thin surface films have a wide variety of different roles. They can influence the optical signature of a surface; a thin film with the right properties coated onto the surface of a sheet of glass can act as an antireflective coating, reducing the glare from reflected sunlight. They can act as lubricants protecting objects from wear, such as those found on the surface of our eyes which act to nourish and protect the cornea. Another example is as memory devices where thin magnetic films are used for data storage.

While the applications and roles may be varied, to be used effectively the physical properties of these films need to be well understood. This thesis explores the physical phenomena of a number of different thin films and can broadly be divided into three

Physical phenomena of thin surface layers

areas. The first looks at the stability of thin polymer films. The stability of a thin film is important when considering its application, where a uniform homogenous film is required, for example a layer of paint on the wall, it would be undesirable if the film were to rupture and break-up. For a butterfly caught in the rain however, it is important that a continuous film of water does not form on its wings, weighing it down, but instead breaks up into droplets which will easily fall off.

Polymer blend films are often unstable, when taken from the one phase region to the two phase region of phase space, due to phase separation of the different components. In these films the surfaces can have a strong effect on the microstructure evolution within the film during phase separation. Wetting layers rich in one component are often seen to form at the film interfaces prior to phase separation [1] and can lead to novel segregation within the film [2, 3]. These wetting layers are also seen to form when the films are in the one phase region of phase space [4]. In chapter 3, the formation of wetting layers at temperatures far from phase coexistence are seen to result in the spontaneous destabilisation of the film, causing a roughening of the polymer/air interface. The blend is still in the one phase regime and no phase separation is seen to occur. A spinodal like instability develops with a characteristic wavelength, which is dependent on the composition of the blend. A theoretical description of the destabilisation is developed, which explains the experimental results in terms of the hydrodynamics of the film taking into account coupled height and concentration variations within the wetting layer which forms.

Dewetting of a film is often undesirable. However, if the break up of a film can be carefully controlled then the mechanisms causing this break up and the properties of the film can be probed. In thin polymer films, electric fields can be used to drive destabilisation of the surface, resulting in the formation of a well defined pattern [5]. The wavelength of this pattern is defined by the force balance acting on the film, while the onset of the instabilities is dependent on the rheological properties of the film. Experiments have shown that there is a discrepancy between the exper-

imentally observed growth of these instabilities and that predicted theoretically [6]. It is thought that this may arise from non-equilibrium conformations of the polymer chains and residual stresses in the film due to the preparation procedure [7]. In chapter 4 the effect of casting solvent on the properties of films formed by spin coating is considered. The effective viscosity and the residual stresses of the as-spun film are seen to be strongly dependent on the properties of the casting solvent and the solvent-polymer interactions. The results show that the processing conditions of the film are critical in determining the rheological properties and the conformation of the polymer chains in the film. In chapter 5 the feasibility of using focused ion beam milling to study the overall magnitude of the stresses in as-cast films polymer films is investigated. This is done using a cantilever deflection technique, where the cantilevers are milled into polymer films supported on silicon nitride membranes. The initial experiments show that this technique is indeed feasible and indicate high residual stresses in as-cast films.

The second phenomenon of thin films explored in this thesis is the use of polymer films to form magnetic ceramics. Thin magnetic films are important in many technological applications and can be used as sensors and for data storage. The use of polymers as the precursors to the ceramics allows for the easy incorporation of metallic nanoparticles into the films prior to ceramatisation and for the possible fabrication of complex and nanostructured shapes not possible with other film formation methods. A popular class of polymer to use as precursors are ferrocenes due to the desirable magnetic properties of the resulting ceramics [8]. In chapter 6 one such polymer polyferrocenylethylmethylsilane is doped with palladium prior to pyrolysis and ceramic formation. The crystalline structure and the magnetic properties of the resulting ceramics are investigated. Synthesis of new polymers can be an expensive and time consuming process. Here instead palladium is mixed into the polymer, either through the addition of nanoparticles or directly as acetyl acetonate, allowing iron-palladium containing ceramics to be formed. Iron-palladium alloys are highly

Physical phenomena of thin surface layers

desirable due to their potential use in next generation hard-disk drives.

The final physical phenomena of thin films discussed in this thesis, is the use of thin films to influence the optical signature of a material. Optically active structures occur widely in nature and often result in the production of vibrant, pure, iridescent colours [9]. Generally observed in insects and birds, optical structures are also seen in plants but have not been as widely studied and as a result are poorly understood. Plants use light both as an energy source for photosynthesis but also as an environmental signal and are able to respond to its intensity, wavelength and direction. One plant which displays iridescence is *Selaginella willdenowii* and is found growing in the understorey of the Malaysian rainforests. The plant leaves are seen to display a bright blue colouration. In chapter 7 the structures causing this colouration are investigated and the role that the iridescence might have to play in the plant discussed.

THEORETICAL BACKGROUND

Polymers are long chain flexible molecules that consist of repeating molecular units known as monomers. Due to the diversity of their properties both naturally occurring and synthetic polymers are used in almost every aspect of modern day life. On the molecular level polymers can be considered as chains, where the chain is not completely stretched but has a coil-like conformation. If the polymer is made up from a single type of monomer then it is known as a homopolymer. Polymers can also be formed from different monomers, with copolymers containing two chemically different monomers and terpolymers containing three. Polymers are formed during a process known as polymerisation where each monomer is covalently bonded to the next. The properties of the polymer depend on a number of parameters, including the monomer used, the chain length, the distribution of the chain length (known as the polydispersity) and purity. This chapter focuses on the theoretical description of the stability of polymer blends and of thin polymer films.

2.1 Polymer blends

Binary polymer blends are mixtures that consist of two chemically different polymer species; polymer A and polymer B. The behaviour of a blend is determined by the interactions between the two polymers. Entropic interactions always act to promote mixing of the two components. Enthalpic interactions can however, act to promote or inhibit mixing depending on the monomer-monomer interactions.

In polymer mixtures the entropy of mixing is very small due to the long chains of the molecules involved. Miscibility of the polymers can therefore occur when the enthalpic interactions between the two polymers are favourable. Miscibility can also occur when the enthalpic contribution is unfavourable, if it is smaller in magnitude than the entropy of mixing. The monomer-monomer interactions are dependent on a number of factors, including temperature and composition. As a result polymer blends can exhibit both miscibility (homogeneous, one phase behaviour) and immiscibility (heterogeneous, two phase behaviour) depending on these parameters.

2.1.1 Flory-Huggins theory

A model for the thermodynamic compatibility of polymer blends was developed by Flory [10] and Huggins [11] independently in the 1940's. The Flory-Huggins lattice model is a mean field theory that considers both the combinatorial entropy of mixing and the enthalpic interactions between the monomers. The model assumes a mixture of n_A chains consisting of N_A units of polymer A and n_B chains consisting of N_B units of polymer B. The polymer chains are arranged randomly on a periodic lattice. Each unit is assumed to be identical in size and occupies only one site.

The entropy of the system can be found by considering the total number of states of the system and is determined using the Boltzmann relation $S = k \ln \Omega$, where Ω is the number of ways the molecules can be arranged on the lattice. The resulting

expression for the entropy of mixing for a binary blend is given by

$$\Delta S_{\text{mix}} = -k_B \left[\frac{\phi_A}{N_A} \ln \phi_A + \frac{\phi_B}{N_B} \ln \phi_B \right] \quad (2.1)$$

where $\phi_{A,B}$ is the fraction of sites occupied by monomers of polymer A or B and k_B is the Boltzmann constant. The $1/N$ factor arises from the fact that the monomers are covalently bonded in groups of N , which cannot be independently dispersed. This shows the strong influence of the chain length on the entropy of mixing and the miscibility of polymer blends.

The enthalpic energy of the system depends on the monomer-monomer pair interaction. In the model, this is assumed to come only from nearest-neighbour interactions; identical and nonidentical monomer-monomer interactions. The enthalpy of mixing is given by

$$\Delta H = k_B T \chi \phi_A \phi_B \quad (2.2)$$

where χ is the dimensionless Flory-Huggins interaction parameter. Flory and Huggins considered χ to be purely energetic in origin varying as T^{-1} . This implies that for phase separation to occur the temperature of the blend must be lowered. However, phase separation is also seen to occur in some blends upon heating. Therefore χ must also have an entropic contribution arising from packing constraints on the level of polymer segments such that

$$\chi_{\text{th}} = A + \frac{B}{T} \quad (2.3)$$

where A and B are constants, which vary from blend to blend. In classic Flory-Huggins theory the interaction parameter is assumed to be independent of the volume fractions of the two polymers. Experimentally however, it has been seen that the interaction parameter can have a strong compositional dependence [12–14]. Here a compo-

Physical phenomena of thin surface layers

sition dependent interaction parameter is used with the form

$$\chi(T, \phi) = \left(C_1 - \frac{C_2}{T} \right) (1 - C_3 \phi_A) \quad (2.4)$$

where C_1 , C_2 and C_3 are constants. The total free energy of the system F_{th} can now be written using equations 2.1 and 2.2

$$\frac{F_{\text{th}}}{k_{\text{B}}T} = \frac{\phi_A}{N_A} \ln \phi_A + \frac{\phi_B}{N_B} \ln \phi_B + \chi(T, \phi) \phi_A \phi_B \quad (2.5)$$

The entropic contribution to equation 2.5 is always negative, while the enthalpic contribution can be either positive (opposes mixing) or negative (promotes mixing) depending on the value of χ .

The Flory-Huggins free energy can be used to interpret the phase space of polymer mixtures and to theoretically predict changes in the mixing behaviour such as the coexistence or binodal curve. This is normally done using the common tangent approach. The free energy vs. composition is plotted as a function of the temperature (see figure 2.1a). If the free energy is partially concave, a line can be drawn that is tangent to F_{th} and intercepts the curve in two places. These give the coexistence compositions at that temperature. For a more detailed discussion see [15]. The binodal curve defines the boundary between the one phase and two phase regions in phase space and gives the equilibrium composition of the coexisting phases. The temperature at which the phase boundary disappears defines the critical point. If this extremum is a maximum then the system is said to have an upper critical solution temperature (UCST), while if it is a minimum then the system has a lower critical solution temperature (LCST) (figure 2.1b).

The spinodal curve defines the limit of metastability; the region enclosed by the spinodal is unstable while the region between the binodal and spinodal is metastable. Equilibrium is reached slowly in polymer melts. For a blend heated to just inside the

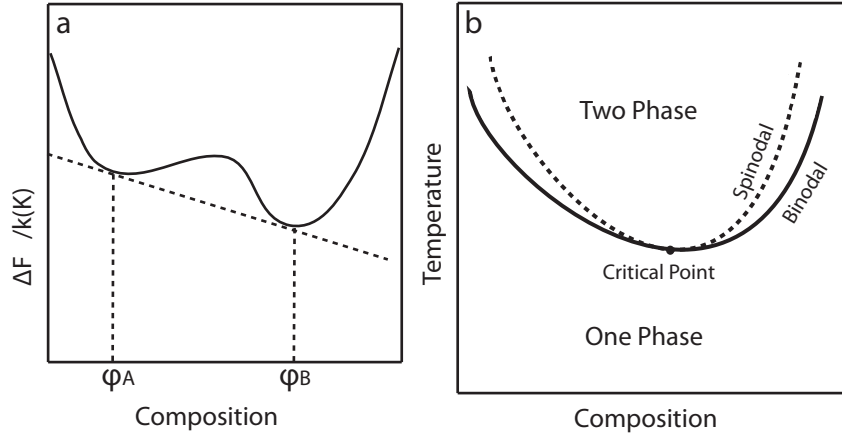


Figure 2.1: (a) Common tangent construction. (b) Example phase diagram for a lower critical solution blend.

two-phase region (between the spinodal and binodal curves), phase-separation occurs via nucleation and growth; droplets of one phase form inside a matrix of another slowly at discrete sites. If the temperature quench is deeper into the two phase region (inside the spinodal region), then it becomes favourable for the system to phase separate spontaneously; phase separation occurs uniformly throughout the material. The spinodal defines the boundary between the two regimes of phase separation.

The binodal, spinodal and critical point can be found from equation 2.5 by considering the stability, equilibrium criteria and criticality.

- Binodal

$$\frac{\Delta F_{\text{th}}(\phi_A) - \Delta F_{\text{th}}(\phi_B)}{\phi_A - \phi_B} = \left(\frac{\partial \Delta F_{\text{th}}}{\partial \phi} \right)_{\phi_A} = \left(\frac{\partial \Delta F_{\text{th}}}{\partial \phi} \right)_{\phi_B} \quad (2.6)$$

- Spinodal

$$\frac{\partial^2 \Delta F_{\text{th}}}{\partial \phi^2} = 0 \quad (2.7)$$

- Critical Point

$$\frac{\partial^3 \Delta F_{\text{th}}}{\partial \phi^3} = 0 \quad (2.8)$$

2.2 Thin film stability

Thin liquid surfaces are never completely flat. Due to thermal motion of the molecules a spectrum of capillary waves is always present. However, liquid films are in general stable, since a sinusoidal perturbation of any given wavelength will result in an increase in the surface area of the film and therefore an increase in the free energy of the system. For the film to become unstable an additional “destabilising” force must act at the surface of the film. This force can take on a number of different forms including van der Waals forces (section 2.2.1), surface-tension forces, temperature gradient effects [16, 17] and forces due to external fields such as an applied electrostatic pressure (section 2.4). In this case the film can lower its free energy by changing its thickness and is therefore unstable.

The stability of thin liquid films on solid substrates has been widely studied both theoretically and experimentally [18–22]. The main stages of instability formation and dewetting in thin films are generally well understood. The process of instability formation can be modelled using a hydrodynamic approach where the thin liquid film is approximated as an incompressible fluid. The motion of the fluid is then described using the Navier-Stokes description of fluid flow with the appropriate boundary conditions. The equations of motion are linearised by assuming that variations in the height are small compared to their lateral extent (linear stability theory). The stability of the film is determined by whether these fluctuations grow or decay over time. The resulting system of equations can be reduced to a simple description for the time and spatial dependence of the height of the film, which can be used to determine the conditions for instability formation. Pattern development and the dynamics of the instabilities can be followed by studying these equations numerically.

This approach has been used to model a variety of systems such as the dewetting of polymer films on solid substrates [21, 22], the formation of instabilities in two-layer liquid films [23] and the stability of films due to density variations [24]. Sharma *et al.*

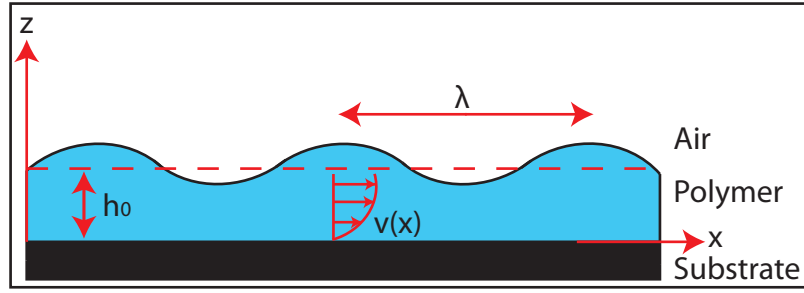


Figure 2.2: Schematic representation of capillary surface instabilities.

have shown that if the density of a film decreases with increasing film thickness, a thermodynamically stable film can become unstable [24].

At temperatures above the glass transition temperature polymers can be described as incompressible viscous fluids. Figure 2.2 shows a schematic representation of a thin liquid film supported on a solid substrate. The local variation in height $h(x, t)$ of the polymer film at the polymer/air interface can be described by a one dimensional sinusoidal function

$$h(x, t) = h_0 + \xi \exp(iqx + t/\tau) \quad (2.9)$$

where h_0 is the average thickness of the film, ξ and q are the amplitude and wavevector of the fluctuations respectively, t is the time and x the lateral coordinate parallel to the surface. The time constant τ determines the temporal evolution of each fluctuation with wavevector q . For positive values of τ the surface is destabilised by an amplification of this mode, while negative values of τ correspond to damping. The wavelength λ of the fluctuations is assumed to be large compared to the film thickness such that $\lambda = 2\pi/q \gg h_0$ and the amplitude much smaller than h_0 .

The formation of a surface wave requires the lateral displacement of liquid within the film. The velocity profile within the film can be determined using the Navier-Stokes equation of motion for an incompressible Newtonian fluid.

$$\rho(\partial_t v + (v \cdot \nabla)v) = -\nabla p + \eta \nabla^2 v + \rho g \quad (2.10)$$

Physical phenomena of thin surface layers

This equation determines the liquid transport within the film, where v and η are the velocity and viscosity of the liquid, ∇p is the pressure gradient, which drives the liquid flow in the film, g is the gravitational acceleration and ∂_i is the partial derivative with respect to i . The right hand-side of equation 2.10 gives the total force acting on a small volume element moving in the fluid. This force stems from the pressure gradient, viscous forces and gravity.

The polymer films considered in chapter 4 have very high viscosities, which results in a low fluid flow. As a result the convective term $(v \cdot \nabla)v$ in equation 2.10 can be neglected. The slow dynamic means that the velocity profile can always be considered to be in a quasi-steady state ($\partial_t v = 0$). Finally in thin films gravity is negligible. Equation 2.10 can now be simplified to give

$$-\nabla p + \eta \nabla^2 v = 0 \quad (2.11)$$

The following assumptions are made about the thin liquid film. Firstly, a no-slip boundary condition is assumed $v(z=0) = 0$ at the film/substrate interface; there is no liquid motion relative to the substrate. Secondly that normal stresses at the interface are absent $\eta \partial_z v_{\text{liquid}} = 0$. Taking these into account the velocity profile of the film is

$$v(z) = \frac{1}{2\eta} z(z-2h) \partial_x p \quad (2.12)$$

The averaged flux due to the lateral flow through a cross-section h of the film is given by

$$j = h\bar{v} = \int_0^h v(z) dz = \frac{h^3}{3\eta} \partial_x p \quad (2.13)$$

where \bar{v} is the mean velocity. The continuity equation of the non-volatile liquid film assuming incompressibility and taking into account mass-conservation is

$$\partial_t h + \partial_x j = 0 \quad (2.14)$$

The equation of motion of the film/air interface can then be found by inserting equation 2.13 into equation 2.14.

$$\partial_t h = \frac{1}{3\eta} \partial_x (h^3 \partial_x p) \quad (2.15)$$

Here, p is the overall pressure acting at the surface of the liquid film. This is given by

$$p = p_0 - \gamma \partial_{xx} h + p_{\text{ex}}(h) \quad (2.16)$$

where p_0 is the atmospheric pressure and γ is the surface tension. The second term represents the Laplace pressure acting on the film, which stems from the curvature of the interface. $p_{\text{ex}}(h)$ is any excess surface pressure acting on the film.

Substituting the expression for the overall pressure acting at the surface into equation 2.15 along with equation 2.9, the dispersion relation for the system relating the time constant τ to the wavevector q for a sinusoidal perturbation of the film can be found using linear stability analysis [25].

$$\frac{1}{\tau} = -\frac{h_0^3}{3\eta} [\gamma q^4 + \partial_h p_{\text{ex}}] \quad (2.17)$$

The dispersion relation can be used to determine whether a wave with wavevector q is damped or amplified. This is shown in figure 2.3. In the absence of, or for a positive excess pressure gradient ($\partial_h p_{\text{ex}} \geq 0$) all growth rates are negative, the fluctuations will be damped due to the restoring effect of surface tension. As discussed earlier, the film will act to minimise its surface area, damping all perturbations. This is indicated by the dashed line in figure 2.3. When $\partial_h p_{\text{ex}} < 0$ (solid line in figure 2.3) long wavelength fluctuations with $0 < q < q_c = \sqrt{-\partial_h p_{\text{ex}}/\gamma}$ are amplified and the film will become unstable, while short wavelength fluctuations are damped.

The fastest growing mode q_{max} is given by the maximum of equation 2.17,

$$q_{\text{max}}^2 = \frac{-1}{2\gamma} \partial_h p_{\text{ex}} \quad (2.18)$$

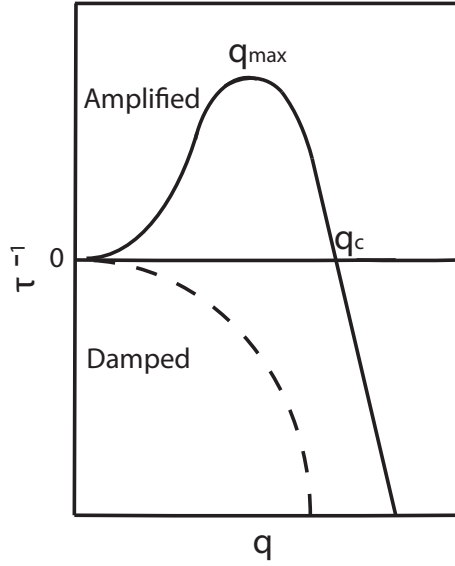


Figure 2.3: Graphical representation of the dispersion relation. In the absence of an applied external field, all fluctuations are damped (dashed line). For a finite external pressure, fluctuations are amplified. The dispersion relation yields a dominant mode q_{\max} with a corresponding growth rate τ_{\max}^{-1} .

the characteristic wavelength by:

$$\lambda_{\max} = 2\pi \sqrt{\frac{-2\gamma}{\partial_h p_{\text{ex}}}} \quad (2.19)$$

and the maximal growth rate by:

$$\frac{1}{\tau_{\max}} = \frac{\gamma h_0^3}{3\eta} q_{\max}^4 \quad (2.20)$$

This is proportional to the surface tension and inversely dependent on the viscosity of the liquid.

Equations 2.19 and 2.20 together can be used to describe the static and dynamic behaviour of the liquid film. The characteristic wavelength is a signature of the forces acting on the liquid-air interface, while the time constant and growth rate can be used to probe the rheological behaviour of the liquid film.

2.2.1 Van der Waals forces and the Hamaker constant

Van der Waals forces are an attractive or repulsive force, which acts between atoms or molecules. They stem from polarisation effects between permanent and/or induced dipoles. For two isolated atoms, the resulting force is proportional to the inverse sixth power of the distance between the atoms [26]. This is known as the London equation. Van der Waals forces exist not only between atoms and molecules but also between particles and condensed media. These forces can be used to explain the dewetting (break-up) of thin polymer films and wetting layers [27].

Consider a layer of thickness h sandwiched between two semi-infinite media. The van der Waals forces between these media, give rise to an interaction free energy per unit area of the form [28]

$$f_{\text{vdw}} = -\frac{A}{12\pi h^2} \quad (2.21)$$

where A is the effective Hamaker constant. The Hamaker constant determines the interaction between the media and can be found using the Lifshitz theory [28]. The Lifshitz theory is a continuum theory, which describes the van der Waals interactions in terms of the dielectric properties of the media. The Hamaker constant for two semi-infinite media 1 and 2, interacting across a layer 3, is approximated as

$$A \approx \frac{3}{4}kT \left(\frac{\varepsilon_1 - \varepsilon_3}{\varepsilon_1 + \varepsilon_3} \right) \left(\frac{\varepsilon_2 - \varepsilon_3}{\varepsilon_2 + \varepsilon_3} \right) + \frac{3h_p v_e}{8\sqrt{2}} \frac{(n_1^2 - n_3^2)(n_2^2 - n_3^2)}{(n_1^2 + n_3^2)^{1/2} (n_2^2 + n_3^2)^{1/2} \left\{ (n_1^2 + n_3^2)^{1/2} + (n_2^2 + n_3^2)^{1/2} \right\}} \quad (2.22)$$

where ε_1 , ε_2 and ε_3 are the dielectric permittivities and n_1 , n_2 and n_3 are the refractive indices of the three media, h_p is Plank's constant and v_e is the main electronic absorption frequency in the ultra-violet, which is typically around $3 \times 10^{15} \text{ s}^{-1}$. The first term of equation 2.22 is the zero-frequency energy of the van der Waals interaction and the second term is the dispersion energy contribution.

In thin films of polymer blends, surfaces can have a strong effect on the microstructure evolution within the film during phase separation. On quenching of the films

from the one phase region to the two phase region of the phase diagram, wetting layers rich in one component of the polymer blend are often seen to form at the film interfaces [1]. The formation of these layers can lead to novel segregation within the films [2], with simultaneous phase separation and dewetting being observed [3]. In chapter 3 equation 2.22 is used to calculate the Hamaker constant for a system where media 1, 2 and 3 are the bulk polymer/polymer blend, air and a wetting layer rich in poly(vinyl methyl ether) respectively. The first term in equation 2.22 is found to be on the order of -4.5×10^{-23} J. This is three orders of magnitude smaller than the second term in equation 2.22, which is on the order of -1×10^{-20} J. The first term is therefore ignored.

When $n_1 > n_3 > n_2$, as in chapter 3, the Hamaker constant is negative. This results in a repulsive van der Waals force, which tends to increase the thickness of layer 3 in order to lower the free energy. This repulsive or negative pressure in relation to van der Waals forces is known as the disjoining pressure and can lead to a destabilisation of the layer and the formation of instabilities due to the presence of an excess surface pressure as shown earlier. The $1/h^2$ dependence of the van der Waals free energy s_{vdw} (equation 2.21), signifies that the van der Waals forces are long-range forces and act significantly over distances of up to 10 nm.

2.3 Stability of polymer blend thin films

In chapter 3, the formation of instabilities at the polymer/air interface in miscible polymer blends is discussed. In such a system it is not enough to describe the stability only in terms of fluctuations in the height; composition fluctuations also play an important role and must be considered. There have been many studies into the behaviour of thin films of binary blends. However, all of these studies have been carried out at the coexistence temperature or on films that are quenched deep into the two phase region of the phase diagram where simultaneous phase separation and

dewetting are observed [3].

The mechanisms of instability formation and dewetting in thin films of polymer blends, differ to that of single component films. In blends of deuterated oligomeric styrene and oligomeric ethylene-propylene quenched into the two phase region, phase separation is seen to induce dewetting of the films [29]. Holes are observed to form first at the edges of the film and then move inwards. The rupture of the films occurs on a faster time scale than that seen in single component films and has different morphological characteristics. Evolving gradients in the concentration of the two components at the surface of the film induce surface tension gradients, which provide an additional flow in the decomposition/dewetting front. It is thought that this is responsible for the accelerated hole formation observed [30].

The formation of wetting layers in polymer blends, where one component preferentially segregates to the polymer/air interface, prior to phase separation can induce material heterogeneities and surface tension gradients in the films. These surface tension gradients influence the hydrodynamics and mass transfer within the film and are important when considering the destabilisation of these systems [30–32].

In a study by Clarke [33, 34], the stability of thin polymer blend films subject to coupled height and composition fluctuations was investigated. He showed that such a film will be less stable than one where either height or composition fluctuations are considered in isolation. While this study focuses on films quenched in the two phase region of the phase diagram, it was proposed that a thin film heated at temperatures corresponding to the bulk one-phase region may also become unstable when these coupled fluctuations are considered. A modified version of this model is used in chapter 3 to describe the instabilities observed. For completeness the original model is explained here.

The model considers the coupling between surface-driven instabilities and composition instabilities in a thin film on a flat solid substrate with a free upper surface. The following assumptions and conditions are applied. For simplicity fluctuations in

Physical phenomena of thin surface layers

composition are only allowed in the plane parallel to the substrate. For the model to be physically realistic, the system of equations must conserve the total volume and the relative amount of each component in the blend. The condition for fluctuations in height and composition must correspond to the thermodynamic criteria based on the free energy of the system. The model also assumes incompressibility; there is no variation in the total density throughout the film. The total free energy of the film is given by

$$F_T = \int \left\{ f_b[\phi(\mathbf{x})]h(\mathbf{x}) + f_s[\phi(\mathbf{x}), h(\mathbf{x})] \right\} d\mathbf{x} \quad (2.23)$$

where \mathbf{x} is the two-dimensional vector within the plane. $f_b[\phi(\mathbf{x})]$ is the volume fraction dependent free energy per unit volume within the film, which is independent of height; since composition fluctuations are only allowed in the plane parallel to the substrate, all unit volumes with coordinate \mathbf{x} have the same composition. The total local free energy in the bulk is therefore proportional to the height $h(\mathbf{x})$ of the film with respect to the substrate. $f_s[\phi(\mathbf{x}), h(\mathbf{x})]$ is the surface free energy per unit area, which is dependent on the composition and the local height.

The model then considers the effect of perturbations in the composition $\phi(\mathbf{x})$ and height $h(\mathbf{x})$ about their average values ϕ_o and h_o . The perturbations have the form

$$\phi(\mathbf{x}) = \phi_o + \delta\phi(\mathbf{x}) \quad (2.24)$$

$$h(\mathbf{x}) = h_o + \delta h(\mathbf{x}) \quad (2.25)$$

Substituting the above into equation 2.23, gives the total free energy to be

$$F_T = \int f_b[\phi_o + \delta\phi(\mathbf{x})](h_o + \delta h(\mathbf{x})) d\mathbf{x} + \int f_s[\phi_o + \delta\phi(\mathbf{x}), h_o + \delta h(\mathbf{x})] d\mathbf{x} \quad (2.26)$$

The bulk and surface free energies to the second order in the perturbations are

$$f_b \approx f_b(\phi_o) + \frac{\partial f_b}{\partial \phi} \delta\phi(\mathbf{x}) + \frac{1}{2} \frac{\partial^2 f_b}{\partial \phi^2} [\delta\phi(\mathbf{x})]^2 \quad (2.27)$$

$$f_s \approx f_s(\phi_o, h_o) + \frac{\partial f_s}{\partial \phi} \delta\phi(\mathbf{x}) + \frac{1}{2} \frac{\partial^2 f_s}{\partial \phi^2} [\delta\phi(\mathbf{x})]^2 + \frac{\partial f_s}{\partial h} \delta h(\mathbf{x}) + \frac{1}{2} \frac{\partial^2 f_s}{\partial h^2} [\delta h(\mathbf{x})]^2 + \frac{\partial^2 f_s}{\partial h \partial \phi} [\delta h(\mathbf{x})][\delta\phi(\mathbf{x})] \quad (2.28)$$

The conditions of volume and material conservation require that $\int \delta h(\mathbf{x}) \, d\mathbf{x} = 0$ and $\int (\phi_o + \delta\phi(\mathbf{x}))(h_o + \delta h(\mathbf{x})) \, d\mathbf{x} = B\phi_o h_o$, where B is the area of the film being considered. These two conditions combine to give

$$\int \delta\phi(\mathbf{x})\delta h(\mathbf{x}) \, d\mathbf{x} = -h_o \int \delta\phi(\mathbf{x}) \, d\mathbf{x} \quad (2.29)$$

the constraint for coupled height and composition fluctuations.

In order to determine the condition for instability formation, the free energy change due to small sinusoidal spontaneous fluctuations of the form

$$\delta\phi(\mathbf{x}) = \delta\phi_o + \delta\phi_1 \sin\left(\frac{\pi x_1}{L}\right) \sin\left(\frac{\pi x_2}{L}\right) \quad (2.30)$$

$$\delta h(\mathbf{x}) = \delta h_1 \sin\left(\frac{\pi x_1}{L}\right) \sin\left(\frac{\pi x_2}{L}\right) \quad (2.31)$$

are considered. $B = 2L \times 2L$ is the area of the film, where L is much greater than the correlation length associated with gradients in the free energy. In a system where height and composition fluctuations are not coupled, the condition for instability formation is that the second derivative of the free energy with respect to height or composition fluctuations is negative. This means that the free energy decreases due to the fluctuations.

Considering equations 2.27, 2.28, 2.29 and 2.30, the total free energy has the form

$$F_T = F_o - \pi^2 f' \delta\phi_1 \frac{\delta h_1}{h_o} + \pi^2 f''_{\phi} \delta\phi_1^2 \left(1 + \frac{\delta h_1^2}{4h_o^2}\right) + \pi^2 f''_h \delta h_1^2 \quad (2.32)$$

where

$$f' = \left[\frac{\partial f_s}{\partial \phi} - h_o \frac{\partial^2 f_s}{\partial h \partial \phi} \right], \quad f''_{\phi} = \frac{1}{2} \left(h_o \frac{\partial^2 f_b}{\partial \phi^2} + \frac{\partial^2 f_s}{\partial \phi^2} \right), \quad f''_h = \frac{1}{2} \frac{\partial^2 f_s}{\partial h^2} \quad (2.33)$$

For the free energy to decrease with respect to a flat uniform film for some fluctuation

Physical phenomena of thin surface layers

$\delta\phi_1 \delta h_1$, the curvature of the free energy must be somewhere negative.

The film is able to lower its total free energy by coupled height and composition fluctuations if

$$f''^2 > 4h_o^2 f''_{\phi} f''_h \quad (2.34)$$

This shows that even when both the second derivatives with respect to height and concentration are positive the film may become spontaneously unstable, as long as the surface free energy is concentration dependent. In this situation, coupled phase separation and height variations are the only route to reduce the free energy.

Equation 2.34 gives the condition for instability formation in a thin film binary mixture. The implications for stability when the mixture is miscible can now be considered. The model assumes that composition fluctuations only occur in two dimensions; layers do not form parallel to the substrate. In many polymer blends however, layering at the polymer/air interface is often seen due to surface enrichment by one component. This surface segregation acts to lower the free energy of the film, which according to this model can only serve to reduce the stability of the film. Equation 2.34 is then sufficient for the film to become unstable.

The model clearly shows that the coupling of height and composition fluctuations is important when considering the stability of polymer blend films and provides a starting point for modelling the dynamics of these systems.

2.4 Electrohydrodynamic instabilities

The formation of so-called electrohydrodynamic (EHD) instabilities, which develop when a thin liquid film is sandwiched between two conductive media in a capacitor like device, have been widely studied [6, 25, 35, 36]. Placing a liquefied insulator in a plate capacitor geometry and applying an electric field perpendicular to the liquid/air interface causes an amplification of low amplitude capillary surface waves,

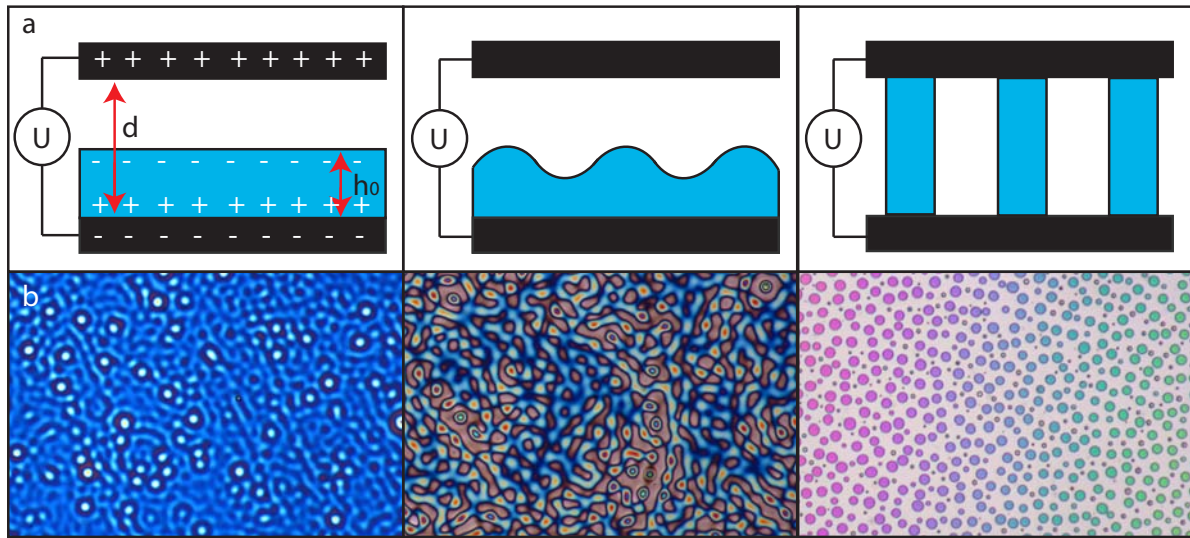


Figure 2.4: (a) Schematic representation of the capacitor setup used for the generation of instabilities in thin films by electric fields. The amplification of a surface instability is triggered by applying a voltage U . With time this instability grows causing the formation of liquid columns which span the two plates. (b) Optical images of instabilities observed in a polystyrene film.

due to the presence of a destabilising surface excess pressure. EHD instabilities develop with a characteristic wavelength λ . These instabilities then grow until fully formed columns span the electrodes (figure 2.4). The physical mechanisms describing the induced deformation of a liquid surface by an applied electric field, were first noted by Swan in 1897 [37]. Since then many investigations have been carried out on this type of system and the theory behind EHD instabilities is well understood [25, 38–40].

There are two main reasons behind the popularity in this approach for thin-film destabilisation. The first, is as a method of pattern replication [6, 41–43]. When a homogeneous force acts at the films surface, the resulting pattern will have a characteristic wavelength, but will be laterally random. However, if a lateral variation in the force field is introduced, for example by patterning the top electrode, the pattern formation process can be guided to form a well defined structure (figure 2.5). Faithful replication of the electrode pattern can be achieved with lateral dimensions down to 100 nm [5] and on timescales of a few seconds [36] depending on the properties of the liquid film.

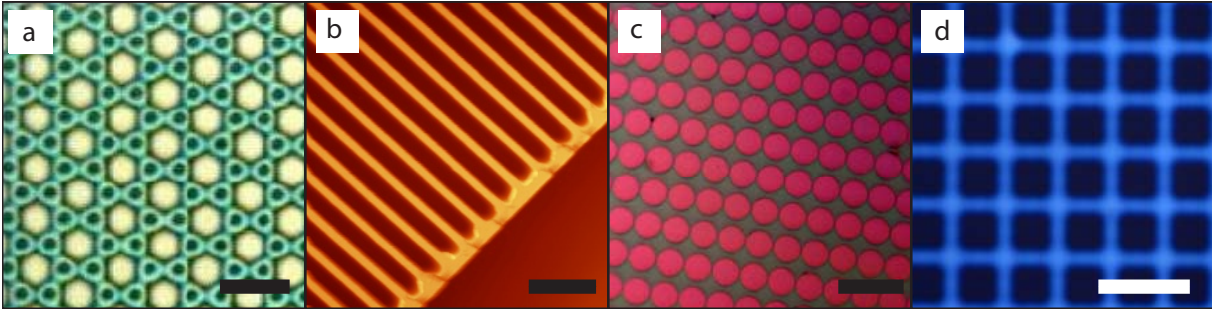


Figure 2.5: Electrohydrodynamic pattern replication using structured top electrodes. (a) Double-hexagonal pattern. (b) Lines are 140 nm wide and 140 nm high. (c) Circular columns. (d) Square columns. Scale bars (a) 5 μm , (b) 1 μm , (c) 20 μm , (d) 10 μm . Images taken from [25], [36] and [45].

The second use of this method of destabilisation is as a sensitive measurement technique to quantitatively deduce the balance of forces at the liquid interface [44] and the intrinsic physical properties of the liquid film. Barbero *et al.* [7] have shown that by weakly perturbing the surface of a thin liquid film using an applied electric field, the rheology and dynamics of the film can be probed. This will be discussed further in chapter 4.

In the presence of an applied electric field equation 2.16 becomes

$$p = p_0 - \gamma \partial_{xx} h + p_{\text{dis}}(h) + p_{\text{el}}(h) \quad (2.35)$$

where p_{dis} is the disjoining pressure, which results from intermolecular forces exerted on the thin film. These include van der Waals interactions as discussed in section 2.2.1 and play a role in near surface regions. p_{el} is the destabilising pressure, for an applied voltage U , exerted on the interface by the interaction of the electric field with the polarisation charges induced at the interface. If the liquid is a perfect dielectric in a capacitor, the charges at the liquid/air interface experience an attractive interaction with the charges on the upper electrode. The electrostatic pressure at the liquid/air interface is given by

$$p_{\text{el}} = -\epsilon_0 \epsilon_p (\epsilon_p - 1) E_p^2 = \epsilon_0 \epsilon_p (\epsilon_p - 1) \frac{U^2}{[\epsilon_p d - (\epsilon_p - 1)h]^2} \quad (2.36)$$

where ε_0 is the permittivity of free space, ε_p is the dielectric constant of the liquid polymer, d is the capacitor spacing and U is the applied voltage. Only the Laplace term and the electrostatic pressure need to be taken into account due to the strong electric fields generated in the system. The characteristic wavelength can be found by substituting equation 2.36 into equation 2.19

$$\lambda_{\max} = 2\pi \sqrt{\frac{-2\gamma}{\partial_h p_{\text{el}}}} = 2\pi \sqrt{\frac{\gamma U}{\varepsilon_0 \varepsilon_p (\varepsilon_p - 1)^2} E_p^{-3/2}} = 2\pi \sqrt{\frac{\gamma [\varepsilon_p d - (\varepsilon_p - 1)h]^3}{\varepsilon_0 \varepsilon_p (\varepsilon_p - 1)^2 U^2}} \quad (2.37)$$

and the characteristic onset time for instability formation is given by equation 2.20

$$\tau_{\max} = \frac{\eta}{\gamma h_0^3} \left(\frac{\lambda_{\max}}{2\pi} \right)^4 \quad (2.38)$$

From these two equations it can be seen that the time dependence of instability formation is strongly dependent on the thickness of the film and the pressure gradient. It is also dependent on the viscosity of the liquid film and the surface tension.

WETTING INDUCED INSTABILITIES IN MISCIBLE POLYMER BLENDS

The composition of polymer blends at the surface and in the bulk often differs due to the preferential adsorption of one component [1]. Driven by differences in surface energies, the lower surface tension component is seen to segregate to the surface, enriching the polymer/air interface [4, 46–48]. In miscible polymer blends this surface enrichment is seen to be dependent on the molecular weights of the blend constituents and the overall blend composition, with the width of the enriched wetting layer being on the order of the correlation length ξ [49]. As the critical temperature of the blend is approached ξ increases [50] and the width of the surface layer grows rapidly [51].

Thin liquid films are easily deformed by material heterogeneities or thermal fluctuations [52]. The interaction of the polymers with the free surface plays an important role in the type of instability observed when thin films of polymer blends are quenched from a homogeneous state to an unstable state in the two phase regime [53]. When one component is preferentially attracted to the polymer/air interface, surface-directed spinodal decomposition waves evolve at this surface, propagating into the

Physical phenomena of thin surface layers

bulk, with wave vectors normal to the interface [54]. On quenching of the system, the rapid formation of a surface enriched layer occurs prior to phase separation, inducing material heterogeneities and surface tension gradients within the film. Surface tension gradients have a strong influence on the hydrodynamics and mass transfer within fluid systems [30–32], resulting in Marangoni-type flows within the film. The liquid layer becomes unstable as a consequence of normal and lateral composition gradients, giving rise to surface undulations.

Lateral surface modes can also evolve in the presence of neutral surfaces, which do not have a preference for either polymer [30, 32, 55, 56]. These modes are similar to those for energetically biased interfaces but have a much smaller amplitude than spinodal decomposition waves, making them hard to resolve.

Blends of polystyrene (PS) and poly(vinyl methyl ether) (PVME) exhibit a lower critical solution temperature (LCST) [57–60]. They offer an ideal system for the study of the wetting behaviour of polymer blends due to their miscibility across all blend compositions and strong segregation of PVME to the air surface. Investigations using two-dimensional nuclear magnetic resonance (NMR) suggest that this miscibility results from a weak van der Waals interaction between the PS phenyl ring and the PVME methoxy group, giving rise to a weakly negative interaction parameter [61, 62]. As the temperature of the blend is increased, this interaction is weakened and phase separation of the blend occurs [63].

The miscibility of PS/PVME blends can be influenced by a number of parameters, including the solvent in which the two polymers are initially mixed [64], the molecular weights of the polymers [65, 66], the film thickness [67] and through cross-linking of the polymer chains [68]. For the majority of studies, PS/PVME blends are cast from toluene solutions. Films produced in this way are homogeneous for all compositions at room temperature. Trichloroethylene is also a common solvent for PS and PVME. For films cast from trichloroethylene, the homogeneity of blends is seen to be dependent on the volume fraction of the two polymer components [64]. Homogenous

films are observed at room temperature for $\phi_{\text{ps}} < 0.25$ and heterogenous films for $0.4 < \phi_{\text{ps}} < 0.97$, where ϕ_{ps} is the volume fraction of PS in the blend. Films with composition $0.25 < \phi_{\text{ps}} < 0.4$ and $\phi_{\text{ps}} > 0.97$ have 'slight' heterogeneities. The homogeneous films were found to have the same phase separation or cloud point temperature as films cast from toluene.

In the one phase regime, PVME exhibits a strong surfactant behaviour and is seen to wet the polymer-air interface [69, 70]. Bhatia *et al.* [4] showed, using X-ray photoelectron spectroscopy (XPS) measurements, that a pure PVME wetting layer of 5–7 nm thickness forms at the polymer/air interface. The surface enrichment of the PVME is dependent on the molecular weights of the polymers and the overall blend composition.

Extensive work has been carried out on the phase separation of weakly miscible polymer blends [67, 71–73]. Thin films of the blend were reported to undergo phase separation induced by composition fluctuations [74]. Ogawa *et al.* studied the evolution of 200 nm thick films heated at 115 °C, which is in the two phase region for that blend. They observed delayed dewetting of the films. During this incubation period, the PVME was seen to segregate to the surface, while phase separation occurred in the bulk. They suggest that the dewetting was induced by composition fluctuations during the incubation period.

A further property of PS/PVME blends that has attracted a lot of attention is the homogeneity of the blends at room temperature. Differential scanning calorimetry (DSC) measurements have shown that PS/PVME blends exhibit a single glass transition temperature T_g , which is dependent on the composition of the blends [75]; this is indicative of a homogeneous blend. However, other experiments carried out using NMR spectroscopy and electron spin resonance oppose this view [76, 77]. They show that on the scale of the polymer segments, for temperatures in the one phase region but above T_g , the PS/PVME blends are not completely mixed. The blends are neither strictly homogenous nor phase separated but instead microheterogeneous [75, 78, 79].

This chapter focuses on previously unreported instabilities observed at the polymer/air interface, which develop spontaneously in PS/PVME polymer blend thin films in the one-phase regime, at temperatures well below their cloud point temperature. Optical microscopy and atomic force microscopy were used to observe the surface evolution of the films, while the changes in wetting behaviour were analysed using ellipsometry.

3.1 Materials and methods

Polystyrene (PS) $M_w = 100 \text{ kg mol}^{-1}$, $M_w/M_n = 1.04$ and poly(vinyl methyl ether) (PVME) 50 wt.% H_2O , were both obtained from Sigma-Aldrich. The PVME was dried in a vacuum oven at 60°C for 48 hrs and then placed under vacuum in a desiccator containing phosphorous pentoxide (P_2O_5) for a further 24 hrs. Measurements of the PVME before and after the dehydration process showed a mass loss of 50% confirming that all the water had been removed. The molecular weight $M_w = 78 \text{ kg mol}^{-1}$ and polydispersity $M_w/M_n = 2.43$ of the PVME were determined using gel permeation chromatography. Solutions with various PS:PVME ratios in toluene were prepared and filtered through a $0.1 \mu\text{m}$ PTFE filter.

Cloud point measurements

Cloud point measurements were obtained by measuring the intensity of reflected light at normal incidence as a function of temperature using an Ocean Optics USB 4000 spectroscope and DHL bal 2000 lightsource. The experimental setup is shown in figure 3.1a. This technique was chosen due to the high resolution of the measurements. As blends are heated and phase separation starts to occur, domains of one phase start to form in a matrix of another phase. Once these domains become large enough they start to scatter the low wavelength light of the incident lightsource. This reduces the reflected intensity at normal incidence for this wavelength and a decrease

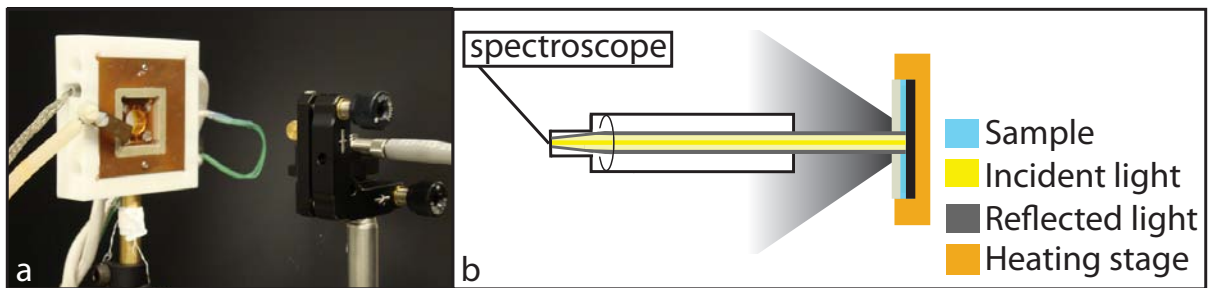


Figure 3.1: (a) Photograph of spectroscopic setup. (b) Schematic representation of (a).

in the overall intensity of reflected light from the baseline reflectance is observed. As the domains grow, longer and longer wavelengths are scattered and the intensity of reflected light at normal incidence decreases further.

Films of 10 μm thickness were prepared by blade coating a 20% w/w toluene solution of the blend onto cleaned silicon substrates. The films were heated for 24 hrs at 60 $^{\circ}\text{C}$ under vacuum and then covered with a polydimethylsiloxane (PDMS) coated glass cover slip to prevent air coming into contact with the blend. The sandwiched films were heated in the optical set-up from 75 $^{\circ}\text{C}$ to 130 $^{\circ}\text{C}$ at a rate of 0.5 $^{\circ}\text{C}/\text{min}$.

Films of 215 ± 10 nm thickness of the blends with varying PVME volume fraction ϕ were prepared by spin coating (3000 rpm for 45 s) 5% w/w toluene solutions onto cleaned silicon wafers. All samples were prepared in a nitrogen glove box and used immediately. Optical measurements of the cloud point temperature were carried out using the same heating parameters as above. Films were imaged during heating using an Olympus GX51 inverted microscope coupled to a CCD digital camera. The optical measurements of cloud point temperatures were found to be $\sim 20^{\circ}\text{C}$ higher than the spectroscopic cloud point measurements. This is due to the lower dynamic range of the microscopy set-up as compared to the reflectivity set-up.

Dynamic mechanical thermal analysis

The cloud point temperature was also measured using a Triton Technology DMTA (figure 3.2a). Dynamic mechanical thermal analysis (DMTA) allows the measurement of the mechanical properties of a material, such as the modulus or stiffness, as a func-

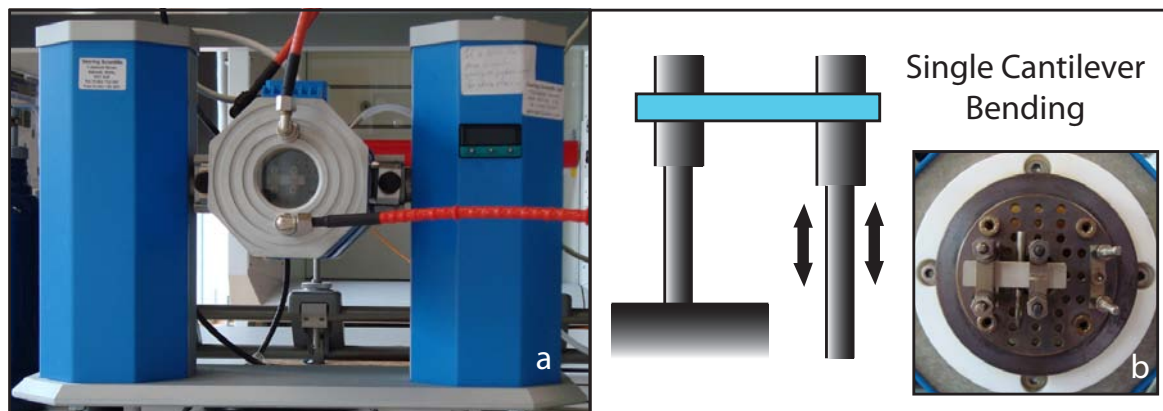


Figure 3.2: (a) Photograph of Triton Technology DMTA. (b) Schematic representation and photograph of the sample holder.

tion of the temperature. For these measurements, a specimen of known geometry is subjected to a sinusoidal stress and the strain in the material is measured. This allows the complex modulus of the material to be determined.

DMTA is a useful technique for characterising polymers as it can capture their viscoelastic behaviour. For purely elastic materials Hooke's law applies i.e. the strain is proportional to the applied stress. In this case the stress is independent of the strain rate; the applied stress and the measured strain are in phase with one another. For purely viscous or Newtonian materials, the stress is proportional to the strain rate. For these materials, there is a 90° phase difference between the applied stress and the measured strain. Viscoelastic materials such as polymers behave somewhere in between and some phase difference will be measured.

DMTA measures the stiffness and damping, these are reported as the modulus and $\tan \delta$. The modulus is expressed as the storage modulus (in-phase elastic component) and the loss modulus (out of phase viscous component). The ratio of the loss modulus to the storage modulus is known as $\tan \delta$ and is a measure of the energy dissipation of the material.

The DMTA was used to measure two properties of the polymer blends; the glass transition temperature and the demixing temperature. The glass transition gives rise

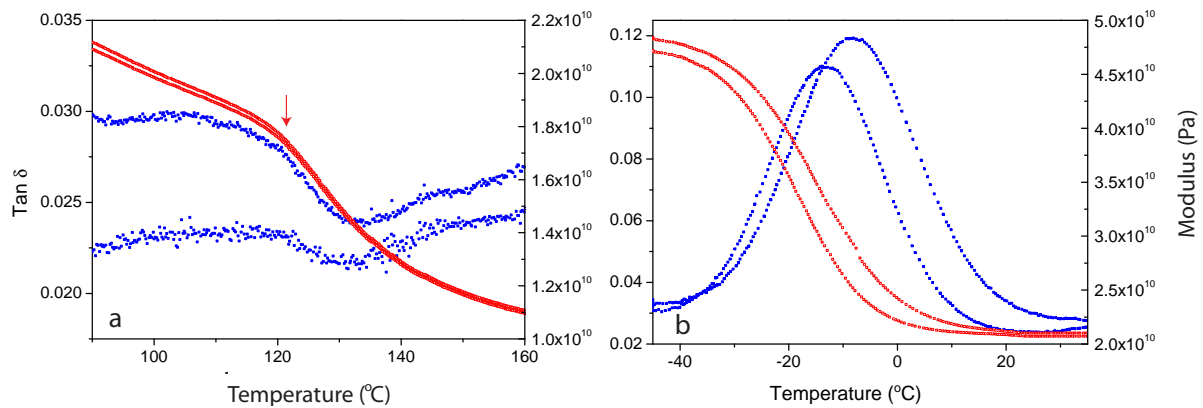


Figure 3.3: DMTA traces showing (a) cloud point temperature for $\phi = 0.3$ (b) glass transition temperature for $\phi = 0.5$.

to a large drop in the storage modulus and a peak in $\tan \delta$. The position of this peak is dependent on the frequency of the applied stress. Phase separation is observed by a change in the storage modulus and $\tan \delta$. The position of this peak is frequency invariant [80].

Blend samples of 3 – 5 mg of material were prepared in a glovebox and used immediately. A heating rate of 1 $^{\circ}\text{C}/\text{min}$ was used. The DMTA was used in single cantilever bending mode with frequencies of 1 and 10 Hz. The size of the sample holder was 10 mm \times 5 mm \times 0.5 mm. This heating rate is greater than that used than for the other two techniques due to limitations of the apparatus.

Figure 3.3 shows example traces for the DMTA measurements. All blends were seen to exhibit a single glass transition temperature, which was dependent on the blend composition (figure 3.3b). The demixing temperature of the blends was found to be greater than the cloud-point temperatures measured using reflection spectroscopy partly due to the higher heating rate and the lower resolution of the apparatus. Figure 3.3a shows an example temperature scan for a blend with $\phi = 0.3$.¹ The demixing temperature is indicated by the arrow.

¹ ϕ indicates the PVME content of the blend.

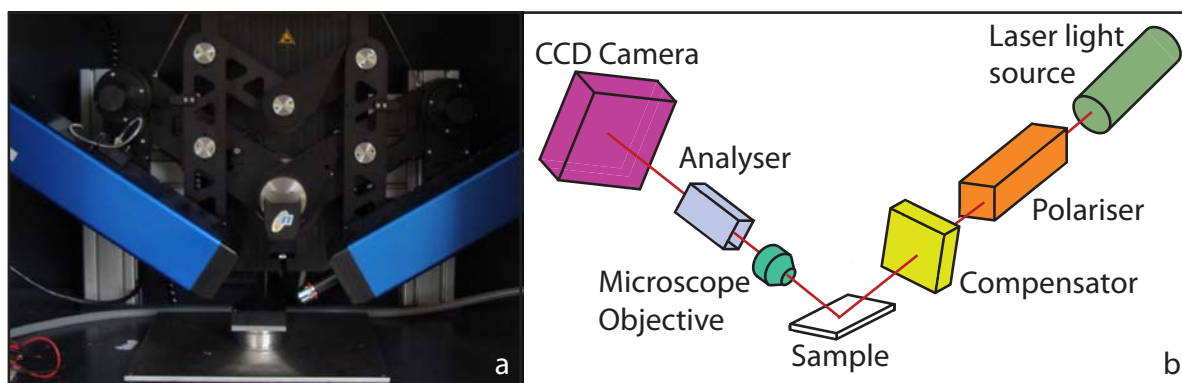


Figure 3.4: (a) Photograph of ellipsometer. (b) Schematic diagram of ellipsometer showing positions of analyser, compensator and polariser.

Ellipsometry

To monitor surface evolution and wetting, films were first heated at $T_1 = 70^\circ\text{C}$ ($\phi = 0.6, 0.7$) or $T_1 = 75^\circ\text{C}$ ($\phi = 0.3, 0.4, 0.5$) for 45 min, followed by heating at 10°C below the cloud point temperature T_{cp} : $T_2 = T_{\text{cp}} - 10^\circ\text{C}$. Temperature measurements were accurate to $\pm 1^\circ\text{C}$. Wetting behaviour was monitored with an EP3 nulling imaging ellipsometer (Nanofilm, Germany), while surface evolution was monitored using a Veeco Dimension 3100 atomic force microscope (AFM) (see section 4.1.1).

The thickness, refractive index and depth profile of the blend films were found using a model-dependent fit to the ellipsometry data. For these measurements, films were prepared and annealed in a glove box. Ellipsometric measurements were then carried out in air. Ellipsometry is a standard method for the determination of optical constants and thicknesses of polymer films on reflecting surfaces. It can also be used to study more complicated systems and is able to resolve the interfaces between polymer layers [81–83]. Unlike some other methods [84], ellipsometry allows for the modelling of the composition across the entire thickness of the film.

Ellipsometry works by measuring the change in polarisation of light upon reflection from the interfaces of thin transparent films. A schematic diagram of the ellipsometer can be seen in figure 3.4b. All nulling ellipsometers are based on six components: a light source, a rotating polariser, a compensator, a sample, a rotating anal-

yser and a detector. The angles of the polariser, compensator and analyser at the null condition are related to the ellipsometric quantities Δ and Ψ , where $\tan(\Psi)$ is the amplitude ratio of the parallel and perpendicular components of the polarised light on reflection from the surface and Δ is the phase difference. The optical properties of the film cannot be deduced directly from Δ and Ψ . Instead the optical properties are found through comparison of the measured data with computational models of Δ_{model} and Ψ_{model} allowing the properties of the film, for which the modelling data best matches the experimental data, to be found.

Measurements with four zone accuracy were performed at a wavelength of 532 nm, using a diode-pumped solid state laser, while varying the angle of incidence from 45° to 60°. A $200 \times 200 \mu\text{m}^2$ area was chosen as the region of interest for the measurements. Care was taken to exclude local defects and dust. Each measurement lasted about 45 min due to the time required for rotation of the polariser, analyser and compensator between the four zones. Analysis was carried out for the film as spun, after heating at $T = T_1$ for 45 min and after heating at $T_2 = T_{\text{cp}} - 10^\circ\text{C}$. Repeat measurements showed no further changes.

The film thickness and surface roughness were measured using a Veeco Dimension 3100 atomic force microscope (AFM) in tapping mode. The use of atomic force microscopy will be discussed in chapter 4.

3.2 Optical properties of the pure polymers

Reliable ellipsometric measurements require optical characterisation of the substrate and the film materials. The bare silicon substrate was measured and modelled in terms of the optical constants of bulk silicon, with a refractive index $n_{\text{Si}}(532 \text{ nm}) = 4.15$ and an extinction coefficient $k_{\text{Si}} = 0.01$, covered by a native silicon oxide layer with $n_{\text{SiO}_x} = 1.5$, $k_{\text{SiO}_x} = 0$ and $d_{\text{SiO}_x} = 2 \text{ nm}$. These parameters were kept fixed for all further measurements. Films of pure PVME and PS were spin-cast onto cleaned

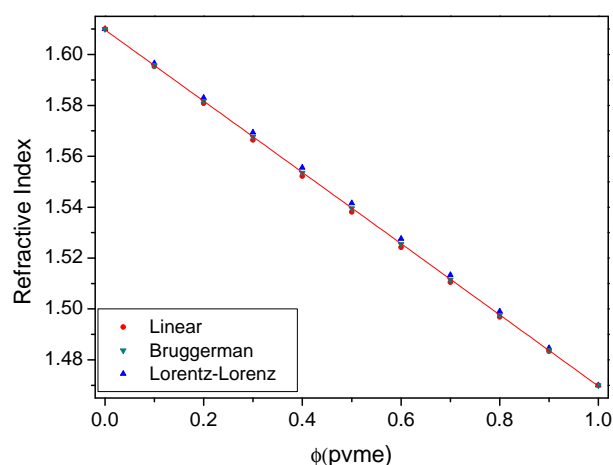


Figure 3.5: Variation of refractive index with blend composition as predicted using the linear, Bruggeman and Lorentz-Lorenz effective medium models. The line is a guide for the eye.

silicon wafers and their thickness d and refractive index n were determined before and after annealing at T_1 for 45 min. For PS, n was seen to increase and d to decrease slightly with annealing. The properties of the PVME film remained unchanged.

Since the initial measurements were performed directly after spin coating, the changes in PS properties are likely to be caused by residual solvent in the film, resulting in a lower refractive index and a slightly swollen film. Upon heat treatment this solvent is lost and the properties of pure PS are recovered. Additional heat treatment resulted in no further changes in the refractive index or thickness of either film.

The refractive indices for the PS and PVME were found to be 1.61 and 1.47 respectively ($k = 0$ for transparent polymers). This compares to 1.60 [85] and 1.467 [86] in the literature. Based on these refractive indices, measured values of n for PS/PVME blends were converted into PVME volume fractions ϕ by linear interpolation, which closely approximates the Lorentz-Lorenz and Bruggeman effective medium approximations for refractive index (figure 3.5) [87–89].

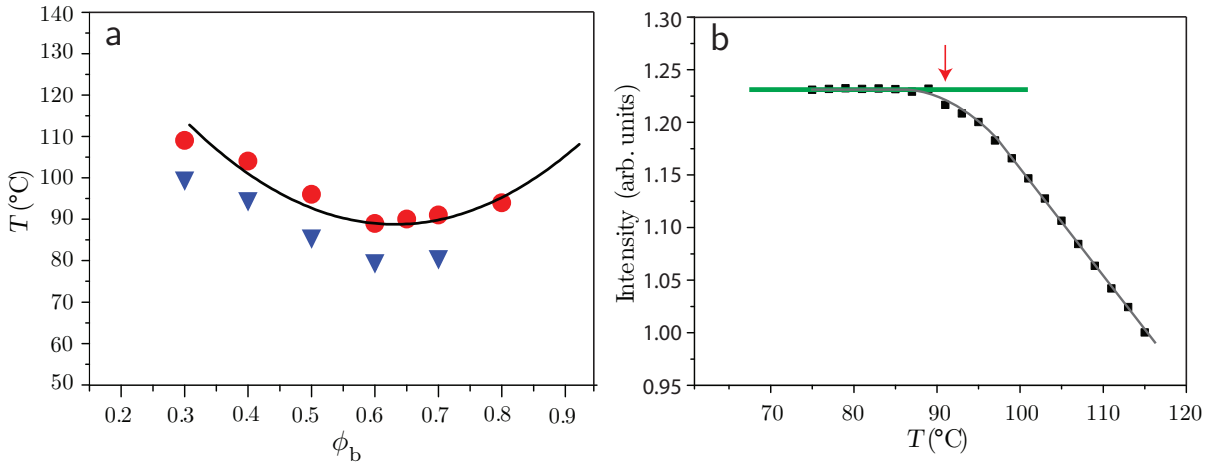


Figure 3.6: (a) Coexistence curve for the PS/PVME blends. The circles are data from light reflectivity experiments. The line is a fit using the common-tangent construction of the Flory-Huggins free energy. The triangles indicate the temperatures at which surface instabilities were observed. (b) Intensity of the reflected light as a function of temperature for $\phi = 0.6$. T_{cp} is indicated by the arrow. The grey line is a guide for the eye.

3.3 Results

The cloud point curve for the bulk PS/PVME blend is shown in figure 3.6a. The cloud point temperature T_{cp} , as measured by reflectivity, was taken to be the temperature at which the intensity of reflected light first started to decrease from the baseline intensity (figure 3.6b).

The experimental data were modelled by minimising the Flory-Huggins free energy

$$f_b = \frac{\phi}{N_A} \ln \phi + \frac{1-\phi}{N_B} \ln(1-\phi) + \chi\phi(1-\phi) \quad (3.1)$$

using the well established common-tangent technique (section 2.1.1), where N_A and N_B are the degree of polymerisation of PVME and PS respectively. For this blend a χ -parameter with a weak linear ϕ -dependence [14] is commonly used:

$$\chi(T, \phi) = (C_1 - C_2/T)(1 - C_3\phi) \quad (3.2)$$

The parameters $C_1 = 0.0222$, $C_2 = 7.32$ K and $C_3 = 0.4$ were determined by fitting the

calculated binodal to the data in figure 3.6a. This yields the critical temperature for the blend of $T_c = 89 \pm 1$ °C at a PVME volume fraction of $\phi_c = 0.63 \pm 0.05$.

The literature reports wide-ranging lower critical solution temperatures for blends with molecular weight of PS and PVME similar to those used in this study [14, 57, 58, 90]. Nishi *et al.* [57] found $T_c \sim 100$ °C for $M_w(\text{PS}) = 110$ kg mol⁻¹ and $M_w(\text{PVME}) = 51.5$ kg mol⁻¹, while Qian *et al.* found $T_c \sim 120$ °C for $M_w(\text{PS}) = 100$ kg mol⁻¹ and $M_w(\text{PVME}) = 75$ kg mol⁻¹ [14]. PVME is known to be highly hygroscopic and the presence of water can affect the thermodynamics of phase separation. The lower value of T_c found here possibly arises from the great care that was taken to ensure that the PVME and PVME containing blends were water-free at all times. Repeat experiments showed highly reproducible results for the determination of the coexistence curve.

3.3.1 Surface enrichment

Three individual ellipsometric measurements and surface roughness measurements were carried out for five blend compositions. The temperature protocol was as follows: the films were measured as spun, after heating at T_1 for 45 min and after heating at T_2 for 45 min. Figure 3.8 shows data for these three different measurements for a film with $\phi = 0.6$.

Each data set was initially fitted to three different models: a uniform film, a film with a wetting layer and a film with a roughened wetting layer. These three models are shown in figure 3.7. The fit to model C in figure 3.7 was comparable to that of model B. AFM surface roughness measurements, showing a roughness of $\sigma < 1$ nm for all films after these heating times, confirmed the absence of significant surface roughness (figure 3.11a). Based on these observations, only model A and B were used to analyse the data.

Initially the data are fitted well by assuming a film of uniform composition with $d = 224$ nm and $n = 1.538$ (figure 3.8a). Heating the film at T_1 for 45 min did not change

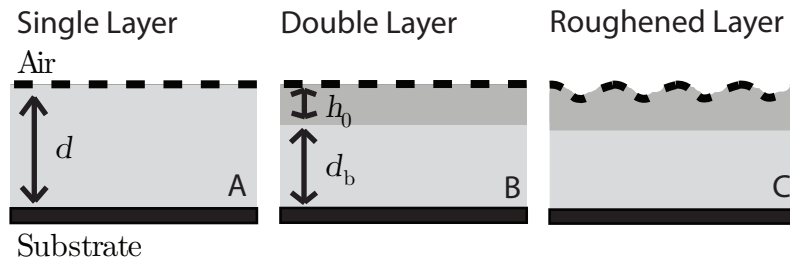


Figure 3.7: Schematic diagram of the models used to fit the ellipsometric data. (a) Uniform film (single layer). (b) PVME enriched surface layer (two layer model). (c) Roughened PVME surface layer (three layer model).

the fitted d and n values, indicating the absence of residual solvent in the PVME rich film. The fitted values from the two layer model converge to a single layer model with $n = n_b = n_s$ where n_b is the refractive index of the bulk layer and n_s is the refractive index of the surface layer and did not improve the quality of the fit.

The film was then heated at $T_2 = 80^\circ\text{C}$ for 45 min. The ellipsometric angles of the data in figure 3.8c are no longer well described by a single layer fit. Instead, a double layer model with $d_b = 208\text{ nm}$, $n_b = 1.529$, $h_0 = 19\text{ nm}$ and $n_s = 1.482$ provides a much better fit to the data. An AFM topography image of the surface showed no sign of surface roughness, indicating that the resulting changes must be due to a wetting layer, not to a roughening of the polymer/air interface (figure 3.11a). The lower refractive index of the wetting layer indicated an increased PVME content at the surface as compared to the bulk. A detailed analysis of the fit parameters was consistent with material conservation with respect to the initial uniform film.

Similar measurements were carried out for all the blend compositions indicated in figure 3.6a and the trend in sample composition with temperature was confirmed. As-cast and films annealed at $T = T_1$ could be fitted by a single layer model, while films heated at $T = T_2$ for 45 min were all best described by a two layer model with a PVME enrichment layer of $h_0 = 21 \pm 3\text{ nm}$ and a reduced refractive index as compared to the bulk.

The thickness of the PVME surface enrichment layer can be compared to the bulk correlation length of PS/PVME blend for $T = T_2$. The correlation length is both com-

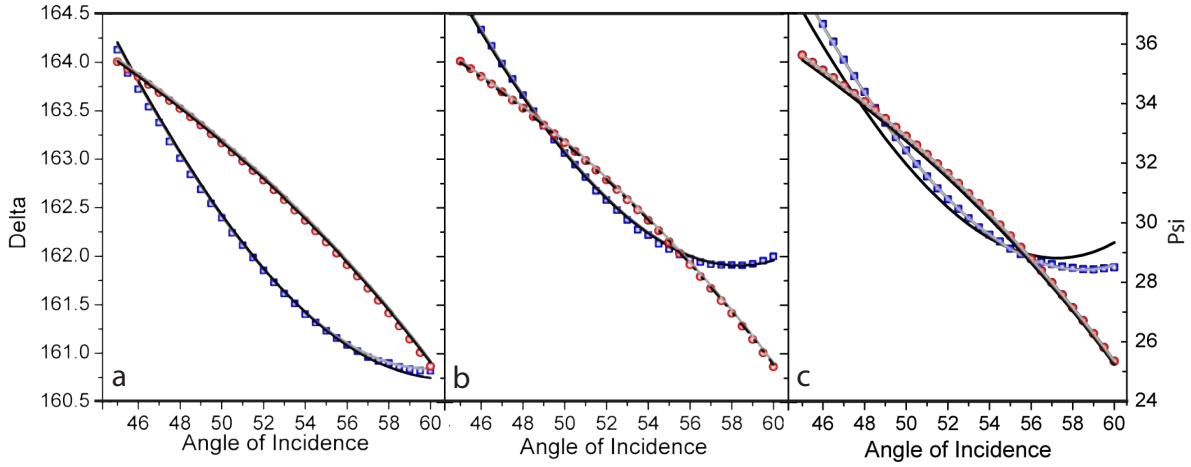


Figure 3.8: Variation of the ellipsometric angles Delta (\square) and Psi (\circ) with the angle of incidence for a sample with $\phi = 0.6$. The lines are fits to the data for a uniform film composition (black lines) and a film with a PVME-rich surface layer (grey lines). (a) Film as spun. Single layer fit: $d = 224 \pm 7$ nm, $n = 1.538$. Double-layer fit: $d_b = 207 \pm 8$ nm, $n_b = 1.528$ and $h_0 = 20 \pm 10$ nm, $n_s = 1.515$. (b) Film heated at 70°C for 45 min. Single layer fit: $d = 224 \pm 7$ nm, $n = 1.535$. Double layer fit: $d_b = 207 \pm 7$ nm, $n_b = 1.535$ and $h_0 = 22 \pm 3$ nm, $n_s = 1.538$. (c) Film heated at 80°C for 45 min. Single layer fit: $d = 228 \pm 8$ nm, $n = 1.517$. Double layer fit: $d_b = 208 \pm 8$ nm, $n_b = 1.529$ and $h_0 = 19 \pm 2$ nm, $n_s = 1.482$.

position and temperature dependent [91].

$$\xi = \frac{a}{6} \sqrt{\frac{1 - \phi_b}{2N_A} + \frac{\phi_b}{2N_B} - \chi(T, \phi)\phi_b(1 - \phi_b)} \quad (3.3)$$

where a is the statistical segment length [92] and ϕ_b is the bulk composition sufficiently far from the surface. The correlation length varies from 19 ± 2 nm for $\phi = 0.3$ to 20 ± 2 nm for $\phi = 0.4 - 0.6$ and 18 ± 2 nm for $\phi = 0.7$. Within the error margins, the fitted width of the PVME enrichment layer is identical to the bulk correlation length of the blend, in agreement with mean field theories.

Figure 3.9a shows the variation of the normalised surface excess as a function of ϕ_b

$$z^* = \frac{a}{6} \int_{\phi_s}^{\phi_b} d\phi \sqrt{\frac{(1 - \phi)}{f_b(\phi) - f_b(\phi_b) - (\phi - \phi_b)\Delta\mu}} \quad (3.4)$$

where ϕ_s is the surface composition and $\Delta\mu$ is the chemical potential difference between blends with ϕ_b and ϕ_s [93]. The insets show the composition profile for $\phi = 0.3$

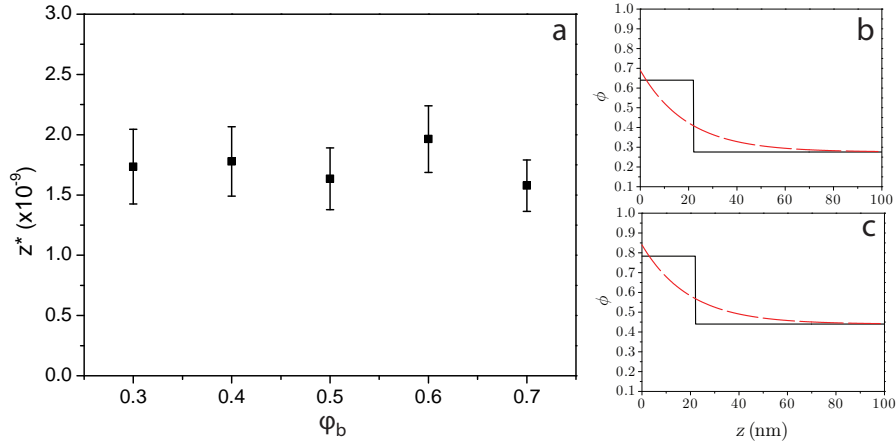


Figure 3.9: (a) Variation of the surface excess with ϕ after annealing for 45 min at $T_2 = T_{cp} - 10^\circ \text{C}$. Composition profile of blends with overall blend composition (b) $\phi = 0.3$ and (c) $\phi = 0.5$. All surface layers have the same thickness of $h_0 = 21 \pm 3 \text{ nm}$. The solid line shows the ellipsometric model and the broken line prediction of equation 3.5.

(figure 3.9b) and $\phi = 0.5$ (figure 3.9c). The squares show the experimental surface excess based on the ellipsometric step model fit to the wetting layer (solid line in figure 3.9b, c). The ellipsometric model is however only the most simple approximation for the surface enriched layers. Mean field models predict an exponential variation of the composition at the surface

$$\phi(z) = \phi_b + (\phi_s - \phi_b) \exp(-z/\xi) \quad (3.5)$$

The predictions of equation 3.5 are shown in figure 3.9 (broken lines) alongside the step profiles (solid lines). Both models have the same values of z^* .

To improve the ellipsometric model, a series of step functions can be used to better approximate the predicted exponential variation of z^* . Adding a third layer to the model resulted in fits with a top layer of $\phi \simeq 1$. This is in agreement with published values for the PVME surface enrichment of 98% [4, 69] and leaves z^* , h_0 and ϕ_b essentially unchanged. Since this more complex layer sequence did not significantly improve the fit in figure 3.8c, data analysis was confined to the model with the fewest fit parameters that adequately describes the data (i.e. the simple two-layer box model shown in figure 3.7b).

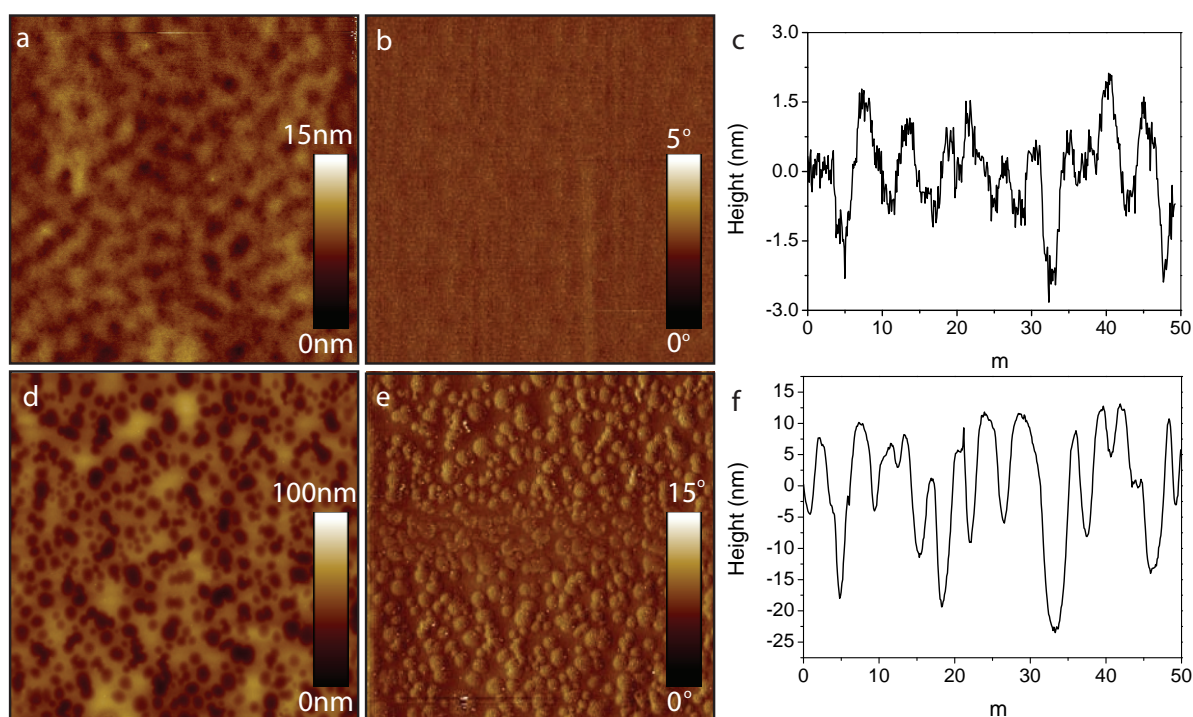


Figure 3.10: AFM micrographs of a (a,b) 210 nm thick film with $\phi = 0.4$ heated at 95°C for 180 min. The AFM topography image in (a) shows the formation of capillary surface instabilities with a wavelength $\sim 4\ \mu\text{m}$ and an amplitude of (c) $\sim 1\ \text{nm}$. (d,e) AFM micrographs of a 210 nm thick film with $\phi = 0.6$ heated at T_{cp} for 180 min. Lateral phase separation is seen in both the height and phase images. (f) Roughness of cross-section of (d).

3.3.2 Surface instabilities

The surface topography of a 210 nm film with $\phi = 0.4$, heated at $T_2 = 95^\circ\text{C}$ is shown in figure 3.10a. Initially, the surface stayed planar. However, after extended annealing, the formation and growth of surface instabilities was observed. The AFM topography images of the film in figure 3.10a reveal a spinodal-like pattern with a characteristic wavelength λ , which varies as a function of blend composition (figure 3.12). The lack of contrast in the AFM phase images in figure 3.10b confirms the absence of a lateral composition variation. The contrast in figure 3.10a therefore arises solely from a variation in surface topography. The optical micrograph in figure 3.11b confirms the initial smoothness of the film, while figure 3.11c shows additional structure on a larger length scale for the film of figure 3.10a. Similar roughening is seen for all blend compositions.

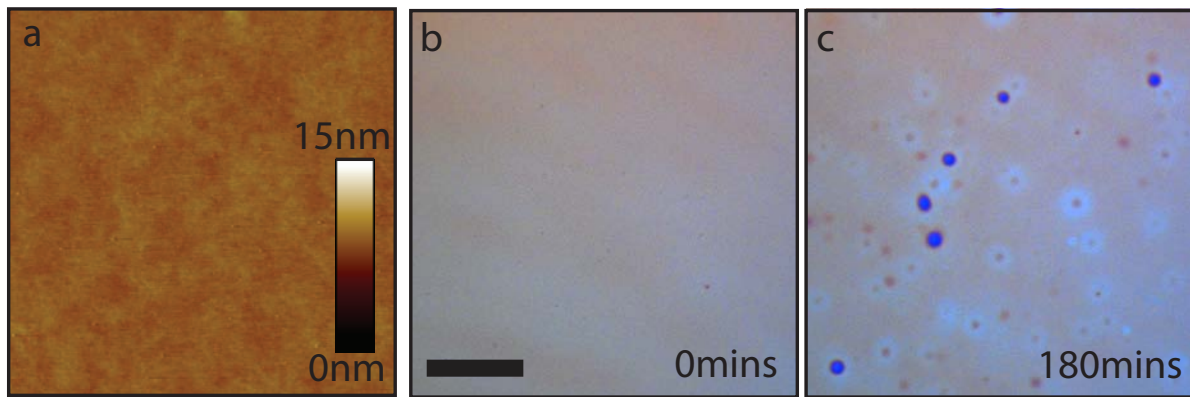


Figure 3.11: (a) AFM topography image of a sample after heating at T_2 for 45 min. (b, c) Optical micrographs of a 210 nm film with $\phi = 0.4$ heated at 95 °C. The optical micrograph of the unannealed film in (a) confirms the smoothness of the initial film, while the optical contrast of the film annealed for 180 min in (c) possibly indicates the onset of dewetting by nucleation. Scale bar is 100 μm .

Figures 3.10d,e show the AFM images for a film with $\phi = 0.6$ heated at T_{cp} for 3 hrs. Phase separated domains are observed in both the height and phase images. The topology is very different to that seen in figure 3.10a and the roughness is increased by one order of magnitude (figure 3.10c, f). This confirms that the instabilities observed in figure 3.10a do not arise from lateral composition variations due to phase separation of the polymers.

The spontaneous formation of capillary instabilities in a non-critical polymer blend is surprising due to the lack of any apparent surface pressure driving the instability. While there is considerable literature on the pattern formation in unstable binary blends, these predominately arise from a lateral variation of surface composition, which is clearly not the case here. Very recently, Thiele and coworkers [30] performed model calculations testing the stability of complete wetting layers that coexist with a bulk of coexisting composition (i.e. bulk compositions that lie on the binodal line). The films in these experiments, while close to bulk coexistence, are clearly in the one-phase regime of the phase diagram.

Clarke [33] has shown that a thin layer of a binary mixture may become unstable with respect to coupled height h and composition ϕ fluctuations, even if the layer is

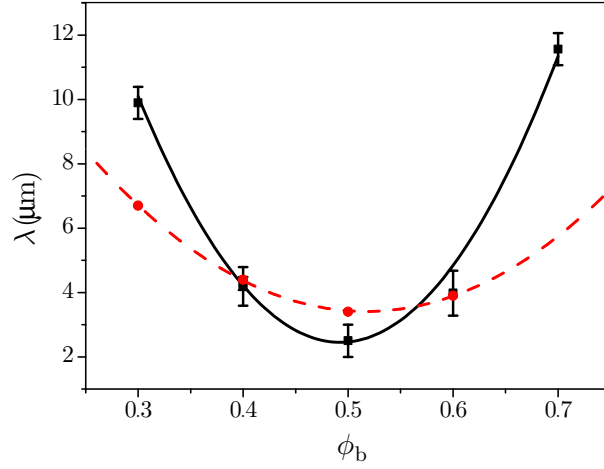


Figure 3.12: (■) Experimentally determined wavelength of the instability as a function of the blend composition, measured after 3 hrs of heating at T_2 . (●) Theoretically determined wavelength found using experimental parameters. The lines are a guide for the eye.

stable to both height and composition fluctuations when treated independently. The condition for instability formation is given by

$$\left[\frac{\partial f_s}{\partial \phi} - h_0 \frac{\partial^2 f_s}{\partial h \partial \phi} \right]^2 > h_0^2 \left(h_0 \frac{\partial^2 f_b}{\partial \phi^2} + \frac{\partial^2 f_s}{\partial \phi^2} \right) \frac{\partial^2 f_s}{\partial h^2} \quad (3.6)$$

where h_0 is the initial height of the unperturbed layer and f_b is the composition dependent local free energy per unit volume within the layer, which is assumed to be independent of h . The model assumes that all unit volumes with the same coordinate in the plane of the layer have the same composition. Hence the total local free energy density due to the bulk is proportional to the height of the film with respect to the substrate. The local surface free energy per unit area f_s is both h and ϕ dependent. As shown in [34], the dynamics of an instability in the plane of the film are described by the two dimensional equations of motion

$$h \frac{\partial \phi}{\partial t} = -\nabla \cdot [hM\nabla\mu_{K\phi}] + \frac{\phi h^3}{3\eta} (\nabla\mu_{K\phi})(\nabla\phi) \quad (3.7)$$

and

$$\frac{\partial h}{\partial t} = -\frac{1}{3\eta} \nabla \cdot h^3 \nabla \mu_{Kh} \quad (3.8)$$

The first term on the right hand side of equation (3.7) represents the diffusive flux, driven by gradients in the chemical potential difference between the two components $\mu_{K\phi} = \delta F_T / \delta_K \phi$, where F_T is the total free energy and M is the mobility of the blend. The second term represents the coupling to hydrodynamics and depends on the blend viscosity η . Equation (3.8) describes the hydrodynamic flow in thin films, which is driven by gradients in the disjoining pressure $\mu_{Kh} = \delta F_T / \delta_K h$. The subscript K in the chemical potential and the disjoining pressure denotes constrained functional derivatives [94, 95]. These ensure that the functional form of the disjoining pressure and the chemical potential take into account the constraints of material and composition conservation. Linearisation of equations (3.7) and (3.8) to first order in height and composition fluctuations leads to

$$\begin{pmatrix} (3\eta/h_0^3)\partial\delta h/\partial t \\ (1/M)\partial\delta\phi/\partial t \end{pmatrix} = A \begin{pmatrix} \delta h \\ \delta\phi \end{pmatrix}. \quad (3.9)$$

If it is assumed that composition and height gradients can be accounted for within the free energy by the contributions $\kappa(\nabla\phi)^2$ and $\sigma(\nabla h)^2$ respectively, where κ is the interfacial energy and σ is the surface tension, then the components of the matrix are given by

$$\begin{aligned} A_{11} &= -q^2 \left(\frac{\partial^2 f_s}{\partial h^2} + 2q^2 \sigma \right) \\ A_{12} &= A_{21} = q^2 \frac{1}{h_0} \left(\frac{\partial f_s}{\partial \phi} - h_0 \frac{\partial^2 f_s}{\partial h \partial \phi} \right) \\ A_{22} &= -q^2 \left(h_0 \frac{\partial^2 f_b}{\partial \phi^2} + \frac{\partial^2 f_s}{\partial \phi^2} + 2h_0 \kappa q^2 \right) \end{aligned} \quad (3.10)$$

The solution to equation (3.9) is

$$\begin{aligned} \delta\phi &= c_{11}e^{R_1 t} + c_{12}e^{R_2 t} \\ \delta h &= c_{21}e^{R_1 t} + c_{22}e^{R_2 t} \end{aligned} \quad (3.11)$$

Physical phenomena of thin surface layers

where the constants c_{ij} are determined by the statistical correlations of the functions prior to the layer becoming unstable. The two rates are the solution to

$$\begin{vmatrix} \frac{\hbar_0^3}{3\eta}A_{11} - R & \frac{\hbar_0^3}{3\eta}A_{12} \\ MA_{12} & MA_{22} - R \end{vmatrix} = 0. \quad (3.12)$$

Whilst the q -dependence of the rates depends on both the viscosity and mobility, the critical wave vector, the wavelength below which fluctuations are unstable and grow can be determined, without knowledge of either of these parameters. If $A_{11}, A_{22} > 0$ then one of the solutions to equation (3.12) is equal to zero when

$$A_{11}A_{22} - A_{12}^2 = 0. \quad (3.13)$$

To make further progress, it is necessary to choose a functional form for the bulk and surface energies. The bulk free energy is determined using the Flory-Huggins theory, such that

$$\frac{\partial^2 f_b}{\partial \phi^2} = \frac{2k_B T(\chi_s - \chi)}{a^3} \quad (3.14)$$

where χ_s is the value of the interaction parameter on the spinodal curve. The factor $k_B T/a^3$ ensures that the energy scales of the bulk and surface energies are matched appropriately. The surface free energy is given by $f_s = -A_H/\pi h^2$, where A_H is the composition dependent Hamaker constant. It is found using the Lifshitz theory [28] and is given by

$$A_H = d_1(d_2(\phi_b - \phi_s)) - d_3\phi_b\phi_s \quad (3.15)$$

where $d_1 = 3.867 \cdot 10^{-22}$ J, $d_2 = 54.328$ and $d_3 = 10.452$ are constants calculated using the refractive indices of the bulk and surface layers with compositions ϕ_b and ϕ_s .

The interfacial energy is given by [96]

$$\kappa = \frac{k_B T}{a^3} \left(\frac{a^2}{36\phi(1-\phi)} \right) \quad (3.16)$$

For the surface energy a fixed value of $\sigma = 30 \text{ mNm}^{-1}$ [85] was used.

One difficulty that arises from assuming discrete wetting is that the composition of the surface layer falls inside the bulk two-phase region for some compositions and hence should be unstable. However, this interpretation is based on the bulk behaviour and it is known that for thin layers the transition temperature is shifted upwards for LCST behaviour [97]. In order to overcome this difficulty, the value of the interaction parameter required for an instability to form is considered and given such values, the resulting critical wave vector of the instability is determined.

Unstable fluctuations are found for $0 < (\chi_s - \chi) < 1.5 \cdot 10^{-5}$. It should be emphasised that for these conditions both $\partial^2 f_b / \partial \phi^2$ and $\partial^2 f_s / \partial h^2$ are positive, so that when considered independently the layer is stable to either concentration or height fluctuations; it is the coupling between the two that leads to the instability.

The theoretical values of the critical wavelength, $\lambda_c = 2\pi/q_c$, found using the experimentally determined ϕ_b and ϕ_s for $(\chi_s - \chi) = 1.4 \times 10^{-4}$ are shown in figure 3.12. The critical wavevector q_c is given by the solution to equation 3.13, which is quadratic in q_c^2

$$4h_0\kappa\sigma q_c^4 + 2 \left[\sigma \left(h_0 \frac{\partial^2 f_b}{\partial \phi^2} + \frac{\partial^2 f_s}{\partial \phi^2} \right) + h_0\kappa \frac{\partial^2 f_s}{\partial h^2} \right] q_c^2 + \left(h_0 \frac{\partial^2 f_b}{\partial \phi^2} + \frac{\partial^2 f_s}{\partial \phi^2} \right) \frac{\partial^2 f_s}{\partial h^2} - \frac{1}{h_0^2} \left(\frac{\partial f_s}{\partial \phi} - h_0 \frac{\partial^2 f_s}{\partial h \partial \phi} \right)^2 = 0 \quad (3.17)$$

The trend is qualitatively similar to that seen in the experimental data, with the absolute values of the critical wavelength being comparable to the fastest growing wavelength. For both phase separation and dewetting, the relation between the critical and the fastest growing wavelength is given by $q_m = \sqrt{2}q_c$. Although such a simple relation does not exist for the coupled process, it seems reasonable to assume that the trend associated with the critical wavelength is a good indication of that expected for the fastest growing wavelength.

The compositional dependence shown in figure 3.12 arises from the dependence of the Hamaker constant A_H on both ϕ_s and ϕ_b , as seen in equation 3.15. The driving

force for the instability in the case of a coupled process, depends on the first derivative of A_H with respect to ϕ_s , which varies as a function of ϕ_b . The absolute value of the negative Hamaker constant is greatest for $\phi_b = 0.3, 0.7$ and smallest for $\phi_b = 0.5$.

Clarke has shown that the greater the difference between h_{crit} (the critical value of h , below which an instability will occur) and the wetting layer thickness, the smaller the wavelength of the evolving instability [33]. This is equivalent to the theory of phase separation where a deeper quench results in a smaller, most unstable wavelength.

Here the wetting layer thickness was shown to be constant for all blend compositions. The ‘quench depth’ therefore depends only on h_{crit} . A smaller A_H implies a larger h_{crit} and therefore a greater quench depth. Hence, the smallest instability wavelength is observed for $\phi_b = 0.5$.

3.4 Conclusions

This study presents clear evidence for a surface instability in a binary PS/PVME polymer blend heated close to its demixing temperature, staying well within the one-phase regime of the blend. The behaviour of varying blend compositions was studied at temperatures where the PS and PVME were miscible. Ellipsometric measurements confirm the build-up of a PVME surface enrichment layer. After heating at 10 °C below the demixing temperature for 45 min, this surface layer was seen to have a thickness comparable to the bulk correlation length of the PVME ~ 20 nm. Further heating resulted in the formation of an instability at the polymer/air interface. These exhibited a spinodal-like pattern with a characteristic wavelength dependent on the blend composition. Instabilities were observed for all blend compositions.

Theoretical modelling of the system, using a thermodynamic approach, suggests that the instabilities results from coupled height and composition fluctuations in the PVME wetting layer. The model can be used to define a critical wetting layer thickness, below which the layer will become unstable. The composition dependent in-

stability wavelength, arises from the dependence of the Hamaker constant on both the bulk and wetting layer compositions. The Hamaker constant defines the critical wetting layer thickness. Since the experimentally observed PVME wetting layer has the same thickness for all blend compositions, the Hamaker constant determines the 'quench depth' of the system. The greater the difference between the critical layer thickness and the wetting layer thickness, the smaller the wavelength of the resulting instability.

Instabilities were only observed in blends heated close to the demixing temperature. PVME-rich wetting layers were also observed to form at the polymer/air interface in blends kept at room temperature for extended periods of time. These blends were stable however and no instabilities were seen to evolve.

OUT OF EQUILIBRIUM DYNAMICS OF THIN POLYMER FILMS

The process of spin coating to form thin films is widely used in polymer science and in technological applications. The popularity of the technique stems from the ability to form uniform films over large areas, with thicknesses ranging from a few nanometres to a few micrometres.

A drop of polymer solution is placed onto a substrate, which is then rotated causing the solution to spread. The solvent rapidly evaporates, increasing the glass transition temperature T_g of the liquid film. When T_g reaches the ambient temperature, the polymer vitrifies forming a glassy film. While the remaining solvent continues to evaporate, the conformations of the chains within the film are frozen-in.

Films formed in this way are often seen to exhibit anomalous structural and dynamic properties, which strongly differ from the bulk behaviour of the polymer [7, 98–100]. The properties of films are dependent on the film thickness, with a greater deviation from bulk behaviour seen as the film thickness is decreased¹. Films which are thicker than 100 – 200 nm are generally considered to have bulk behaviour.

¹The discussion here is limited to films thicker than the coil size of the polymer chain. For thinner films, confinement effects of the polymer chain may start to play a role and must also be considered.

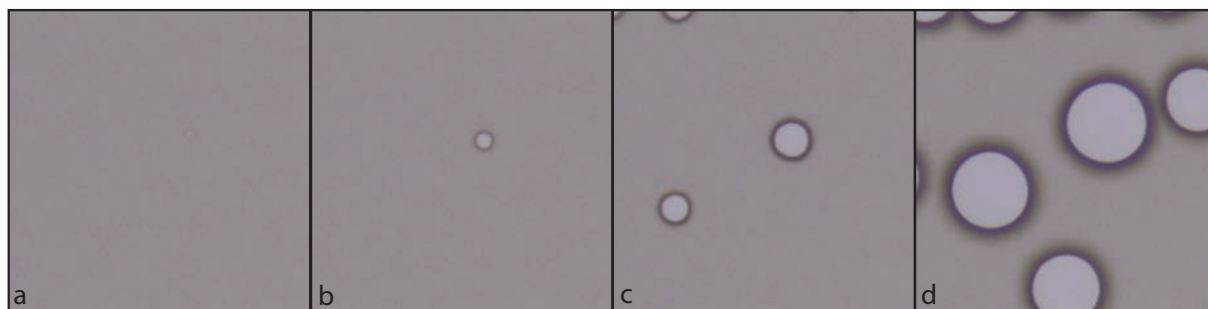


Figure 4.1: Optical micrographs of dewetting observed in a 40 nm PS film heated at 125 °C after (a) 0 min (b) 1 min (c) 10 min (d) 60 min. PS $M_w = 4000 \text{ kg mol}^{-1}$ was spun from toluene at 6000 rpm onto a silicon wafer coated with a 10 nm PDMS layer.

Thin polymer films have been shown to exhibit a negative thermal expansion coefficient when heated close to the glass transition temperature T_g [99]. As the film thickness is decreased, the onset of this thickness contraction is seen to occur at lower temperatures with $T \ll T_g$ [100].

Bulk equilibrium behaviour can be achieved for spin-cast films through thermally annealing the films above T_g for an extended period of time [101]. Jones *et al.* have shown that films annealed for times greater than the time required for the polymer chain to diffuse a distance comparable to the radius of gyration R_g of the polymer, have the same chain conformations as those observed in the bulk [102]. Films with thicknesses of 10 – 100 nm have been investigated and no thickness dependence was observed except for the thinnest films, where the thickness was comparable to R_g . Kim *et al.* have shown that thermally annealed films have a viscosity equalling that of the bulk viscosity of the polymer [103, 104].

The difference in behaviour is thought to arise from non-equilibrium conformations of the polymer chains and frozen-in stresses, resulting from the preparation of the films from solutions by rapid solvent evaporation. A popular method of investigating the behaviour of thin polymer films is through studying the dewetting of a polymer film on a substrate [105]. The dewetting process can be explained in terms of non-equilibrium chain conformations and entanglements in thin polymer films, the relaxation of which can be probed *in situ* in real time. In dewetting experiments,

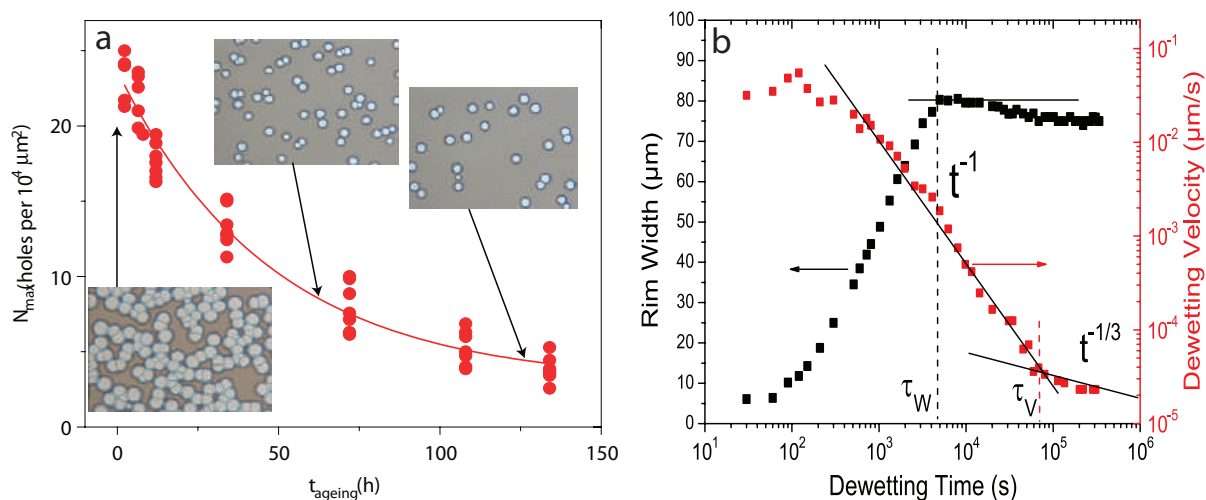


Figure 4.2: (a) Number of holes which spontaneously nucleate in PS films aged at 50°C for various times. The insets show typical micrographs. (b) Evolution of the dewetting velocity and rim width for a PS film. τ_w indicates the timescale on which residual stresses relax, while τ_v indicates the timescale on which equilibration of the film takes place. Graphs taken from [106] and [107] respectively.

the film is heated to $T > T_g$ after spin casting. Upon annealing, holes form and grow. An example of this can be seen in figure 4.1. The shape of the rim and the growth velocity of the holes can be interpreted in terms of molecular, interfacial and rheological properties of the film. Films which are aged below T_g show a decreasing number of spontaneously nucleated holes per unit area are observed upon heating above T_g [106] (figure 4.2a). After a sufficiently long period of aging, it is predicted that holes will no longer form in an idealised polymer film.

The change in rupture probability is a signature of the metastability and non-equilibrated chain conformations of the films and suggests higher stresses in the as-spun films as compared to the aged films. Residual stresses, which can be stored in the films due to distorted chain conformations, provide an additional driving force for dewetting, thereby accelerating the process [108]. As the films are aged, these stresses relax as the polymer chains adopt conformations closer to equilibrium and the holes stop growing (figure 4.2b). The results suggest that the anomalous behaviour observed in as-cast films originates from the film preparation and can be removed by aging below T_g .

Dewetting experiments can also be used to probe the rheology of the films. The velocity of the dewetting front gives an indication of the viscosity of the fluid. Seemann *et al.* have shown that the viscosity is significantly reduced, compared to the bulk, in as-cast PS films [19]. Masson *et al.* show a similar viscosity reduction but only for films with a thickness less than 80 nm [101]. A transition in the dewetting velocity is observed on timescales greater than the relaxation of residual stresses [107]. This is shown in figure 4.2b and suggests that residual stresses may relax without full equilibration of the polymer chains, which requires the film to be annealed at $T > T_g$.

While dewetting experiments give insight into the non-equilibrium properties of as-cast films or films aged below T_g , fully equilibrated films cannot be probed due to the unstable nature of the films. Barbero *et al.* have shown that electric fields can be used to perturb the free surface of a polymer film heated above T_g in order to probe the rheology of the liquid film [7]. In these experiments the films are intrinsically stable in the absence of the destabilising force, allowing for the direct comparison of as-cast with equilibrated films.

Electric field destabilisation provides an ideal way to study the behaviour of liquid polymer films due to the ability to disentangle the force balance driving the instability from the rheology within the film, which is not possible in dewetting experiments. The magnitude of the characteristic wavelength λ of the instabilities reflects the balance of forces acting on the surface of the film and is not dependent on the film rheology as long as the flow in the film can be considered to be laminar. The characteristic onset time τ of the instabilities however, is proportional to the viscosity of the film.

Figure 4.3 shows the characteristic destabilisation time of the film as a function of the instability wavelength for PS with different molecular weights M_w , as measured by Barbero [7]. As-cast films are observed to have a substantially reduced viscosity as compared to the bulk (figure 4.3a,c,e). Annealing the films above T_g , for sufficiently long times prior to destabilisation, results in an increase in the measured viscosity, with bulk viscosity being recovered (figure 4.3b,d).

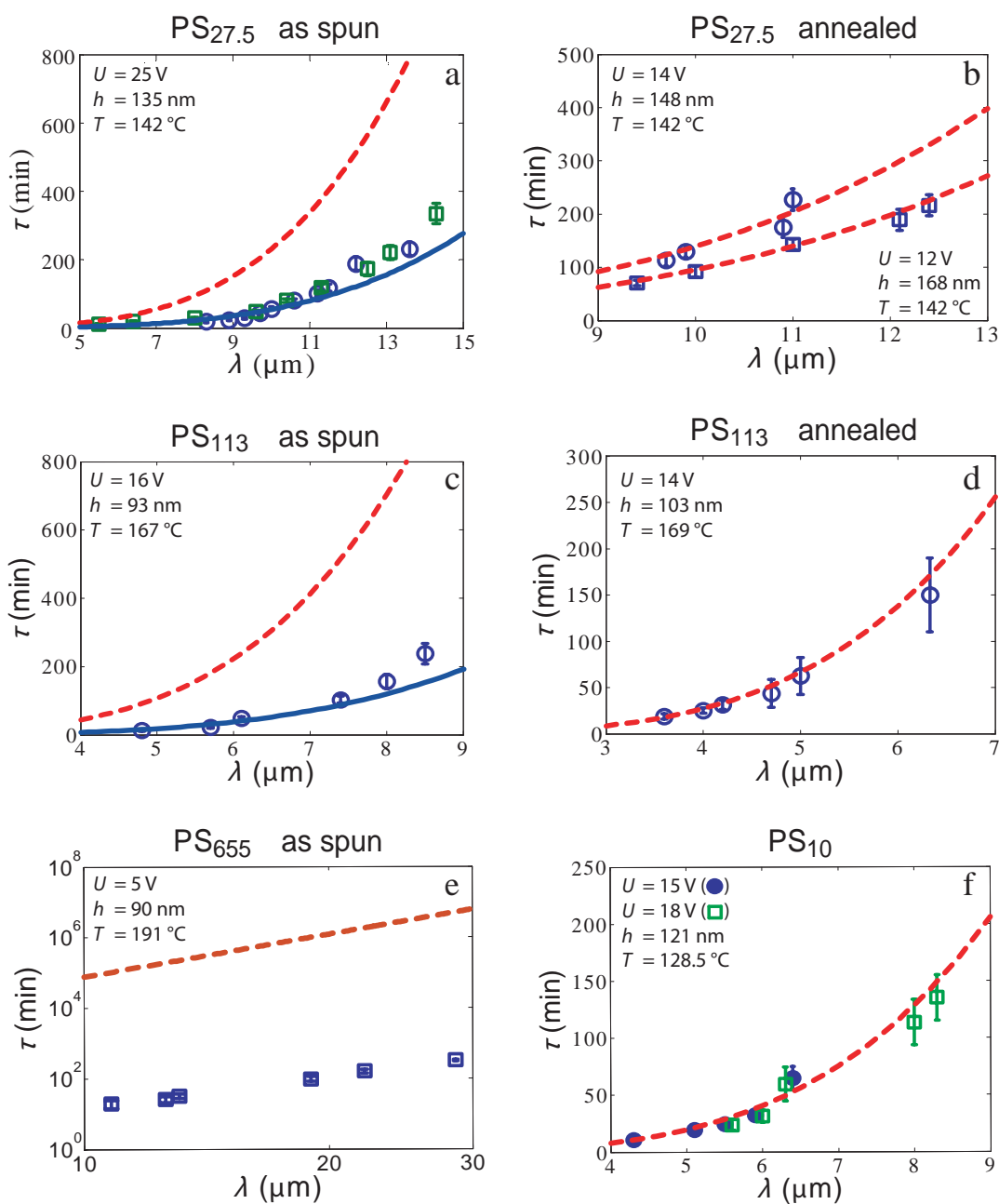


Figure 4.3: Characteristic destabilisation time τ vs. wavelength λ . (a),(c) and (b),(d) compare films before and after annealing. The different symbols in (a) correspond to bare and functionalised substrates, (b) samples of different thicknesses, (f) annealed and as-cast films. Dashed lines are the predictions using the bulk viscosity, the solid lines are fits found by varying the viscosity. Graphs taken from [7].

The destabilisation of films with $M_w = 10\text{ kg mol}^{-1}$ does not show this effect (figure 4.3f). The M_w of this polymer is below the entanglement molecular weight of PS. Here the data for the as-cast and annealed films are both described by the bulk viscosity.

Physical phenomena of thin surface layers

Similar behaviour is observed by Yang *et al.* who investigated the viscosity of PS films with $M_w = 2.4 \text{ kg mol}^{-1}$ via spinodal decomposition of the films [109].

Barbero [110] also looked at the role of the film/substrate interface on the properties of the film. A reduction in the characteristic onset time is predicted if there is finite slip at the liquid/solid interface, which could be the cause of the observed reduction in viscosity. The results are shown in figure 4.3a, where films spun onto cleaned silicon wafers are compared to those spun onto surface-functionalised wafers, which have a substantially reduced interfacial energy with the PS. The results show that the characteristic destabilisation times for the two sets of films are indistinguishable. This indicates that the solid boundary does not play a significant role during the early stage of destabilisation and interfacial slip is not the cause of the increased mobility observed in the as-cast films.

The reduced effective viscosity is instead explained in terms of entanglements of the polymer chains. In the initial phase of spin coating, the polymer is in a semi-dilute solution with a good solvent. As the solvent evaporates the chains start to entangle. As the polymer concentration increases further, this process slows and stops once the film vitrifies. This results in a lower entanglement density per chain and therefore lower viscosity than seen for a fully equilibrated film. Annealing at $T > T_g$ equilibrates the chains, restoring the melt entanglement density and viscosity. This model is corroborated by Tsui *et al.*, who show that in high M_w PS, the elastic modulus of the polymer in spin coated films is substantially reduced compared to bulk PS [111]. This again suggests the chains have a lower entanglement density and did not have time to fully interpenetrate before vitrification.

This chapter builds on the work of Barbero, using electrohydrodynamic (EHD) destabilisation to explore the effect of the solvent used for spin-casting on the properties of the film produced. Both the viscosity and the residual stresses in the film are studied. Particular attention is paid to the timescale on which these stresses relax. Solvent vapour annealing is used as an alternative method to thermal annealing,

to achieve fully equilibrated films on much shorter timescales. In tandem with this study, similar experiments were carried out by Adam Raegen and Günter Reiter at the University of Freiburg, where the effect of casting solvent on the dewetting of PS films was investigated. The results of these experiments are discussed and compared to those of the EHD destabilisation study.

Physical phenomena of thin surface layers

Solvent	T_{bp} (°C)	T_{m} (°C)	η (25 °C)	φ_{solvent}
Trans-decalin (TD)	187	-31	1.948	0.46 (0.3)
Toluene	110	-95	0.560	0.23
Chloroform	61.2	-64	0.537	0.32
Methyl ethyl ketone (MEK)	79.6	-87	0.405	0.25
Tetrahydrofuran (THF)	66	-45	0.456	0.30

Table 4.1: Boiling point T_{bp} , melting point T_{m} , viscosity η and concentration of solvent φ_{solvent} at vitrification of the polymer for the solvents used for spin coating. Physical data taken from [86]. φ_{solvent} for TD is shown for 25 °C (55 °C).

4.1 Materials and methods

Polystyrene (PS) $M_w = 200 \text{ kg mol}^{-1}$ (PS200), $M_w/M_n = 1.09$ (Polymer Source), PS $M_w = 655 \text{ kg mol}^{-1}$ (PS655), $M_w/M_n = 1.09$ (Polymer Source) and PS $M_w = 4000 \text{ kg mol}^{-1}$ (PS4000), $M_w/M_n = 1.15$, (Polymer Standards Service) were used as obtained without further purification. The glass transition of the three polymers is at $\sim 105 \text{ °C}$ ². The dielectric constant of PS is 2.5 [86], this is unchanged on application of a DC electric field [112]. The PS films were spin coated onto cleaned silicon substrates from solution with a spin speed of 4500 rpm. The solvents used and their properties are given in table 4.1. Films spun from trans-decalin (TD) solutions were spun at 55 °C and 25 °C. For all other solvents films were formed at room temperature. After spin coating, all samples were annealed at 60 °C for 15 min to remove any residual solvent.

Spin coating is a commonly used technique to coat substrates with thin polymer layers. The substrate is coated with droplets of the solution and is subsequently rotated at a given speed. On rotation of the substrate, the solution spreads out forming a liquid layer. Once a homogeneous film thickness across the substrate is established, thinning of the liquid layer occurs mainly by solvent evaporation, with draining of the solution across the edge becoming negligible. The spreading of the liquid and the rate of thinning are dominated by viscous forces and the boiling properties of the solvent, assuming that the spinning speed is constant. Films spun from TD, which has a high

²Physical data as determined by the supplier.

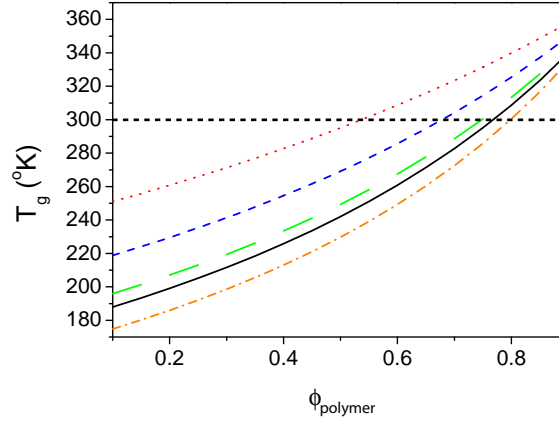


Figure 4.4: Variation of T_g for PS in Toluene (solid), TD (dotted), chloroform (short-dash), MEK (long-dash) and THF (dash-dot) as a function of φ_{polymer} according to equation 4.1. Vertical dashed line indicates φ_{polymer} at 300 K.

boiling point, were seen to form more slowly than those spun from tetrahydrofuran (THF), which has a much lower boiling point.

When the solvent concentration reaches a critical value φ_{solvent} , the polymer vitrifies, forming a smooth film. The critical solvent concentration is dependent on the melting point of the solvent and the glass transition temperature of the polymer and can be found using the Fox equation [113]

$$\frac{1}{T_g} = \frac{\varphi_{\text{solvent}}}{T_m} + \frac{1 - \varphi_{\text{solvent}}}{T_p} \quad (4.1)$$

where T_p is the glass transition temperature of the polymer and T_m is the melting point of the solvent. T_g is the temperature at which the polymer vitrifies, which in this case is 300 K. Figure 4.4 shows the variation in T_g as a function of φ_{solvent} for each solvent used. The graph was used to obtain the values for φ_{solvent} given in table 4.1.

The final film thickness is dependent on a number of parameters including the viscosity, the spin speed and the concentration of the initial polymer solution used. Here the spin speed was kept constant. 1% and 3% solutions were used to form 100 nm thick films for $M_w = 4000 \text{ kg mol}^{-1}$ and $M_w = 200 \text{ kg mol}^{-1}$ PS respectively. Films were used as-cast, after annealing at $T_{\text{anneal}} = 155 \text{ }^\circ\text{C}$ or after solvent annealing. A vacuum

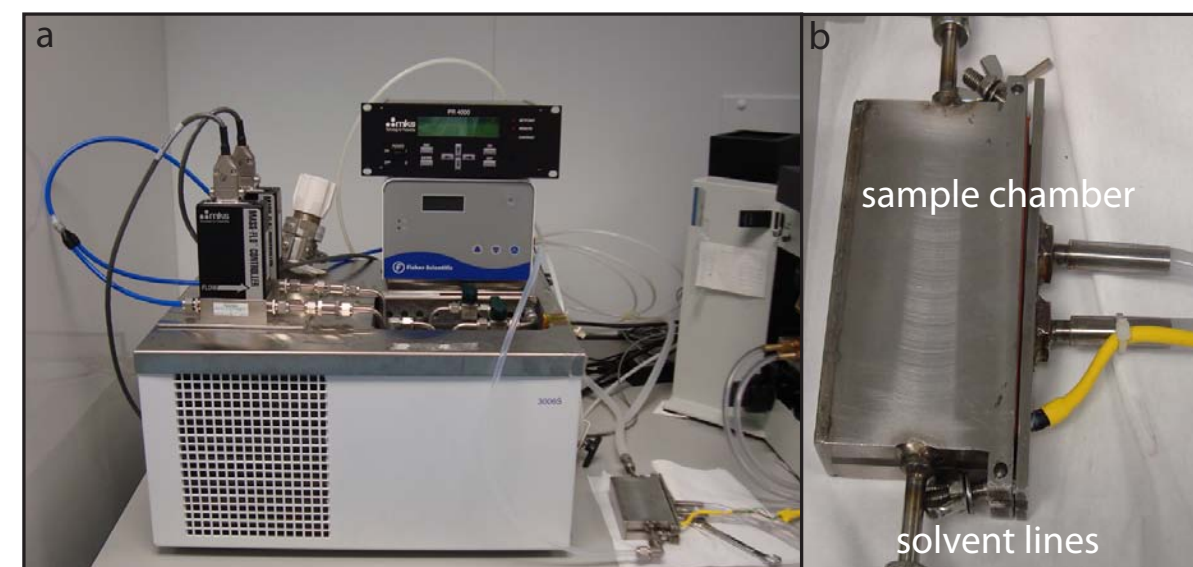


Figure 4.5: (a) Solvent vapour setup. (b) Sample chamber.

oven was used for thermal annealing to avoid degradation of the polymer.

Vapour annealing

The vapour annealing setup can be seen in figure 4.5. The films were placed in the annealing chamber, which was then sealed and filled with solvent vapour of a given concentration. The vapour causes the film to swell. All experiments were carried out using toluene. The films were all initially swollen in an atmosphere containing 50% toluene, followed by a step with a reduced toluene concentration. All films were dried under nitrogen flow for 15 min after solvent annealing to remove any residual solvent.

The film thickness before and after vapour annealing was measured using ellipsometry, as discussed in chapter 3. The 100 nm films were seen to increase by 20–25 nm during the vapour annealing process. After 5 mins in the solvent atmosphere the film stopped swelling and the thickness remained constant for the rest of the annealing time. The film thickness was unchanged after vapour annealing was finished, confirming that all solvent had been removed.

Destabilisation setup

The formation of electrohydrodynamic (EHD) instabilities was carried out using two

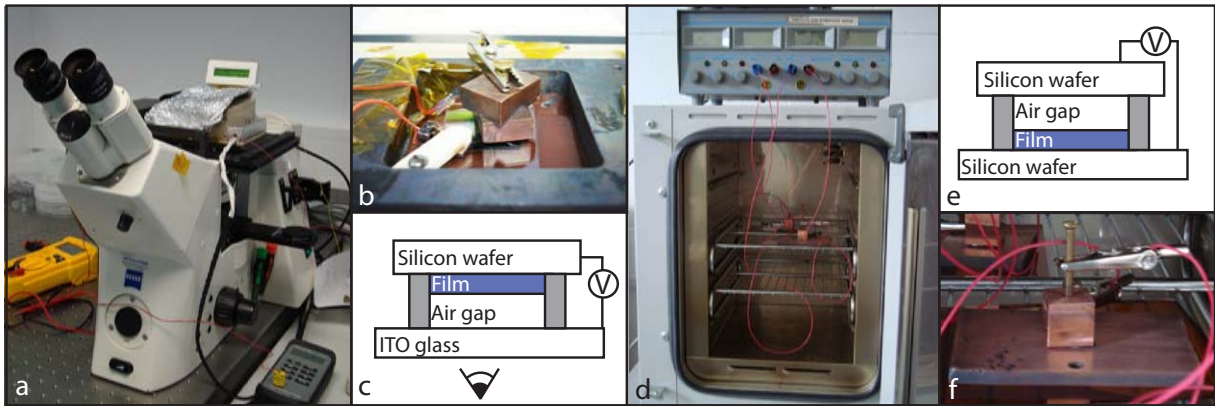


Figure 4.6: Experimental setups. (a,b) Microscope setup. (c) Polymer film is sandwiched with an air gap between silicon and ITO glass electrodes. The ITO glass provides a transparent electrode for viewing. (d,f) Oven setup. (e) Polymer film is sandwiched with an air gap between two silicon electrodes.

different experimental setups, which can be seen in figure 4.6. The oven setup (figure 4.6d,f) was used to investigate the change in wavelength as a function of the electric field, while the microscope setup (figure 4.6a,b) was used to explore the onset time of instability formation. It should be noted that while the schematic representations shown in figure 4.6c,e show parallel capacitor plates, experimentally a small wedge geometry was always achieved. The electric field is inversely proportional to the separation of the capacitor plates and as a result each sample could be used to obtain a number of data points.

Silicon wafers (specific resistance = $6 - 10 \Omega \text{ cm}^2$) covered by a 40 nm gold layer on their backside were used as negative electrodes. A 5 nm chromium layer was used to adhere the gold to the wafer. The gold layer provided good electrical contact to the copper plates used to assemble the devices. The wafers were attached to the copper plates using a silver paste. Silicon wafers and indium-tin oxide (ITO) coated glass (specific resistance = $80 - 100 \Omega \text{ cm}^2$) were used for the upper electrodes.

Photolithography

Photolithography was used to create SU8 spacers on the electrodes to provide an air

Physical phenomena of thin surface layers

gap between the polymer film and the upper electrode. SU8 2000.5 photoresist was spun onto the cleaned silicon/ITO glass at a spin speed of 6000 rpm. The films were temperature cured using the following procedure: heat at 60 °C for 1 min, 100 °C for 1 min, 60 °C for 1 min. This heating procedure was carried out to remove residual solvent, relax stresses in the photoresist and to promote adhesion with the substrate.

The resist film was aligned for photocuring using an MJB4 mask aligner. This allows for selective exposure of the film with UV light through a mask. The masks were made of UV-transparent quartz glass patterned with an absorber metal, in this case chromium, which is opaque to UV light.

UV curing was carried out for 2 s. Upon exposure to UV light, the resist undergoes changes in its chemical and physical properties which alter its solubility. Areas masked by the chromium were left unchanged. The films were then post-baked for 1 min at 60 °C, 1 min at 100 °C and 1 min at 60 °C to complete the chemical reaction. The substrate was rinsed in SU8 developer, which selectively dissolves the unexposed areas and rinsed in isopropanol. A final bake at 175 °C for 2 min was carried out to remove and dry any developer residue.

Experimental conditions

The devices were assembled in the EHD setups at room temperature. The films were heated to 175 °C and the temperature was allowed to equilibrate. The equilibration times were 20 min and 5 min for the oven and the microscope setup respectively. Once the temperature had equilibrated, the electric field was turned on, defining the start of the experiment ($t = 0$).

Figure 4.7 shows the effect on the measured wavelength of the instabilities as a function of the applied electric field for the two different setups. In addition, devices were placed into a pre-heated oven and the electric field turned on directly. No difference was seen in the resulting behaviour.

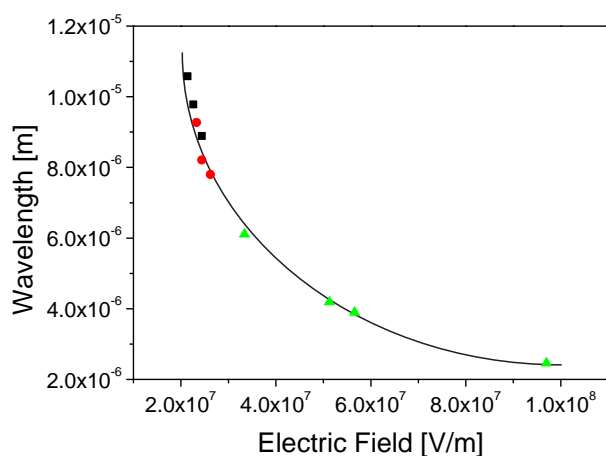


Figure 4.7: Variation in the wavelength of the instability as a function of the electric field for a 100 nm PS=200 kg mol⁻¹ film. (■) Oven setup. (▲) Microscope setup. (●) Oven setup - preheated. The line is a guide for the eye.

4.1.1 Optical observation of instabilities

The microscope setup shown in figure 4.6a,b was used for *in situ* observation of the EHD instabilities in real time. The electrodes were placed on a heated stage, mounted on an inverted microscope. The white light from the halogen light source passed through an interference filter, providing quasi-monochromatic illumination of the sample. The mean wavelengths of the interference filters used were 515 nm and 532 nm. The silicon wafer and ITO glass, used as electrodes, acted as an optical cavity. Interference fringes due to the recombination of light beams within the cavity were observed. An example of the fringes is shown in figure 4.8a.

The use of light interference allowed for accurate observation of the onset of instability formation. Initially the film was flat and appeared monochromatic (figure 4.8a). Interference fringes were observed due to the variation in the thickness of the air gap, as a result of the wedge geometry of the setup. The formation of instabilities results in local variation of the film thickness and a change in the intensity of the reflected light (figure 4.8b). For a 3 nm variation in the thickness, the change in intensity of the reflected light is on the order of 7 – 20% for the experimental configuration used here [110], depending on the position of the instability with respect to

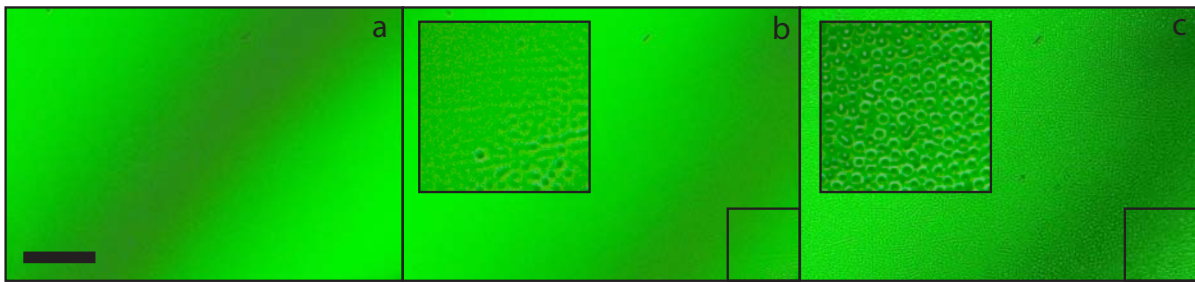


Figure 4.8: Example images showing the destabilisation of a PS film. (a) Initial uniform film showing interference fringes. (b) Onset of EHD instabilities. (c) Instabilities start to form columns. (b,c) Insets show magnification of selected area. Scale bar: 100 μm .

the interference fringes. This change in intensity allows the instability formation to be easily observed using optical microscopy and the time taken for the instability to reach a few nanometres in height to be easily measured. For a more detailed discussion of the experimental setup and the use of light interference in an optical cavity to measure film thickness and the growth of instabilities see [110].

Atomic force microscopy

The height and wavelength of the EHD instabilities formed in the oven were investigated using a Dimension 3100 Veeco atomic force microscope. Atomic force microscopy (AFM) was chosen due its nanometre resolution and non-destructive imaging.

AFM is a high-resolution imaging technique, which allows the topography and composition of a surface to be imaged. Figure 4.9a shows a schematic representation of the AFM. AFM works by measuring the interactions between the sample and the tip. In TappingMode™ or non-contact mode, the tip does not touch the sample. The cantilever is driven at its resonance frequency and a feedback loop is used to maintain a constant amplitude of the cantilever. Topographic and phase images are derived from measurements of the attractive force between the tip and the sample due to deflections of the tip as it is scanned across the surface. These deflections are measured using a laser focused onto the backside of the cantilever.

AFM can also be used in contact mode. This can however, damage the sample.

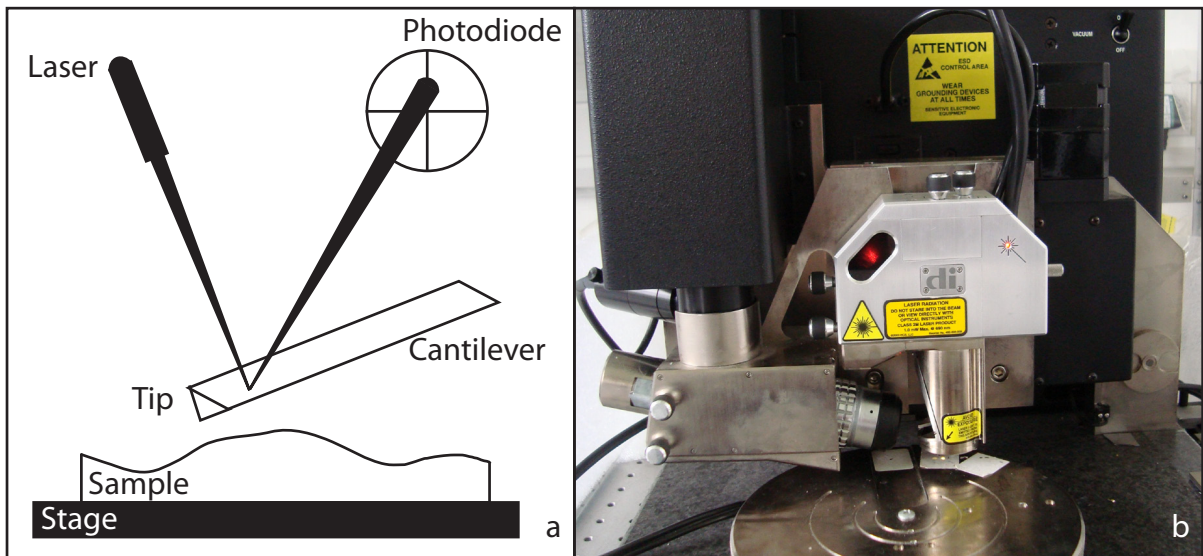


Figure 4.9: (a) Schematic representation of AFM. (b) Dimension 3100 Veeco AFM used in this study.

Only non-contact mode was used here. AFM was also used for roughness measurements and to observe the phase separation of PS/PVME films as discussed in chapter 3. For a more detailed discussion on AFM see [114].

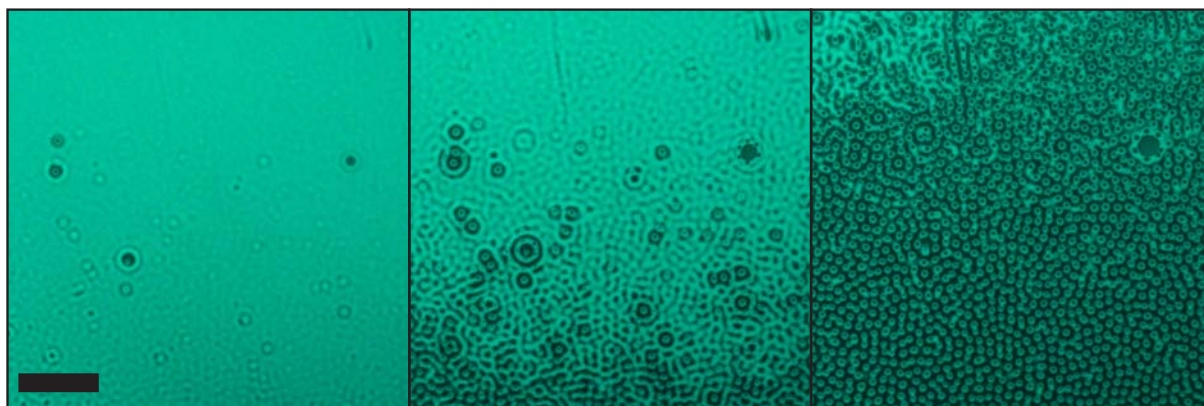


Figure 4.10: Onset and growth of EHD instabilities in PS200 spun from trans-decalin. Scale bar is 20 μm .

4.2 Results and discussion

The application of an electric field across the polystyrene (PS) film heated at $T > T_g$ resulted in the destabilisation of the film and the evolution of a surface wave with a characteristic wavelength. An example of this for a film spun from trans-decalin is shown in figure 4.10.

4.2.1 Toluene

Film rheology

The characteristic onset time τ as a function of the wavelength of the instability is given by

$$\tau = \frac{3\eta}{\gamma h_0^3} \left(\frac{\lambda}{2\pi} \right)^4 \quad (4.2)$$

where h_0 is the thickness of the initial film. The onset time is proportional to the viscosity η and inversely proportional to the surface tension γ of the liquid film.

Figure 4.11 shows the onset times for EHD instabilities observed in PS200 films spun from toluene, as measured using the optical setup. Data were obtained for films destabilised directly after spin coating and for films annealed for 140 hrs at $T_{\text{anneal}} = 155^\circ\text{C}$ prior to destabilisation. From figure 4.11 it can be seen that the characteristic onset

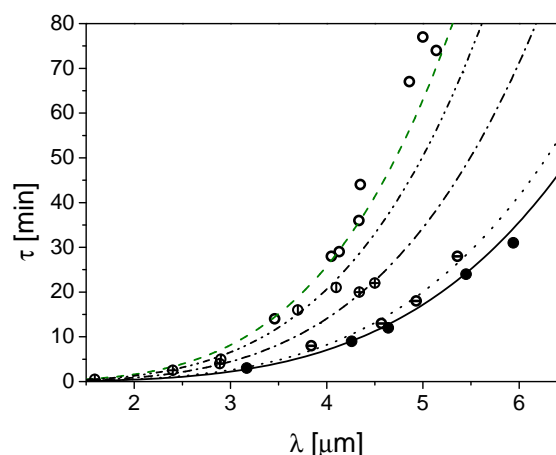


Figure 4.11: Characteristic destabilisation time τ vs λ for (●) as-spun films and after annealing at T_{anneal} for (⊖) 30 hrs, (⊕) 70 hrs, (⊙) 96 hrs and (○) 140 hrs. Lines show fits to the data using equation 4.2 with $\eta = 30, 35, 65, 90, 110 \text{ kPa} \cdot \text{s}$.

time τ is greatly reduced in the as-spun films. This corresponds to an increase in the mobility of the film.

From equation 4.2 it can be seen that changes in τ may result from changes in γ , ε_p and/or η . The dielectric constant ε_p of PS is 2.5 [86]. Park *et al.* have shown that the application of a high DC field to a polymer film, similar to those used here, does not change the measured value of ε_p [112]. The surface tension of PS is $\gamma = 27.5 - 36.0 \text{ mN/m}$ at temperatures between 130°C and 200°C . The surface tension is both temperature and molecular weight dependent. For $M_w = 200 \text{ kg mol}^{-1}$, $\gamma \approx 35 \text{ mN/m}$ at 175°C [115]. The experiments here were carried out at constant temperature and applied voltage. Small fluctuations in γ and ε_p do not account for the large decrease in τ demonstrated in figure 4.11.

Barbero *et al.* have shown that the only likely parameter that can be used to explain the observed decrease in τ is the viscosity of the liquid film [7]. The curves in figure 4.11, show fits to the data using equation 4.2, assuming viscosities of $30 \text{ kPa} \cdot \text{s}$ for the as-spun film and $110 \text{ kPa} \cdot \text{s}$ for the film annealed for 140 hrs. The latter corresponds closely to $\eta = 127 \text{ kPa} \cdot \text{s}$, the bulk viscosity of the polymer³.

In figure 4.3 the data for large λ lie above the curve fitted to the data at small λ . Bar-

³The viscosity of the bulk polymer was measured using a parallel plate rheometer.

Physical phenomena of thin surface layers

berero suggests that this is due to chain relaxation during the experiment. This is not observed in the data shown here. These experiments were conducted at higher applied voltages and therefore electric fields than those of Barbero. The onset of destabilisation was observed on timescales of 2 – 80 min. Using a similar M_w PS, Barbero observed destabilisation on a timescale of 20 – 220 min, with a deviation in the fit being observed after 120 min (figure 4.3c), which is much greater than the length of the experiments conducted here.

A small increase in τ was observed after 30 hrs of annealing at T_{anneal} prior to destabilisation. The characteristic onset times for the EHD instabilities observed after 30 hrs of annealing are shown in figure 4.11. An increase in the viscosity of $\sim 5 \text{ kPa} \cdot \text{s}$ is measured. Full equilibration and the recovery of bulk properties however, occurs after much longer annealing times. The time dependence of the relaxation is discussed later in this chapter.

The recovery of bulk viscosity in the films on annealing above T_g suggests that the increased mobility observed in the as-cast films results from non-equilibrium effects caused by the spin coating film deposition procedure. Annealing of the films for sufficiently long times removes this non-equilibrium effect.

Residual stresses

The characteristic wavelength λ of the instabilities as a function of the applied electric field is given by

$$\lambda = 2\pi \sqrt{\frac{2\gamma U}{\epsilon_0 \epsilon_p (\epsilon_p - 1)^2} E_p^{-3/2}} \quad (4.3)$$

and gives an indication of the forces and residual stresses acting on the film. Figure 4.12 shows the characteristic wavelength of fully formed instabilities as a function of the applied electric field for PS4000. The line shows the theoretical prediction of equation 4.3. Films annealed for 140 hrs are well described by equation 4.3. For as-cast films however, the values of λ are systematically higher. Figure 4.12 also shows values

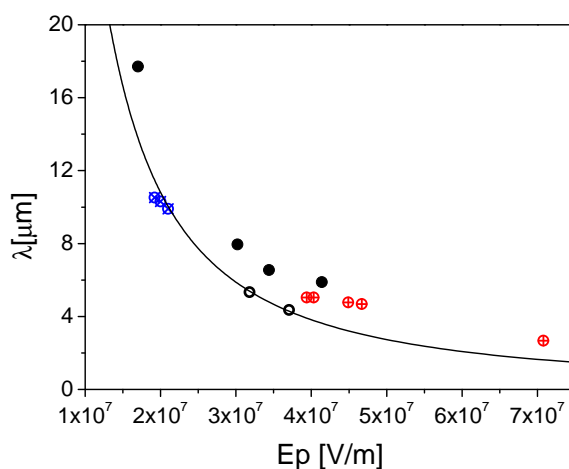


Figure 4.12: Characteristic wavelength as a function of the applied electric field for (●) as-spun and films annealed for (⊕) 1 hr (⊗) 10 hrs and (○) 140 hrs at T_{anneal} . Line shows the prediction of equation 4.3.

of λ for films annealed for 1 hr and 10 hrs at T_{anneal} prior to destabilisation. The recovery of bulk behaviour here is observed much faster than the recovery of bulk viscosity.

It has been shown that non-equilibrium chain conformations result in additional in-plane stresses in spin-cast films [116]. These are seen to drive destabilisation and hole formation in dewetting experiments [106]. Assuming that the same in-plane stresses are present in these films, they should also act as an additional driving force, resulting in smaller values of λ and faster τ . This however, is not seen. The larger values of λ in the as-cast films are instead indicative of a stabilising pressure acting on the as-cast films. A similar effect was observed by Barbero for PS $M_w = 113 \text{ kg mol}^{-1}$ and 27.5 kg mol^{-1} [110].

One possible explanation for the behaviour observed in the as-cast films is frozen-in normal stresses. These could result from strong solvent gradients during spin coating, which lead to a variation in the entanglement density of the chains normal to the film surface. Polymer adsorption at the substrate could also give rise to a non-equilibrium conformation at the polymer/substrate interface.

A comparison of the characteristic wavelength of the instabilities for as-spun PS films with $M_w = 4000 \text{ kg mol}^{-1}$ and 200 kg mol^{-1} can be seen in figure 4.13a. Films

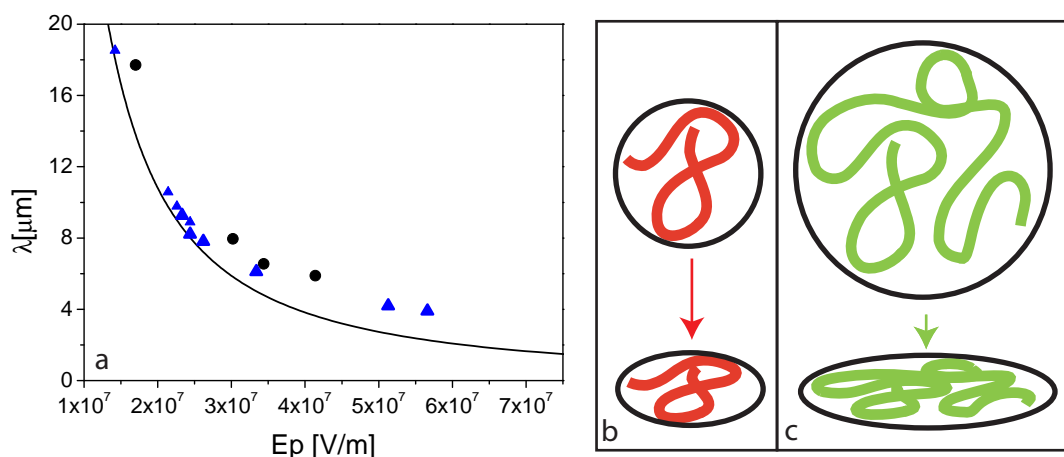


Figure 4.13: (a) Characteristic wavelength of instabilities as a function of the applied electric field for as spun films. (●) PS4000 and (▲) PS200. Schematic representation of the deformation of a polymer chain swollen in toluene with a given density of segments on loss of the solvent for (b) a low molecular weight and (c) a higher molecular weight polymer.

spun from PS200 have a reduced wavelength compared to those spun from PS4000. Shorter wavelength instabilities, for both polymers, are observed to have a greater deviation from bulk behaviour than longer-wavelength instabilities. Bulk behaviour is observed for PS200 for $\lambda > 15 \mu\text{m}$.

Longer-wavelength instabilities are observed for smaller applied electric fields and have increased onset times as compared to shorter-wavelength instabilities. The films are heated above T_g during the incubation time before instability onset. From equation 4.2 it can be seen that longer wavelengths imply much greater incubation times before instability onset, giving the film more time to relax stresses arising from spin-coating. For PS200 relaxation of the frozen-in stresses occurs on much shorter timescales than for PS4000.

The data shown in figure 4.13a are in agreement with the hypothesis that frozen-in normal stresses are responsible for the non-equilibrium behaviour observed here, since the magnitude of the stresses is greater for the higher molecular weight polymer. Consider the liquid films during the spin coating process just prior to vitrification. Taking first the PS200, each chain can be considered to occupy a sphere of radius r_{200} with a given segment density. After vitrification the remaining solvent evaporates

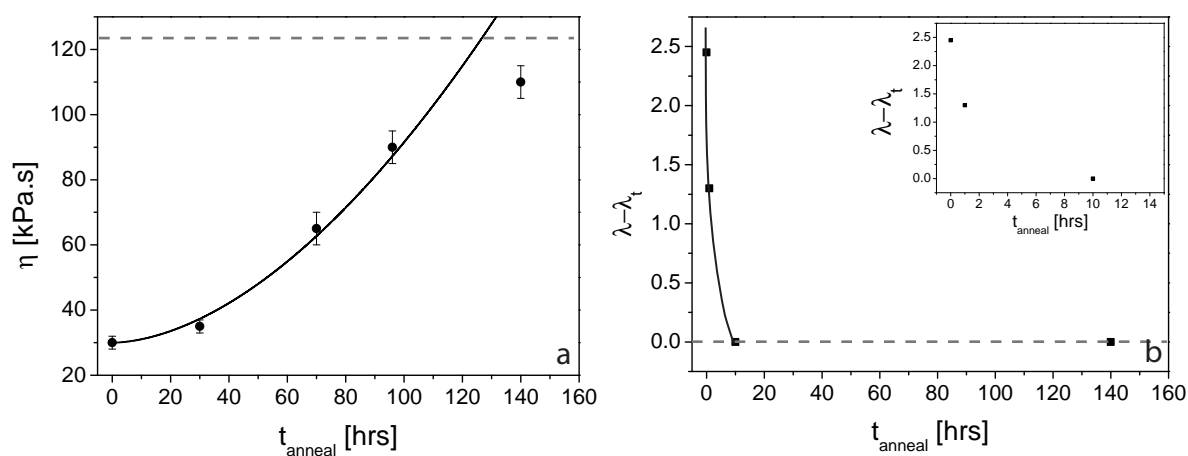


Figure 4.14: Relaxation behaviour of (a) the viscosity for PS200 and (b) the residual stresses for PS4000 as a function of the annealing time. Dashed lines indicate bulk equilibrium behaviour.

and the chains collapse. This is shown schematically in figure 4.13b. Assuming the same segment density for PS4000 prior to vitrification each chain will occupy a sphere with radius $r_{4000} > r_{200}$. On evaporation of the remaining solvent, a larger distortion of the chains will occur (see figure 4.13c), resulting in a greater anisotropy within the film. The distortion of the chains in PS4000 is associated with a bigger change in the free energy than that of PS200 and therefore increased stresses in the film.

Time constants

The relaxation behaviour of the viscosity and the residual stresses are shown in figure 4.14. The points are taken from the data shown in figure 4.11 and figure 4.12 respectively. The annealing time required to remove residual stresses in PS4000 is on the order of a few hours, much shorter than that needed to recover bulk viscosity in the film.

The results suggest that stresses in the film can be removed by local rearrangement of the chains, which happens on relatively short timescales. Recovery of bulk viscosity however, requires complete equilibration of the chains and therefore longer annealing times. A stress free film can exist when the chains are still far from equilibrium. The relatively small deviation in the measured λ compared to that predicted by equation 4.3, shows that the chains are not very strongly distorted. The deviation in

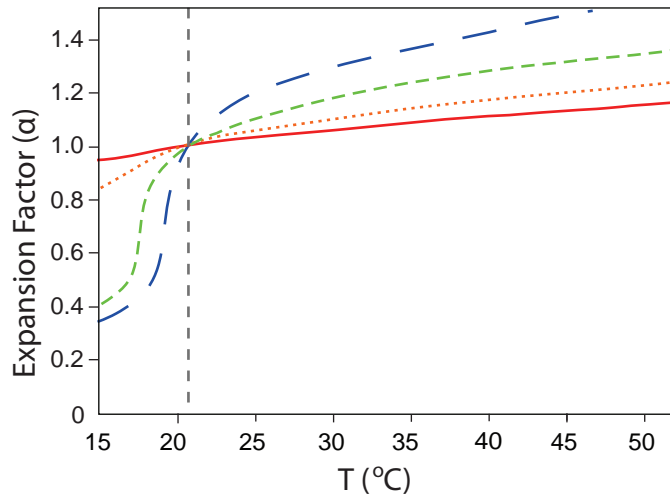


Figure 4.15: Chain conformation of PS chains in TD as a function of the solution temperature. $M_w =$ (solid) 200 kg mol^{-1} (dotted) 1000 kg mol^{-1} (short-dash) 4000 kg mol^{-1} (long-dash) $16800 \text{ kg mol}^{-1}$.

viscosity is much larger indicating that the chains are far from equilibrium. Note that the reptation times for PS4000 at $175^\circ\text{C} \approx 3 \cdot 10^4 \text{ s}$ and for PS200 at $175^\circ\text{C} \approx 4 \text{ s}$ [117] are much smaller than the relaxation time required for full equilibration of the films, also indicating the non-equilibrium nature of the spin-cast films. This will be discussed further in section 4.2.4. The relaxation of the residual stresses for PS4000 is on the order of the reptation time.

4.2.2 Trans-decalin

Trans-decalin is a θ -solvent with a θ -temperature $\theta_T \approx 21^\circ\text{C}$. Below θ_T PS is not soluble in TD and falls out of solution. Increasing the temperature above θ_T increases the solubility of PS, with TD behaving as a good solvent at sufficiently high temperatures.

For a θ -solvent the degree of swelling of the chains is a function of the temperature of the solution [118]. The dependency is given by

$$\left[\frac{14}{3N\alpha_{\min}^3}(\alpha^3 - \alpha^5) + \frac{2}{3} \frac{\alpha_{\min}^3}{\alpha^3} \right] / \sigma = \frac{\theta}{T} - 1 \quad (4.4)$$

where $\alpha = \langle R_g^2 \rangle^{1/2} / \langle R_0^2 \rangle^{1/2}$ is the expansion factor, R_0 is the radius of gyration under

ideal melt conditions, α_{\min} is the volume of the chains in the fully collapsed state and σ is defined as $\sigma = 1 - \Delta S/k_B$ with ΔS being the entropic change associated with segment-segment interaction of the polymer.

Figure 4.15 shows the change in conformation of the PS chains as a function of the solution temperature for various molecular weights of PS. Below θ_T , TD acts as a poor solvent. The attractive intramolecular forces dominate and the chain contracts forming a collapsed globule. The radius of gyration of the polymer follows [119]

$$R_g \sim N^{1/3} \left| \frac{T}{\theta} - 1 \right|^{-1/3} \quad \text{for } T < \theta \quad (4.5)$$

Above θ_T TD acts as a good solvent, the chains appear swollen and the volume they occupy increases. In this case interactions between the monomers and the solvent dominate over intramolecular forces. The conformation of the coils is described by

$$R_g \sim N^{3/5} \left| \frac{T}{\theta} - 1 \right|^{1/5} \quad \text{for } T > \theta \quad (4.6)$$

At θ_T intermolecular polymer-solvent repulsion exactly balances intramolecular monomer-monomer attraction. Under these conditions the polymer behaves like an ideal chain with

$$R_g \sim N^{1/2} \quad \text{for } T = \theta \quad (4.7)$$

Due to this ability to change the polymer-solvent interactions PS solutions in TD provide a tuneable system, allowing the conformation of the chains to be easily adjusted. By varying the temperature at which the films are prepared the effect of the initial coil conformation in the solvent on the properties of the films can be studied. Toluene is a very good solvent and can therefore be compared to trans-decalin solutions at very high temperatures.

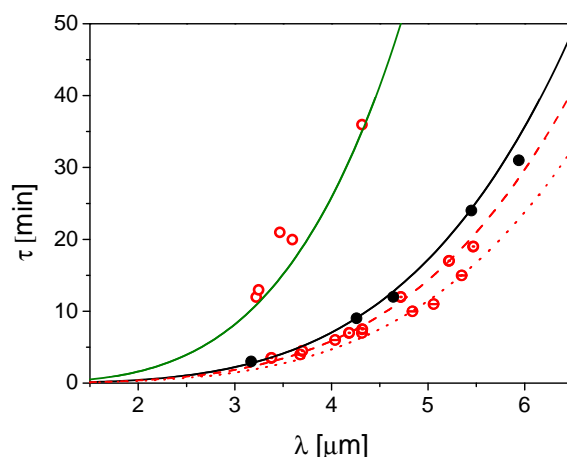


Figure 4.16: Characteristic destabilisation time τ vs λ for as-spun films spun from (●) toluene, trans-decalin at (⊙) 55 °C and (⊖) 25 °C and (○) annealed films spun from trans-decalin. Lines show fits to the data using equation 4.2.

Film rheology – solvent effects

Figure 4.16 shows a comparison of τ for films spun from trans-decalin(TD) at $\sim 25^\circ\text{C}$ (TD25) and $\sim 55^\circ\text{C}$ (TD55) and those spun from toluene. A clear difference in the onset time for the three sets of films is observed.

The onset of destabilisation is observed at shorter times in films spun from TD than in films spun from toluene as shown in figure 4.16. For films spun from TD, the onset time depends on the temperature at which the films were prepared, with films prepared at 55 °C (TD55) having longer onset times than those prepared at 25 °C (TD25). Annealing of TD films at $T_{\text{anneal}} = 155^\circ\text{C}$ for 140 hrs results in a recovery of bulk behaviour. The unannealed data are described well by equation 4.2, assuming $\eta = 25 \text{ kPa} \cdot \text{s}$ for TD55 and $\eta = 20 \text{ kPa} \cdot \text{s}$ for TD25. These results are in agreement with the hypothesis that non-equilibrium chain conformations give rise to a reduced viscosity.

From equation 4.4 and figure 4.15 it can be seen that for PS in toluene the chains will be swollen, while for PS in TD at 25 °C the radius of gyration of the chains is reduced. In [7] the reduced viscosity of toluene is explained in terms of entanglements of the polymer chains. In the initial stages of spin coating, once the concentration

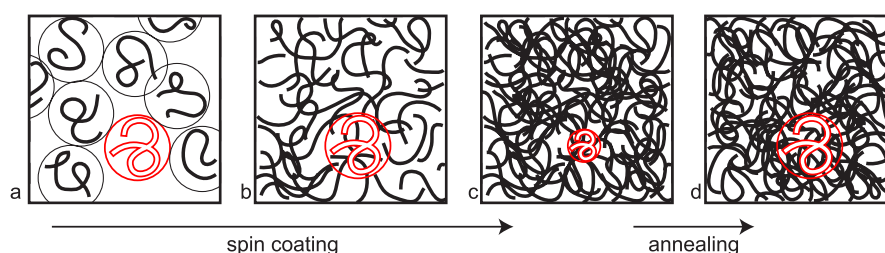


Figure 4.17: Schematic representation of the model used to describe the reduction in the effective viscosity in spin-cast films. (a) Starting from a semi-dilute solution, (b) solvent evaporates and the chains start to entangle as the concentration increases. (c) The slowdown and collapse of the chains for high polymer concentrations prevents the full equilibration of the chains. Thermal annealing equilibrates the chains, restoring the melt entanglement density (d). Figure taken from [7].

of PS reaches the overlap concentration, the PS can be described as being in a semi-dilute solution in toluene, a good solvent. At this point entanglement of the chains starts to occur. As the solvent evaporates the polymer concentration in the liquid film increases, which leads to an increasingly entangled semi-dilute solution. The increase in entanglements occurs via chain reptation. As the solvent concentration decreases, so the mobility of the chains decreases. Chain reptation is progressively slowed and stops upon vitrification of the polymer. The resulting entanglement density of the chains is lower than that in a polymer melt at equilibrium. This is shown schematically in figure 4.17. Melt viscosity comes from the entangled nature of the chains. A lower entanglement density can therefore be used to explain the lower effective viscosity observed here.

For PS in trans-decalin at $T \sim \theta_T$ the behaviour is similar now however, the PS is in a near- θ solvent. As the solvent evaporates the PS will again form a semi-dilute solution however, the polymer concentration at which this occurs is higher than that for a good solvent due to the reduced R_g of the polymer. Once the overlap concentration is reached, the chains start to entangle, with the entanglement density increasing with polymer concentration. For toluene, vitrification occurs when the concentration of solvent in the film decreases to $\varphi_{\text{solvent}} \sim 0.23$ (see table 4.1). For TD at θ_T this occurs at $\varphi_{\text{solvent}} \sim 0.46$ resulting in a lower entanglement density of the chains and a reduced

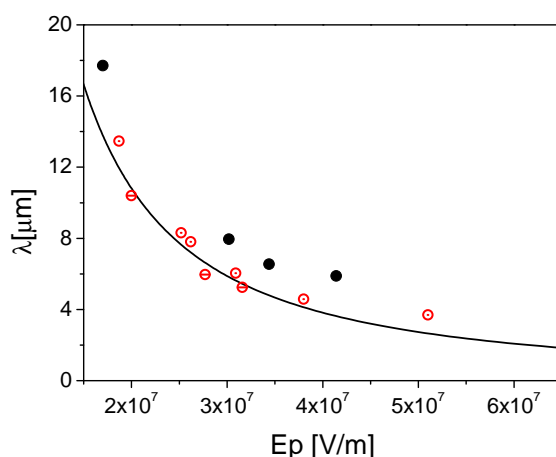


Figure 4.18: Characteristic wavelength of instabilities for as-spun films prepared from (●) toluene (○) TD25 and (○) TD55. Line shows the prediction of equation 4.3.

effective viscosity. For PS in TD spun at 55 °C vitrification occurs at $\varphi_{\text{solvent}} \sim 0.3$ which lies between that of TD25 and toluene.

Residual stress – solvent effects

Figure 4.18 compares λ as a function of the applied electric field for films spun from TD and toluene. Instabilities formed in films prepared from TD have smaller wavelengths than those prepared from toluene, with TD25 exhibiting bulk behaviour.

The time taken for film formation depends on the boiling point of the solvent from which the polymer is cast and the vapour content of the atmosphere in which the film is spun. Here the films were spun under nitrogen flow with no solvent vapour. Film formation from toluene solutions was on the order of 5-10 s and for TD 30-45 s, with films spun from TD55 forming slightly faster than those spun from TD25. These results suggest that frozen-in normal stresses due to solvent gradient effects are responsible for the increased wavelength observed in as-spun films as seen in figure 4.12 and figure 4.18. The difference in the dependency of λ on the applied electric field can be explained by considering the boiling points of the solvents. TD has a much higher boiling point than toluene, this results in a slower evaporation of the solvent and increased film formation time. This, in turn allows more time for the chains to relax, resulting in smaller frozen-in normal stresses within the film.

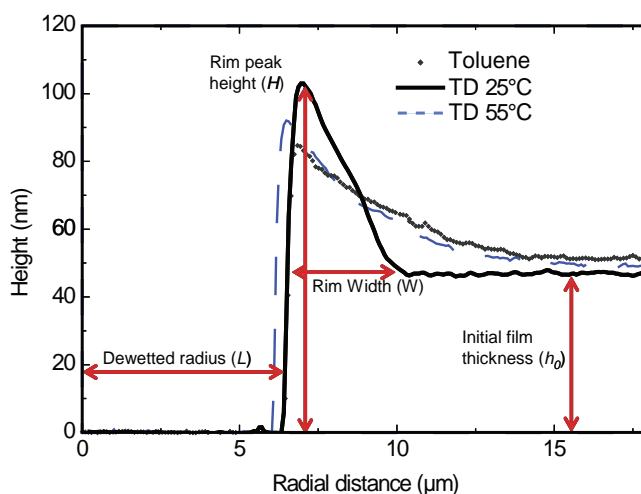


Figure 4.19: Rim profiles of holes formed in films spun from toluene, TD25 and TD55. Profile taken when hole radius L was $6 \mu\text{m}$.

Comparison with dewetting experiments

In tandem with these experiments Raegen and Reiter at the University of Freiburg have been investigating the dewetting behaviour of spin-cast films spun from toluene and TD. In these experiments 40 nm PS films $M_w = 4000 \text{ kg mol}$, $M_w/M_n = 1.15$ were spun onto PDMS coated silicon wafers. The thickness of the PDMS layer was $\sim 10 \text{ nm}$. The films are intrinsically unstable and when heated above T_g to $T_{\text{exp}} = 125 \text{ }^\circ\text{C}$ dewet the substrate through the formation and growth of holes.

These experiments are not yet complete. However, in the context of the results shown here for the EHD instabilities it is interesting to note some of the findings so far. The first relates to the rim profiles of the holes formed in the dewetted films. These are shown in figure 4.19. The profiles are taken at a hole radius of $6 \mu\text{m}$. Both the rim peak height H and the rim width W are seen to vary as a function of the casting solvent. Holes which form in toluene have the lowest H and widest W , with the highest H and narrowest W being seen in films formed from TD25. TD55 lies in between the two data sets. The rim height is given by

$$H = h_0 + \frac{|S|}{E} \left(1 + \frac{h_0}{S} \sigma_0 \right) \quad (4.8)$$

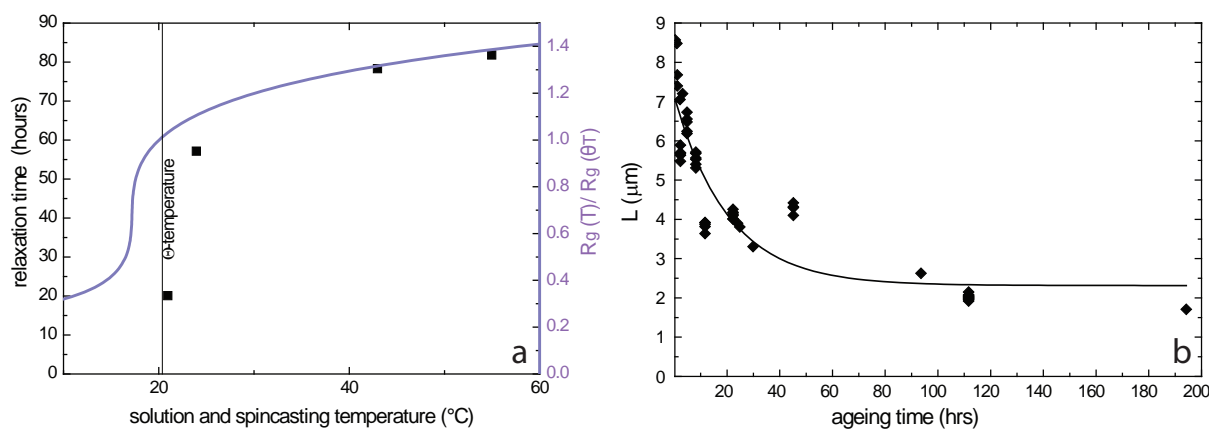


Figure 4.20: (a) Relaxation time as a function of the temperature at which the films were spun from TD. The curve us plotted using equation 4.4. (b) The radius of the hole taken at 480, 1020, 1500 s for TD. The decrease in radius follows an exponential decay, which reflects the relaxation of the chains in the film at room temperature.

where S is the spreading coefficient, σ_0 is the stress in the film and E is the modulus. From equation 4.8 it can be seen that the differences observed in H could result from increased stresses in the film and/or a smaller modulus, both of which result from non-equilibrium conformations of the chains. The rim profiles suggest that the modulus is greatest in films cast from toluene and smallest in films cast from TD25. This is in agreement with the data shown in figure 4.16, where a lower effective viscosity is measured in TD25 as compared to films cast from toluene.

The second interesting observation relates to the relaxation time as a function of the casting solvent. The results are shown in figure 4.20a. The relaxation time is taken to be the time at which the width of the rim stops increasing and reaches a plateau as shown in figure 4.20b. Figure 4.20a clearly shows a dependency of the relaxation time on the conditions under which the film is cast. This suggests that the change in relaxation time comes either directly from the variation in the temperature or indirectly from the dependence of the coil conformation of PS on the solution temperature. Figure 4.20a shows that the relaxation times mimic the behaviour in the amount of swelling, suggesting that this plays an important roll. However, as discussed earlier, the film formation time and the vitrification point must also be considered.

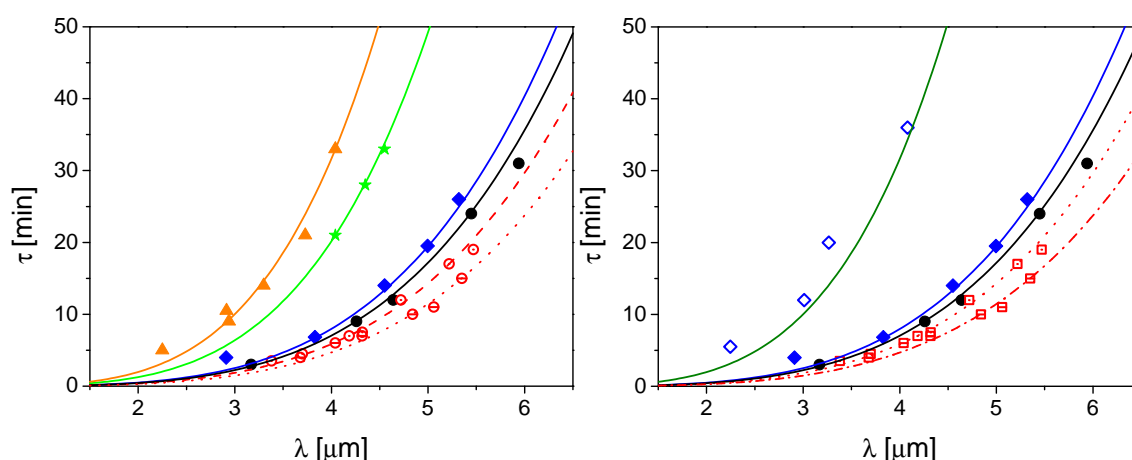


Figure 4.21: Characteristic onset time τ for films spun from (\blacktriangle) THF, (\blackstar) MEK, (\diamond) chloroform, (\bullet) toluene, (\odot, \ominus) TD solutions. Solid symbols represent as-spun films. Outlined symbols represent films annealed at T_{anneal} for 140 hrs.

As shown in figure 4.13b the residual stresses are likely to be smaller in magnitude in TD25 than in TD55 due to the smaller R_g of the chains. It is therefore expected that the stresses will relax more quickly in TD25 than in TD55 as shown in figure 4.20a. It should be noted that the relaxation time measured by Raegen and Reiter is considerably longer than that shown in figure 4.12. This is because their films were aged at room temperature, while those studied here were annealed at $T > T_g$. It should also be noted that the dewetting experiments and EHD experiments probe different residual stresses within the films. The effect of the coil size in solution on the magnitude of these stresses is however the same.

4.2.3 Chloroform, MEK and THF

Film rheology – a few more solvents

Tetrahydrofuran (THF), methylethylketone (MEK) and chloroform were also used as casting solvents for spin coating PS films. The characteristic onset times for destabilisation, for films formed from these solvents, are shown in figure 4.21. Films cast from chloroform, MEK and THF show an increased effective viscosity as compared with those cast from toluene. The effective viscosities of the films determined from

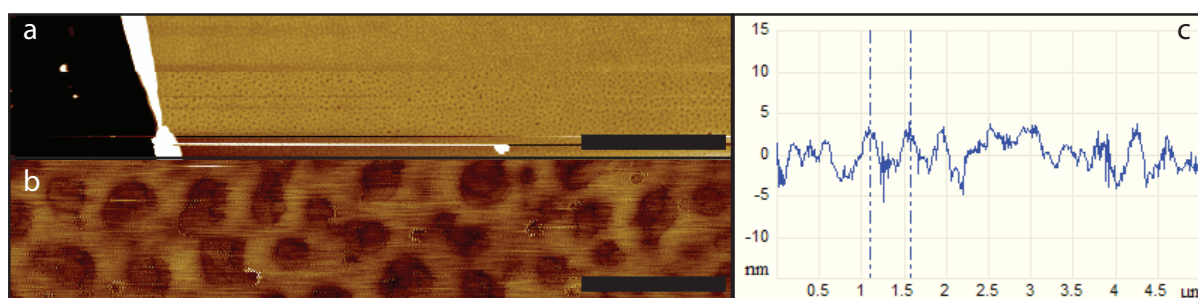


Figure 4.22: (a,b) AFM micrographs of a film spun from THF. (c) Cross-section showing surface roughness. Section taken from (b). Scale bar is (a) 20 μm (b) 2 μm .

the data in figure 4.21 are 34 $\text{kPa} \cdot \text{s}$, 86 $\text{kPa} \cdot \text{s}$ and 135 $\text{kPa} \cdot \text{s}$ for chloroform, MEK and THF respectively.

Maron *et al.* compared the interaction parameters of PS in chloroform, MEK and toluene [120]. Chloroform has an increased solvent quality for PS as compared to toluene, with MEK having a strongly reduced solvent quality. The R_g of PS in chloroform should therefore be greater than that in toluene, allowing for entanglements of the chains to occur at higher solvent concentrations. This was confirmed with dynamic light scattering measurements of PS solutions in the different solvents, where the concentration of PS was much less than the overlap concentration. The chains were found to be more swollen in chloroform than in toluene. For MEK and THF, the chains were more compact and had a R_g close to that of PS in TD near θ_T . Table 4.1 shows that vitrification of PS in chloroform occurs at $\varphi_{\text{solvent}} \sim 0.32$ compared to $\varphi_{\text{solvent}} \sim 0.23$ for toluene, freezing in the chains earlier. This suggests that while both the initial conformation of the chains in the solvent and the amount of solvent remaining in the film when it become glassy are important when considering the non-equilibrium behaviour of the film, the solvent quality dominates.

As shown in figure 4.21, the chloroform data fit with the trend observed in the toluene and TD data. The onset times for destabilisation of films spun from MEK and THF however, do not. MEK and THF are much poorer solvents for PS and have very low boiling points. This resulted in small thickness variations across the surface

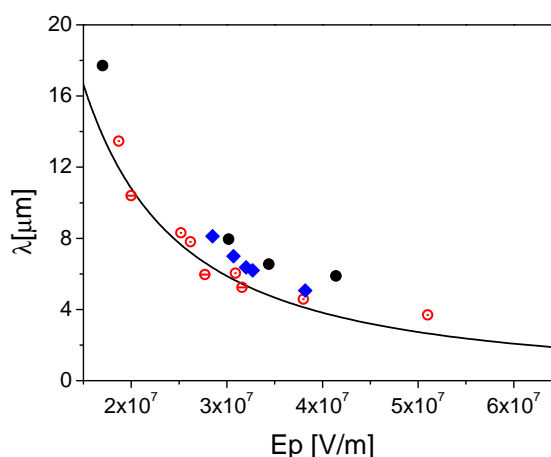


Figure 4.23: Characteristic wavelength of destabilisation as a function of the applied electric field for films spun from (◇) chloroform, (●) toluene and (○, ⊖) TD solutions.

of the film as shown in figure 4.22. The unexpected behaviour observed in these films may result from the electric field coupling into the instabilities already present in the film, influencing both the onset time and the wavelength. As a result the behaviour of films spun from MEK and THF were not considered further.

Residual stress – a few more solvents

Figure 4.23 shows the characteristic λ of the instabilities for films cast from the different solvents. Again a higher λ is observed in the as-cast films spun from chloroform than expected for equilibrated films. Chloroform is a better solvent for PS than either toluene or TD, resulting in an increased swelling of the chains. Chloroform also has a much lower boiling point than the other two solvents with film formation taking ~ 1 s. It would therefore be expected that the stresses in films formed from chloroform would exhibit increased stresses. This is not seen indicating that other parameters must also be considered.

Role of the coil size, vitrification point and solvent boiling temperature

It is clear from the data shown in figure 4.21 that no one property of the system is responsible for the behaviour observed in the films. Instead it is a combination of a number of factors: φ_{solvent} , T_b and the solvent quality. These all need to be taken into

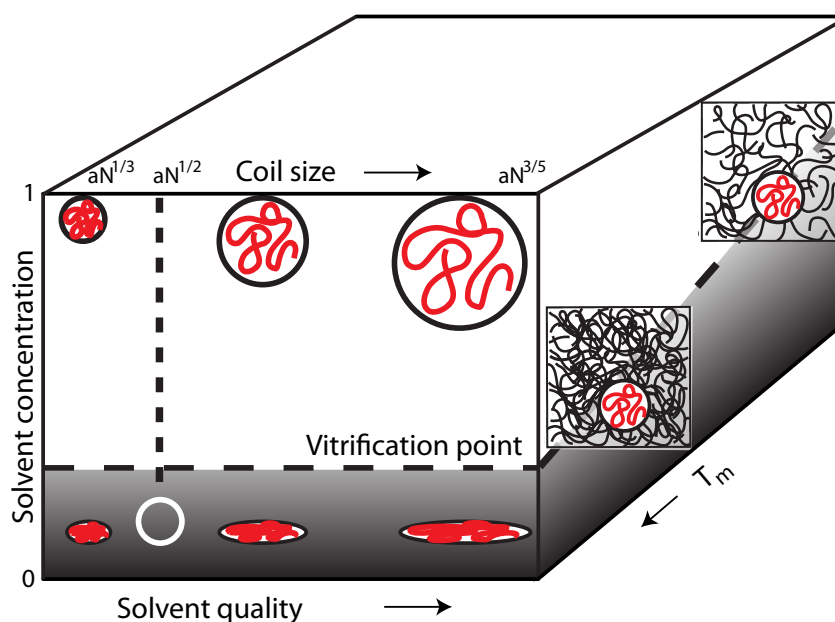


Figure 4.24: Schematic representation of the effect of changing the solvent quality and the concentration of solvent remaining in the film at vitrification on the conformations of the chains in the spin cast film.

account, when considering the final conformations of the chains in as-spun films.

The effect of each of these parameters is shown in figure 4.24. The solvent quality changes the size of the coils, with chains in a good solvent having a greater radius of gyration than those in a poor solvent due to swelling of the chains. Taking the idealised case where the vitrification point for each solvent is the same, by tuning solvent quality the anisotropy of the chains in the final film can be tuned, with those spun from a good solvent having a greater distortion and therefore higher residual stress in the film.

Experimentally the melting temperatures of the solvents vary from -95 to -31 °C changing the concentration of solvent which remains in the film on vitrification. The higher the melting temperature, the more solvent there is in the film when the chains are frozen in and the lower the entanglement density of the chains in the final film. Therefore for higher melting temperature solvents, a lower effective viscosity will be measured.

Although not shown in the diagram, the boiling point of the must also be taken in

to account. The higher the boiling point, the faster the film formation process. Consider two solvents with the same vitrification point and where the PS has the same coil size. Changing the boiling point changes the time that the chains have to reptate before the conformations are frozen-in. A higher boiling point solvent would therefore have a lower entanglement density and be further from equilibrium. However, as shown in the experiments the solvents all have different properties and the parameters cannot be isolated in this way. Instead they all interact with each other and must be considered together.

4.2.4 Vapour annealing

As shown in figure 4.11 bulk viscosity of the films is recovered on annealing of the films at $T_{\text{anneal}} > T_g$ for sufficiently long times. The annealing time needed for equilibration of the films is much longer than the reptation time of the polymers τ_{rep} , where τ_{rep} is the characteristic time for tube renewal of a Gaussian coil in an equilibrated melt.

The reptation model predicts that polymer chains reach an equilibrium state at timescales on the order of τ_{rep} . The results shown here and by Barbero *et al.* [7] seem to contradict this idea. These results are in good agreement with other experimental observations which show that equilibrium properties in thin films are obtained after annealing at $T > T_g$ for $\tau \gg \tau_{\text{rep}}$ [102, 103]. However, the reptation model does not apply to spin-cast films. The reptation model only applies to fully equilibrated chains. The results here show that as-cast films have quenched conformations far from equilibrium, which cannot be equilibrated by a standard reptation process. Quake has shown that chains which have internal entanglements, known as knots, have relaxation times much greater than the reptation time of the chains [121]. Branched and star polymers also have much longer equilibration times, here instead of reptation, the polymer is localised at the branch point until the different arms have fully relaxed

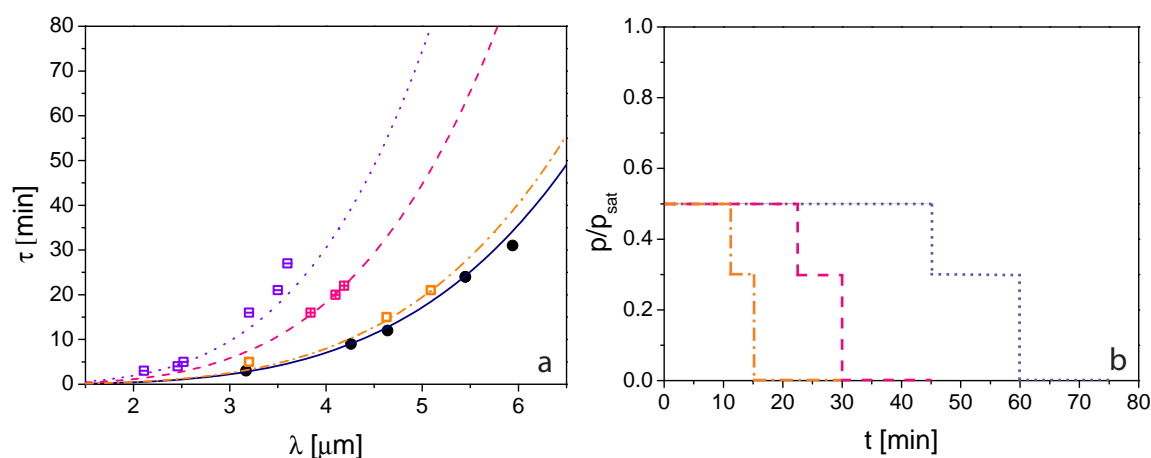


Figure 4.25: (a) Characteristic onset time for EHD destabilisation for vapour annealed films spun from PS $M_w = 200 \text{ kg mol}^{-1}$. (\square) $t_{\text{total}} = 60$ min, (\boxtimes) $t_{\text{total}} = 30$ min and (\square) $t_{\text{total}} = 15$ min. (b) Solvent vapour annealing conditions for (dashed-dot line) $t_{\text{total}} = 15$ min (dashed line) $t_{\text{total}} = 30$ min (dotted line) $t_{\text{total}} = 60$ min.

to the branch point [122]. It may be that some combination of these needs to be considered when describing the equilibration of the chains in spin-cast films.

An alternative to thermal annealing is solvent vapour annealing. During this process the polymer films are placed in a solvent-rich atmosphere. The polymer film then swells due to the presence of the solvent, with the amount of swelling being dependent on the concentration of solvent in the atmosphere. Here PS films, spun from toluene, were annealed at $T = 20^\circ\text{C}$ in a toluene atmosphere with a vapour pressure of $p/p_{\text{sat}} = 0.5$ for time $t_1 = \frac{3}{4}t_{\text{total}}$. The vapour pressure was then reduced to $p/p_{\text{sat}} = 0.3$ for time $t_2 = \frac{1}{4}t_{\text{total}}$. Finally, the film was quenched to remove all the solvent under N_2 flow for 15 min. Figure 4.25 shows the characteristic onset time for films which were vapour annealed for $t_{\text{total}} = 15, 30$ and 60 min prior to destabilisation.

From figure 4.25 it can be seen that vapour annealing allows full equilibration of the films on much shorter time scales than those required for thermal equilibration. After 1 hr of vapour annealing the films have recovered their bulk viscosity. The effective bulk viscosities for 30 min and 15 min as measured by fitting the data using equation 4.2 are $78 \text{ kPa} \cdot \text{s}$ and $32 \text{ kPa} \cdot \text{s}$ respectively. This shows that changes in the chain conformation occur after minutes of vapour annealing compared to hours for ther-

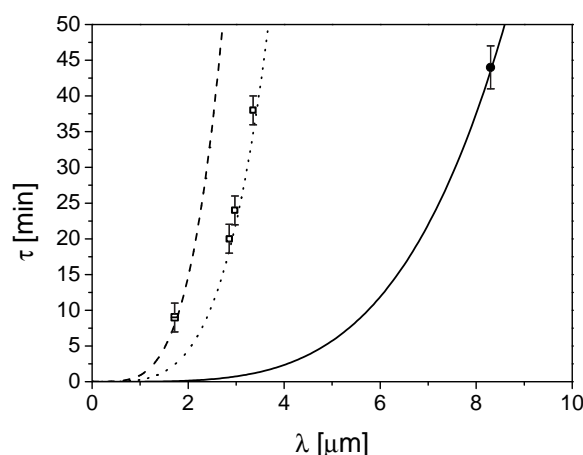


Figure 4.26: Characteristic onset time for PS655. (●) As-cast and vapour annealed films (□) $t_{\text{total}} = 1$ hr and (⊞) $t_{\text{total}} = 2$ hr. Lines show fits to the data using equation 4.2. The dashed line shows the predicted behaviour using the bulk viscosity of the polymer.

mal annealing (see figure 4.11). This is most likely due to the increased mobility of the chains.

For high molecular weight polymers, thermal equilibration of the films is not achievable on technological timescales. For PS $M_w = 655$ kg/mol Barbero found the effective viscosity of the as-cast films to be 0.2 kPas, three orders of magnitude smaller than the bulk value of 1.3 MPas. The results in figure 4.25 suggest that vapour annealing of high M_w polymers provides an alternative method for equilibration of the films on easily accessible timescales.

Figure 4.26 shows the characteristic onset time for EHD instability formation for as-spun and vapour annealed films of PS655. Vapour annealing was carried out for $t_{\text{total}} = 1$ hr and $t_{\text{total}} = 2$ hrs. The curves show fits to the data assuming viscosities of $10 \text{ kPa} \cdot \text{s}$ for the as-cast film and $300 \text{ kPa} \cdot \text{s}$ for films vapour annealed for 1 hr. Full equilibration and a recovery of bulk viscosity is achieved after 2 hrs of vapour annealing time. The results show that equilibration of high molecular weight polymers is possible on much shorter timescales by vapour annealing of the films as compared to thermal annealing at $T > T_g$.

4.3 Conclusions

An electric field has been used to weakly perturb the surface of 100 nm thick PS films cast from various solvents. For films spun from toluene a strong increase in the mobility of the film is observed in as-cast films, corresponding to a reduced effective viscosity of the film. Annealing of the films at $T > T_g$ for sufficiently long times reduces the mobility of the film and restores the viscosity to that of the bulk polymer.

A similar reduction is seen for films spun from trans-decalin. The measured effective viscosity for films spun from trans-decalin is less than that of films spun from toluene. Trans-decalin is a θ -solvent and the viscosity reduction in as-cast films is seen to depend on the temperature at which the films were spun. Again annealing of the films above T_g for long times results in a reduction of the film mobility to that expected from bulk rheology.

The mobility increase observed in the as-cast films can be explained in terms of non-equilibrium chain conformations caused by the film preparation. Spin-coating results in a lower entanglement density of the chain compared to a polymer melt at equilibrium and therefore a reduced effective viscosity. The difference between the films spun from toluene and from trans-decalin can be explained by the changes in the chain conformations in the initial solutions and the amount of solvent remaining in the film at vitrification.

Films spun from chloroform were also seen to have an increased mobility in the as-cast films as compared to the bulk behaviour. Chloroform is a better solvent for PS than toluene, implying that the chains in the initial solvent will be more swollen. However, films spun from chloroform vitrify at higher solvent concentrations. This suggests that the solvent quality strongly effects the non-equilibrium properties of spin-cast films.

The experiments show that instabilities in as-cast films have a higher λ than predicted theoretically, indicating a weak stabilising pressure in the films. These could

arise from frozen-in normal stresses in the as-cast films. The wavelength is seen to be greatest for films spun from toluene and smallest for films spun from trans-decalin, with films spun from trans-decalin at 25 °C exhibiting bulk behaviour. This suggests that spin coating results in an asymmetric deformation of the polymer chains, perhaps due to solvent evaporation after vitrification. The deformation is dependent on the conformation of the chain prior to vitrification and the molecular weight of the polymer.

These frozen-in stresses can be removed by annealing of the films above T_g on much shorter timescales than those required to restore bulk viscosity. This suggests that the stresses can relax while the films are still far from equilibrium. Local rearrangements of the chains are sufficient to remove the anisotropy responsible for the residual stress.

The results indicate that the boiling point of the solvent, the film formation time, the solubility of PS in the solvent and the amount of solvent remaining in the film on vitrification are all important. No one property can be used to consistently describe the trends observed in the data. Instead the behaviour observed results from a combination of all of these parameters.

RESIDUAL STRESS IN THIN POLYMER FILMS

In chapter 4 it was shown that the process of spin coating results in the formation of films with non-equilibrium chain conformations and residual stresses. The wavelength of the instabilities formed using electrohydrodynamic destabilisation of the polymer films yields information about the force balance in the film and at the surface, but not the overall magnitude of the stress in the film. The evaluation of residual stresses is of great importance in the context of technological applications, where stresses play a role in the adhesive and cohesive properties of the film along with their stability.

Stresses in thin films are typically measured by coating a cantilever with the material of interest and observing the cantilever deflection [123, 124]. The first experiments using this technique were carried out by Stoney in 1909 [125]. Thin metallic nickel films were deposited by electrolysis onto steel rules. After deposition a deflection of 3-4 mm was observed in a rule of length \times width \times thickness = 102 \times 12 \times 0.32 mm.

While widely used to study the stresses in inorganic materials, cantilever deflection has also been used to investigate the stresses in polymer films. Ree *et al.* measured the stresses in spin-coated polyimide films on polished silicon wafers [126]. They

Physical phenomena of thin surface layers

used a wafer bending technique, where the deflection was measured using laser light beams. They found stresses on the order of 11.2–26.8 MPa for as spun films with thicknesses of 10 μm . For polystyrene and polyisobutylmethacrylate (PIBM) films blade-coated onto thin steel cantilevers, Croll found the residual stress to be 4.5 MPa for PIBM and 14.3 MPa for polystyrene films [127, 128]. This was found to be independent of the coating thickness for films of 1 – 100 μm .

Although a well established method, this technique requires that the cantilever is formed prior to film deposition and measures the stresses in large area films. Micro-scale cantilevers are used in microelectromechanical systems (MEMS). The fabrication process of these cantilevers typically involves undercutting the cantilever structure to release it using a wet or dry etching technique [129]. Such cantilevers have been used to study the stresses in thin-metallic films sputtered or evaporated onto their backside.

In this chapter, stresses in 100 nm thick polystyrene films are investigated using cantilever deflection. The films are spun onto silicon nitride membranes. Focused ion-beam milling is used to cut cantilevers into the bilayer structures. The deflection of the cantilevers is monitored by scanning electron microscopy.

Focused ion-beam milling has been used by a number of groups to measure residual stresses in thin films [130, 131]. Typically a shape is milled out of the material and the deformation of the structure is monitored using digital image correlation. The deformation is used to calculate the residual stresses. This technique allows the stress in the films to be probed locally and on much smaller length scales than previously studied in polymer films. It also enables the film to be spin coated, which would not be possible on pre-formed MEMS cantilevers.

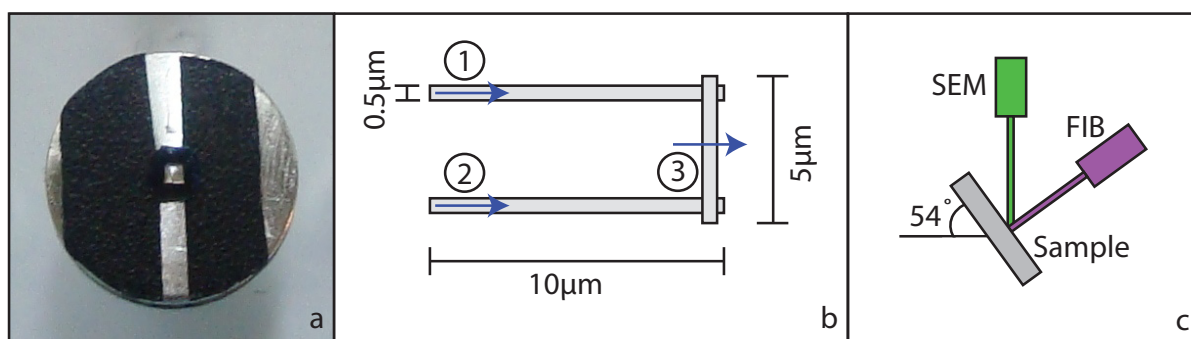


Figure 5.1: (a) Membrane sample mounted on SEM stub. (b) A schematic representation of cantilevers milled using FIB. Numbers and arrows indicate the order in which the edges were milled and the direction of milling. (c) Orientation of sample with respect to ion and electron beams.

5.1 Materials and methods

Polystyrene (PS) $M_w = 4000 \text{ kg mol}^{-1}$, $M_w/M_n = 1.15$ (Polymer Standards Service) was used as obtained without further purification. Films with a thickness of 100 nm were spun from toluene at a spin speed of 4500 rpm onto 100 nm thick low stress Silicon-Nitride (SiN) membranes with a 0.5 mm window supported on 200 μm TEM grids (SPI supplies).

Focused ion beam milling

Focused ion beam (FIB) milling is a commonly used method for the structuring of surfaces on the micron scale [132]. Here a Carl Zeiss 1540 XB CrossBeam FIB/SEM system was used to mill cantilevers into the SiN membranes and SiN/PS bilayers. The substrates were mounted onto SEM stubs using carbon tape, such that the substrates were free standing and no air was trapped underneath the membrane (figure 5.1a). Cantilever structures were milled using a 30 keV ion-beam at a current of 100 pA. The ion-beam was orientated normal to the sample surface. Imaging was carried out using SEM with a 7 keV electron beam at an angle of 54° to the sample surface. It should be noted that the FIB was used only to mill the cantilevers and not to image the membranes.

Unlike SEM (see chapter 6) FIB is inherently destructive to the sample. The ion beam is focused into a small spot size and scanned across the sample surface. As the beam is scanned it removes atoms from the surface, where the number of atoms removed depends on the beam current (dose) and the material being milled. By defining where the FIB scans, milling can be localised to these areas. Figure 5.1 shows a schematic representation of the cantilevers that were milled. The approximate dimensions, the order in which the edges were milled and the direction of milling are all indicated. Each shape was milled for 60 s. This was sufficient to mill through the whole thickness of the SiN/PS bilayer.

5.2 Results and discussion

Figure 5.2a,b shows micrographs of the cantilevers milled in the PS coated silicon nitride membranes. The two cantilevers were cut into different membranes. No imaging of the membranes was carried out using the FIB. Correct positioning of the sample was achieved using only the SEM. Alignment of the electron and ions beams was carried out on the supporting silicon wafer, far from the membrane.

Figure 5.2c,d shows images of two cantilevers cut into the same PS coated membrane. The cantilever in figure 5.2c was milled first and imaged using the SEM. The cantilever in figure 5.2d was then milled and imaged. The first cantilever milled is seen to deflect upwards and the second downwards. A similar downward deflection was observed for all subsequent cantilevers milled into the same membrane.

The silicon nitride (SiN) membranes obtained from SPI supplies are manufactured to have a low intrinsic stress. To check that the deflection observed in figure 5.2a,b,c was not due to stored stress in the SiN, similar cantilevers were milled into uncoated membranes. Examples of these are shown in figure 5.3. The initial cantilever milled is shown in figure 5.3a, while figure 5.3b shows a second cantilever cut into the same membrane. No deflection is observed in the initial cantilever, while a small down-

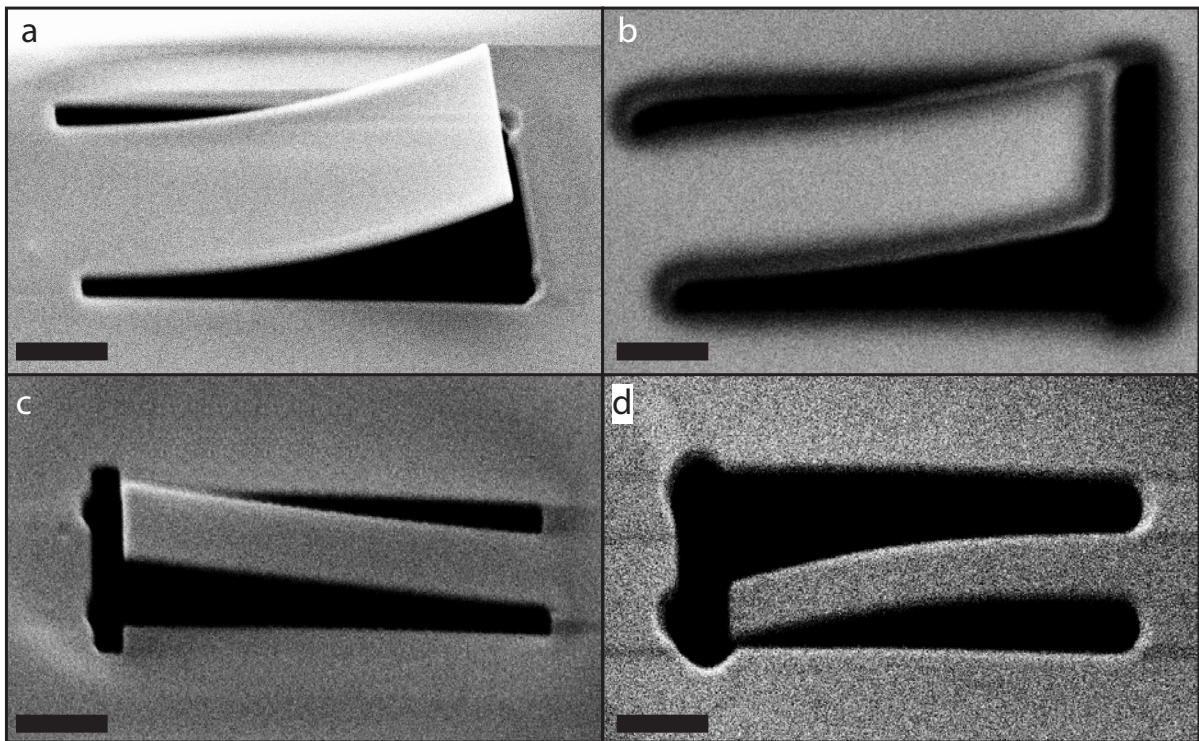


Figure 5.2: Micrographs showing cantilevers milled in PS coated SiN membranes. (a) Membrane 1, first mill. (b) Membrane 2, first mill. Membrane 3 (c) first mill, (d) second mill. Scale bar is 2 μm .

ward deflection is observed in the second.

These results suggest that the ion beam imparts some energy into the membrane and the polymer film during the milling process. While the films were not actively imaged using the ion beam, once milling has finished, a partial scan of the surface does occur as the beam is switched off. This is a property of the CrossBeam system and cannot be avoided.

To see whether this partial FIB imaging may cause the change in behaviour observed in figure 5.2c,d, two cantilevers were milled concurrently, the FIB beam was not switched off between the milling of each cantilever and no SEM images were taken. An example of the cantilevers milled using this method, for both a PS coated on an uncoated SiN membrane, can be seen in figure 5.4. For the PS coated SiN sample, both cantilevers were observed to deflect upwards with an equal radius of curvature. This suggests that the downwards deflection observed in figure 5.2d results

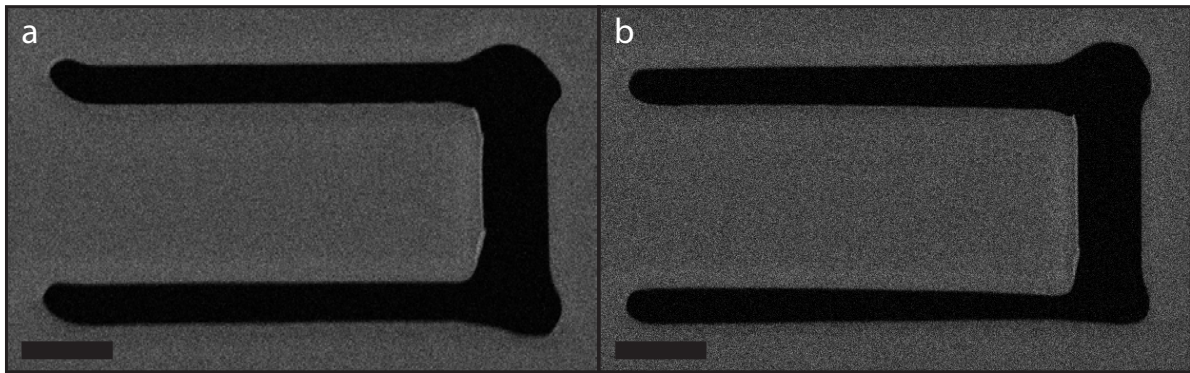


Figure 5.3: Micrographs showing cantilevers milled in an uncoated SiN membrane. Two cantilevers were milled one after the another. Imaging was carried out after each cantilever was milled. (a) First cantilever. (b) Second cantilever. Scale bar is 2 μm .

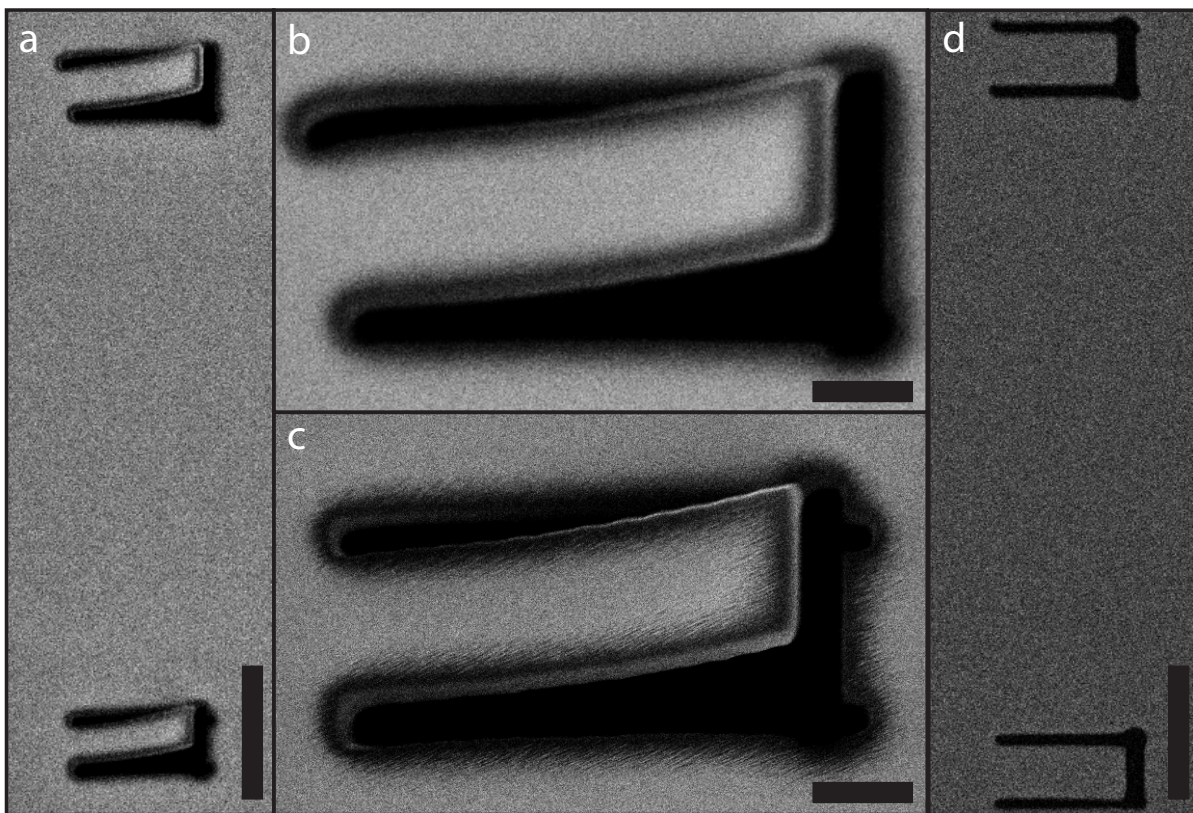


Figure 5.4: Micrographs showing cantilevers milled in PS coated SiN membrane. Two cantilevers were milled concurrently with no imaging between mills. (a) Two cantilevers $\sim 20 \mu\text{m}$ apart. (b,c) Enlargement of the cantilevers shown in (a). (d) Micrograph showing two cantilevers milled concurrently in an uncoated SiN membrane. (a,d) Scale bar is 10 μm . (b,c) Scale bar is 2 μm .

from partial imaging of the sample with the ion-beam.

All images shown here were imaged with the electron beam, after milling had com-

Figure	Sample	Cut	δ (μm)	L (μm)
1a	PS+SiN	First	3.06	9.53
1b	PS+SiN	First	2.79	9.27
1c	PS+SiN	First	1.28	9.37
1d	PS+SiN	Second	-2.18	8.72
2a	SiN	First	–	9.37
2b	SiN	Second	-0.5	9.71
3a	PS+SiN	First	2.79	9.27
3b	PS+SiN	Second	2.43	8.99

Table 5.1: Deflection and length of the different cantilevers shown in figures 5.2, 5.3 and 5.4.

pleted, at an angle of 54° . The deflection and length of the cantilever were measured using ImageJ software and converted into actual distances. These are shown in table 5.1. It should be noted that while the PS films in figure 5.2a,b and figure 5.4a were spun on to the membranes and used directly, the PS film in figure 5.2c,d was milled one month after the film was spun. This may account for the smaller deflection seen in the initial cantilever.

5.2.1 Cantilever bending

The stresses in the polymer film can be calculated from the deflection of the cantilever. The bending of cantilevers due to residual stresses in polymer coatings has been considered by Corcoran [133]. While only the final equation is required for analysis of the cantilevers milled here, a summary of the derivation and the assumptions made are included for completeness.

The method of Corcoran uses plate theory to describe the bending of the cantilevers due to the stresses in organic coatings. Plate theory rather than beam theory (as used by Stoney [125]) is used, since the coating exists in tension in all directions. The following assumptions are made about the system:

1. The curvature of the deflected cantilever due to the stress in the coating is assumed to be spherical. This is consistent with the small curvatures measured experimentally. However, due to one end of the cantilever being fixed, the as-

Physical phenomena of thin surface layers

sumption will introduce a small systematic error.

2. The PS film adheres perfectly to the membrane. No dewetting of the PS from the SiN was observed and the film was not seen to delaminate on milling of the cantilever.
3. The elastic limit is not exceeded in any part of the cantilever.
4. The mechanical properties of the coating and the substrate are isotropic in the plane of the cantilever. Anisotropy in the film may occur in the plane of the cantilever due to the spin coating procedure however, the cantilever occupies a very small area of the film minimising this possibility.
5. The stress is constant through out the thickness of the coating. Chow and Croll have shown that the stress is independent of thickness [127, 134] suggesting that either there is no variation in the stress over the thickness of the film, or that the stress distribution takes the same form for any film thickness.

For pure bending of a flat, thin plate, the plate will have a spherical curvature if the bending moments along the edges are equal i.e. $m_x = m_y = m$. The curvature is given by

$$\frac{1}{\rho} = \frac{m}{D(\nu_s)} \quad (5.1)$$

where ρ is the radius of curvature and ν is Poisson's ratio. The flexural rigidity

$$D = \frac{E_s t_s^3}{12(1 - \nu_s^2)} \quad (5.2)$$

is the force required to bend a rigid structure to a unit curvature, where E is Young's modulus and t is the thickness of the plate. The subscript s refers to the SiN plate.

For a plate fixed at one end the radius of curvature of the bent plate is given by $\rho = L^2/2\delta$, where L is the length of the cantilever and δ is the deflection. Substituting

these into equation 5.1 gives

$$\delta = \frac{6mL^2(1-\nu_s)}{E_s t_s^3} \quad (5.3)$$

The deflection due to an applied polymer coating is considered to result from bending moments applied to the end of the plate, which arise from stresses in the film. In a bent equilibrium position, the coating is in a state of stress σ_{eq} , which exerts an average force F through the thickness t_f of the film. The bending moment per unit area is given by

$$m = \frac{M}{w} = \frac{Fw(t_f + t_s)}{2w} = \frac{\sigma_{eq} t_f (t_f + t_s)}{2} \quad (5.4)$$

where w is the width of the plate and M is the total moment applied. Combining equation 5.3 and equation 5.4 gives the stress in the coating

$$\sigma_{eq} = \frac{\delta E_s t_s^3}{3t_f L^2 (t_f + t_s) (1 - \nu_s)} \quad (5.5)$$

The above equation gives the equilibrium stress of the system. If the coating was instead applied to a rigid substrate, a greater stress would be found. When on a flexible plate the coating compresses, bending the plate. This means that the coating is shorter than it would be if it were on a rigid plate. This introduces a strain difference such that

$$\sigma_{tot} = \sigma_{eq} + \frac{\varepsilon E_f}{1 - \nu_f} \quad (5.6)$$

where $\varepsilon = (t_f + t_s)/2r$ is the strain difference. The total stress in the film is then found by combining equations 5.5, 5.6 giving

$$\sigma_{tot} = \frac{E_s t_s^3}{6t_f \rho (t_s + t_f) (1 - \nu_s)} + \frac{E_f (t_s + t_f)}{2\rho (1 - \nu_f)} \quad (5.7)$$

The subscripts s and f refer to the SiN membrane and the PS film respectively.

Young's modulus of the membrane and PS are taken to be 260 GPa [135] and 3.2 GPa [86] and poisson's ratio to be 0.25 [136] and 0.34 [86] respectively. Using equation 5.7,

Physical phenomena of thin surface layers

the stress in the as-spun PS film is found to be 211 ± 10 MPa. For the PS films aged at room temperature for one month the stress is calculated to be 120 ± 6 MPa. This is in agreement with dewetting experiments, where the residual stresses in the as-cast films are seen to decrease as the films are aged [106].

The value calculated for the stress in the as spun films is much higher than that calculated by other groups. Chung *et al.* monitored the onset of strain-induced wrinkling instabilities in PS $M_w = 654 \text{ kg mol}^{-1}$ films with thicknesses of 100 – 400 nm and found the residual stress to be ~ 30 MPa [137]. Croll carried out cantilever bending measurements using Dow styron 685 blade coated onto steel rules [128]. The molecular weight of this PS is $\sim 358 \text{ kg mol}^{-1}$ [138]. The stress was found to be 14.3 MPa for films of up to 18 μm . Neither group saw a change in the measured stress over this thickness range.

In chapter 4 it was shown that residual stresses, as measured using the onset of electrohydrodynamic instabilities, increase with increasing M_w of the PS. This is also seen in the values for the residual stress found in the literature. The PS used for these experiments had a $M_w = 4000 \text{ kg mol}^{-1}$, over six times greater than that used by Chung *et al.* This would account for the increased residual stress measured.

Partial imaging of the substrate with the ion beam was found to have an effect on the deflection of the cantilever beams, for both the uncoated SiN and the PS coated membrane (see figure 5.2 and figure 5.3). This effect was easily removed by milling multiple cantilevers concurrently (figure 5.4). The effect of imaging with the electron beam was not however investigated and while kept to a minimum cannot be avoided due to the need to align the microscope and observe the cantilevers. Mathrad *et al.* have shown that high energy electron irradiation of PS, with doses of up to 8 MeV, does not change the overall structure of PS films [139]. This indicates that PS is resistant to electron-beam irradiation up to this dose and that the structure should not be changed by the relatively low beam energies of 7 keV used here.

5.3 Conclusions

The internal stresses stored in spin-cast PS films were measured using a cantilever deflection technique. Cantilevers were cut into PS coated SiN membranes using a focused ion beam. On completion of milling the cantilevers were observed to bend upwards in the as-spun films. The stress in the PS film was found to be 211 MPa. Subsequent cantilevers milled in the same membrane were observed to have a downwards deflection. This is most likely due to partial imaging with the focused-ion beam on completion of the milling and was not observed in cantilevers milled concurrently.

The experiments conducted here show that focused ion beam milling of cantilevers is a promising technique for studying the stored stresses of polymer films. The study carried out here was a preliminary investigation to check the feasibility of this method. The dependency of the stresses on the molecular weight of the polymer or the thickness of the film was not investigated. A study of the stresses stored in PS $M_w = 655 \text{ kg mol}^{-1}$ would allow a comparison of the residual stresses found using this technique to literature values and eliminate possible influences of the milling process and electron-beam imaging on the observed bending of the cantilever. A more accurate determination of the effect of the ion and electron beams on the polymer film could also be investigated by flipping the PS/SiN bilayer upside down and imaging/milling it from the back. If either beam is altering the stresses in the polymer film then a smaller deflection should be observed for a cantilever milled in this configuration. This technique could also be used to measure the stresses in much thinner films than those that have been previously been studied.

In agreement with literature, the stresses in the polymer film were observed to decrease for films aged at room temperature. Since the films are aged at $T < T_g$ full equilibration of the films did not occur. As shown in chapter 4 equilibration through thermal annealing for high molecular weight polymers is not achievable on experimentally accessible timescales. Experiments on vapour annealed films, would allow

Physical phenomena of thin surface layers

cantilevers to be milled into fully equilibrated films. It is expected that a much smaller deflection in these films will be seen due to full relaxation and entanglement of the polymer chains.

A further application of focused ion beam milling would be to locally map out the stresses in spin-cast films, by spin coating of the polymer film onto a multi-frame array of membrane windows. By milling cantilevers into the different windows the stresses could be mapped out over centimetre areas.

PALLADIUM DOPED POLYMER PRECURSORS FOR MAGNETIC CERAMICS

Organometallic polymers containing transition metals in the backbone have attracted considerable attention [140–143] since the discovery of ferrocene nearly sixty years ago [144]. These materials have desirable properties [145] and applications as catalysts [146], sensors [147] and ceramic precursors [142]. Their unique processing characteristics allow for the possible fabrication of complex and nanostructured shapes [148] with a variety of magnetic properties [8].

One organometallic system which has received a large amount of interest over recent years is the metallocene-based polyferrocenylsilane (PFS) [149, 150]. PFS is an iron and silicon containing polymer, which when pyrolysed yields magnetisable ceramics due to the presence of clusters containing iron [151]. The size and type of these clusters can be controlled by adjusting the pyrolysis conditions. At lower pyrolysis temperatures (around 600 °C) the formation of ceramics containing small superparamagnetic iron nanoclusters in an amorphous ferromagnetic carbon/silicon carbide matrix [152] is observed. Increasing the temperature of pyrolysis to around 1000 °C, leads to an increase in the cluster size and the generation of ferromagnetic

ceramics containing α -Fe crystallites.

Cross-linking of precursors allows for higher ceramic yields, magnetic properties which are tunable and the ability to produce molded ceramics due to high shape retention [8,153,154]. For example, MacLachlan *et al.* [8] have shown that a cross-linked network of spirocyclic [1]silaferrocenophane can be used to form ceramics whose properties at room temperature can be tuned between superparamagnetic and ferromagnetic states, by controlling the pyrolysis conditions. These polymers can be shaped on the macroscopic scale or patterned on the micron-scale prior to pyrolysis, with the ceramic products retaining the patterned shape with high-fidelity. Higher ceramatisation yields and increased iron content are also seen from hyperbranched polyferrocenylsilanes [155]. These produce mesoporous ferromagnetic materials, with a negligible hysteresis loss when pyrolysed at high temperatures under argon, due to the formation of iron silicides. These materials have potential applications for data storage and electromagnetic shielding [156]. PFS has also been used as a precursor to form microspheres with low polydispersity [154], allowing for the synthesis of microspheres with tailorable redox, semiconductive and magnetic properties [157].

Another interesting application of metal containing polymers is their use as precursors for the synthesis of bimetallic nanoparticles. This has been demonstrated for iron-platinum (FePt) nanoparticles [158] formed from the pyrolysis of bimetallic metallopolyne precursors. Pyrolysis of PFS precursors with pendant cobalt clusters and polycarbosilanes with pendant nickel clusters have been shown to yield cobalt-iron [159] and nickel or nickel silicide nanoparticles respectively [160].

Variation in the pyrolysis conditions results in changes to the nanoparticle size, distribution and composition. Thin films containing CoFe nanoparticles were shown to exhibit superparamagnetic behaviour, with ferromagnetic behaviour being observed for pyrolysis at higher temperatures. This is attributed to a stabilisation of the nanoparticle magnetisation on the time scale of the hysteresis measurement due to the increased size of the nanoparticles which form at higher temperatures. Pyroly-

sis of the nickel containing polycarbosilanes yielded ceramics embedded with nickel particles or nickel silicides depending on the pyrolysis conditions, with both superparamagnetic and ferromagnetic behaviour being observed.

While this shows that bimetallic precursors can be used to synthesis nanoparticles with desirable properties, these precursors can be hard to synthesise as they require the controlled incorporation of different metals into the macromolecular architecture and ancillary ligands which do not interfere in the nanoparticle formation. This chapter focusses on the formation of ceramic films containing FePd nanoparticles from polyferrocenylethylmethylsilane (PFEMS) using the physicochemical methods of evaporation, reduction and thermal breakdown. The incorporation of Pd into polymer precursors is desirable due to the unique properties of Pd and the magnetic properties of FePd alloys [161]. These are of paramount technological relevance due to the large saturation magnetisation and magneto-crystalline anisotropy (hard magnetic behaviour), persistent even in FePd nanoparticles larger than 8 nm [162, 163], rendering them suitable for ultra-high density magnetic storage [164].

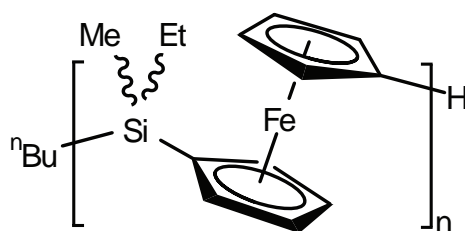


Figure 6.1: Molecular structure of PFEMS.

6.1 Materials and methods

The PFEMS homopolymer was prepared by living anionic ring opening polymerisation of ethylmethylsila[1]ferrocenophane as described in [165]. Figure 6.1 shows the molecular structure of the polymer. The molecular weight and polydispersity index of the material used in this study were 22.5 kg mol^{-1} and 1.01 respectively, as determined by Gel Permeation Chromatography (GPC). GPC was carried out on a Viscotek GPC-max chromatograph equipped with a triple detector array. A flow rate of 1.0 ml min^{-1} was used with THF as the eluent¹. Palladium(II)-acetylacetonate ($\text{Pd}(\text{acac})_2$) 99% purity was obtained from Sigma-Aldrich and used without modification.

The addition of Pd to the PFEMS was carried out using two different methods; as nanoparticles through sublimation of palladium-acetylacetonate ($\text{Pd}(\text{acac})_2$) or through direct mixing of the $\text{Pd}(\text{acac})_2$ into the PFEMS prior to pyrolysis of the films. The pyrolysis scheme is shown in table 6.1. Three sets of films were made: pure PFEMS films (precursor 1), PFEMS films containing Pd nanoparticles (precursor 2) and PFEMS films containing $\text{Pd}(\text{acac})_2$ (precursor 3). Pure PFEMS films were formed by drop-coating PFEMS-toluene solutions onto naturally oxidised Si(100) wafer substrates obtained from Silicon Materials. The dry films were subsequently annealed in a vacuum oven at 60°C for 24 hrs. For PFEMS films containing $\text{Pd}(\text{acac})_2$, the $\text{Pd}(\text{acac})_2$ was mixed into the PFEMS-toluene solutions prior to drop coating with a w/w ratio of 1:4 $\text{Pd}(\text{acac})_2$:PFEMS. The Pd nanoparticle deposition was carried out using the

¹Polymerisation of PFEMS and GPC measurements were carried out by J. Gwyther at the University of Bristol.

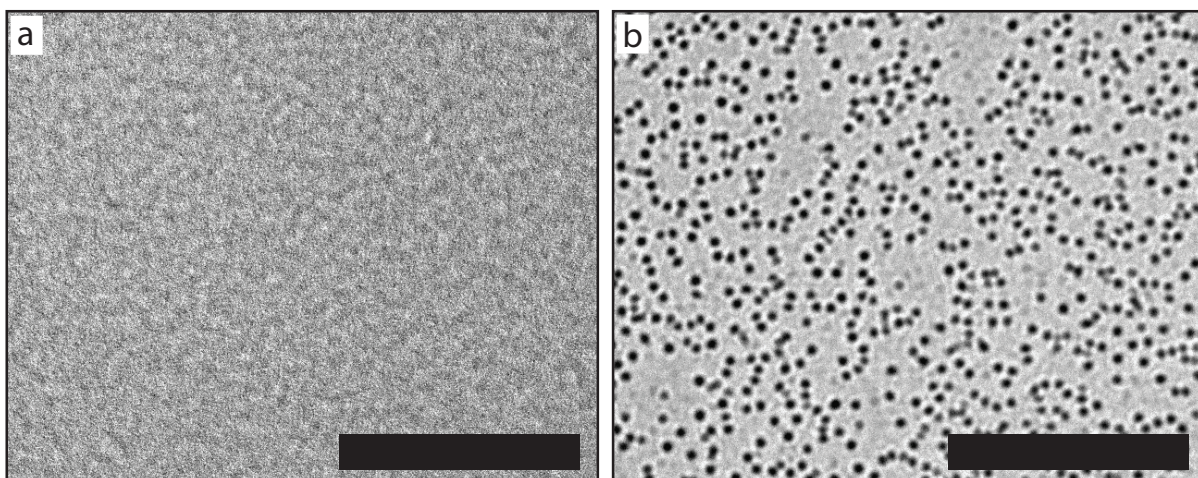


Figure 6.2: TEM micrographs of a PFEMS film (a) before and (b) after Pd nanoparticle deposition. Scale bar is 200 nm.

method described in [166]. The PFEMS films were placed in a crystallisation dish, with ~ 13 mg of $\text{Pd}(\text{acac})_2$. The crystallisation dish was filled with nitrogen, sealed and placed in a box oven, which was pre-heated at 170°C , for 1 hr. The $\text{Pd}(\text{acac})_2$ sublimes and Pd nanoparticles form through the thermal decomposition of $\text{Pd}(\text{acac})_2$ to metallic Pd. TEM images before and after this exposure are shown in figure 6.2.

Pyrolysis was initially carried out in a tube furnace under nitrogen at 600°C and 1000°C for 3 hrs with a heating rate of $15^\circ\text{C min}^{-1}$. The results from these experiments however, indicated that the nitrogen atmosphere had some oxygen impurities. As a result pyrolysis was also carried out under argon at 1000°C . Substrates were weighed

Ceramic Name	Precursor	Pyrolysis Temperature ($^\circ\text{C}$)	Pyrolysis Atmosphere
1aN	1	600	N_2
1bN	1	1000	N_2
1bA	1	1000	Ar
2aN	2	600	N_2
2bN	2	1000	N_2
2bA	2	1000	Ar
3aN	3	600	N_2
3bN	3	1000	N_2
3bA	3	1000	Ar

Table 6.1: Pyrolysis scheme for the different ceramics.

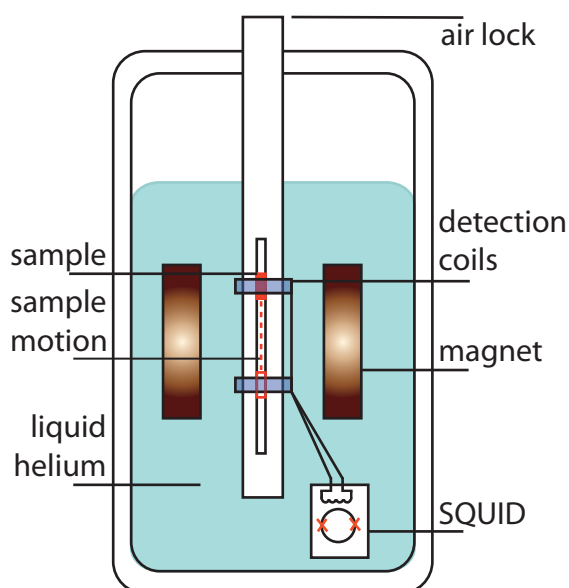


Figure 6.3: Schematic diagram of a SQUID magnetometer showing the basic setup (image adapted from [167]).

before and after film deposition and samples were weighed before and after pyrolysis.

SQUIDS

The magnetic properties of the films and ceramics were measured at room temperature and 5 K using a Quantum Design MPMS Superconducting Quantum Interference Device (SQUID) magnetometer.

Superconducting quantum interference devices (SQUID) are highly sensitive detectors of magnetic flux, which can measure weak magnetic fields as low as 10^{-17} T. They are able to measure any quantity that can be converted to a flux, such as magnetic field, current, voltage, displacement and magnetic susceptibility, making them very versatile. As a result, the applications of SQUIDS are wide ranging, from the detection of tiny magnetic fields produced by the brain [168], to the detection of gravity waves [169]. Here a SQUID was used to analyse the magnetic properties of the precursor and ceramic films.

The basic phenomena governing the operation of SQUID devices are flux quantisation in superconducting loops and the Josephson effect. A detailed description of

the theory behind SQUIDs can be found in [170]. The system contains a homogenous superconducting magnet as shown in figure 6.3, to create a uniform field over the entire region in which the sample is measured. A dc-field is applied across the sample to induce a permanent magnetic moment. This field is kept fixed, while the sample is moved into a set of superconducting detection coils. As the sample passes through the coil, the magnetic moment of the sample induces a current in the detection coils. The current passes through an inductance loop generating a magnetic flux which is fed into a SQUID. The output voltage is dependent on the position of the sample and the applied field. By varying the applied field, the hysteresis behaviour of the sample can be measured.

EDX Analysis

Energy dispersive X-ray (EDX) elemental analysis was performed to look at the atomic composition of the ceramics, using an FEI Philips XL30 sFEG with an EDX detector. Measurements were carried out at 20 kV, 15 kV and 12 kV at a working distance of 5 mm. Three different areas were measured for each sample and averaged to take into account composition variations across the films.

During EDX analysis, the sample is placed inside a scanning electron microscope and bombarded with a beam of electrons². These electrons collide with electrons within the sample, knocking them out of their orbits. The empty positions are then filled with electrons from outer energy shells. The energy difference between these two shells is emitted as an X-ray. The energy of the X-ray is dependent on the element being bombarded and the difference in energy between the shells that the electron has moved from and to. The X-rays are detected using an energy dispersive spectrometer. The energy and number of X-rays detected can be used to find the atomic composition and the weight percent of each element in the sample.

²EDX analysis is an integrated function of a scanning electron microscope. It cannot be operated independently.

X-ray diffraction

The bulk composition and crystalline structure of the precursors and ceramics were investigated using X-ray diffraction (XRD). This technique is based on the constructive interference of monochromatic X-rays with a crystalline sample and is widely used for the identification of unknown crystalline materials. An X-ray diffractometer consists of three different elements: an X-ray tube, a sample holder and an X-ray detector. The X-rays are generated by a cathode ray tube, filtered to produce monochromatic radiation, collimated to increase intensity and directed towards the sample. Interaction of the incident radiation with the sample produces constructive interference when the Bragg condition is satisfied i.e. $n\lambda = 2d \sin \theta$, where λ is the wavelength of the radiation and d is the lattice spacing of the crystalline sample. When the crystals are randomly orientated, scanning over all 2θ angles allows for all possible diffraction directions of the lattice to be obtained. For a detailed discussion of crystallography and X-ray diffraction see [171].

X-ray diffractograms were obtained using Philips PW1820 and PW3020 X-ray generators with a $\text{CuK}\alpha$ ($\lambda = 1.54178 \text{ \AA}$) radiation source. The samples were mounted on an amorphous silicon wafer. The angle was varied from 2° to 75° in steps of 0.05° with 2.5 s per step. The peaks were identified by comparison with data files from the PCPDFWIN crystallographic database.

Microscopy

Image analysis was carried out using a Leo variable pressure Scanning Electron Microscope (SEM) and a Philips Technai 20 Transmission Electron Microscope (TEM). The samples were formed directly on the TEM grids, by dip coating them into the PFEMS-toluene solutions. The use of TEM for imaging is discussed in chapter 7. For imaging of the PFEMS-Pd films, no staining was carried out.

In scanning electron microscopy (SEM) an electron beam is focussed into a small spot size and scanned over the surface of a sample, releasing secondary electrons.

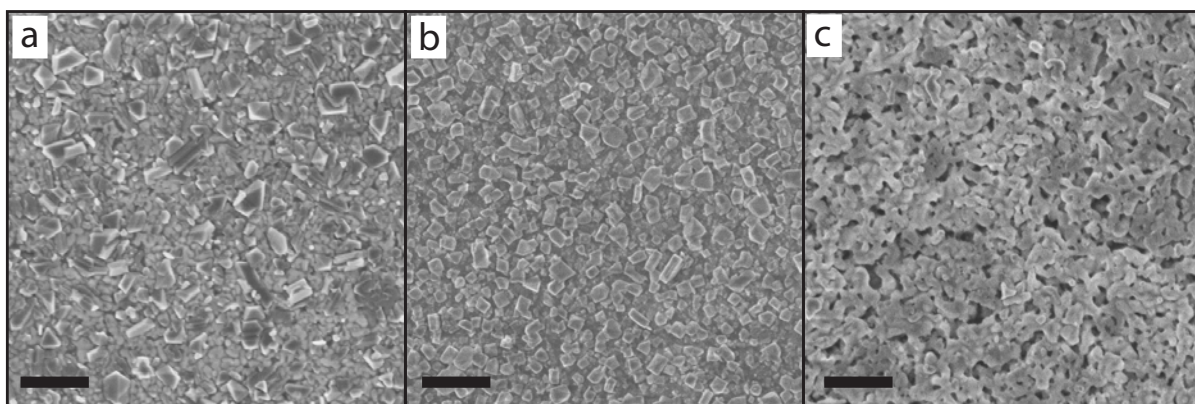


Figure 6.4: SEM micrographs of ceramics (a) 1bA, (b) 2bA and (c) 3bA. Scale bar is 1 μm .

These are recorded using a secondary electron detector. Only secondary electrons close to the surface ($< 10\text{ nm}$) can exit the sample and be detected, due to the relatively low energy of these electrons. By correlating the number of electrons with the position of the scan a topographical image of the sample can be generated, where the intensity of the pixel corresponds to the number of electrons detected at that position.

6.2 Results

Pyrolysis of the PFEMS films without the addition of Pd under nitrogen, 1aN and 1bN, resulted in a red coloured ceramic. Figure 6.4 shows examples of the film morphology for ceramics pyrolysed under argon. Similar morphologies were seen for all ceramics.

Energy Dispersive X-ray (EDX) analysis was used to investigate the chemical composition of the polymer and the ceramics. Four elements were detected by EDX in the PFEMS precursor film: carbon (C), silicon (Si), iron (Fe) and oxygen (O). For ceramics 1aN and 1bN three elements were found: O, Si and Fe. Si and Fe come from the polymer precursor. Oxygen has been found in the ceramics, even though pyrolysis was conducted in a sealed quartz tube under nitrogen. No C was detected in samples pyrolysed under nitrogen, but was seen for samples pyrolysed under argon (table 6.2).

Physical phenomena of thin surface layers

Element (wt.%)	1bA	2bA	3bA
C	28.61	23.70	22.26(13.83)[8.24]
O	39.46	34.47	34.64(34.83)[33.63]
Si	11.96	13.91	9.52(11.44)[13.00]
Fe	19.97	18.88	21.22(27.84)[33.86]
Pd	–	9.004	12.36(12.06)[11.18]

Table 6.2: Composition of ceramics, pyrolysed under argon, estimated using EDX analysis. Values indicate the weight percentage of each element, measured with a beam energy of 20 keV (15keV) and [12keV].

The literature shows that oxygen is often found in ceramics prepared using the precursor method [155]. Oxygenic compounds may stem from moisture absorbed by the polymers prior to pyrolysis and/or from post-oxidation of the samples during handling and storage. They may also arise from impurities in the nitrogen used to purge the furnace prior to and during pyrolysis. Table 6.2 shows the composition of films pyrolysed under argon in terms of the weight percent of each element at a beam energy of 20 keV.

The EDX data for ceramics pyrolysed under argon are shown in table 6.2. Example traces for ceramics 1aN and 2aN are shown in figure 6.5. The results are representative of all the ceramics. Analysis of ceramics pyrolysed from precursors 2 and 3 indicates the presence of Pd (figure 6.5b). For samples 2aN, 2bN and 2bA, Pd nanoparticles were incorporated into the films through sublimation of Pd(acac)₂. TEM images before and after this exposure are presented in figure 6.2 and show the addition of Pd nanoparticles with an average diameter of 6 nm.

When probing the samples with electron beams of different energies, the probing depth of the sample is altered, with lower beam energies having a smaller penetration depth [172]. For films pyrolysed under argon, a dramatic decrease in the carbon content is seen as the beam energy is decreased. Data for sample 3bA are shown in table 6.2. The data suggest that there is less carbon at the surface than in the bulk, which may be a result of oxidation of the surface, perhaps due to the adsorption of oxygen on the film prior to loading. The Pd content of all Pd containing samples does

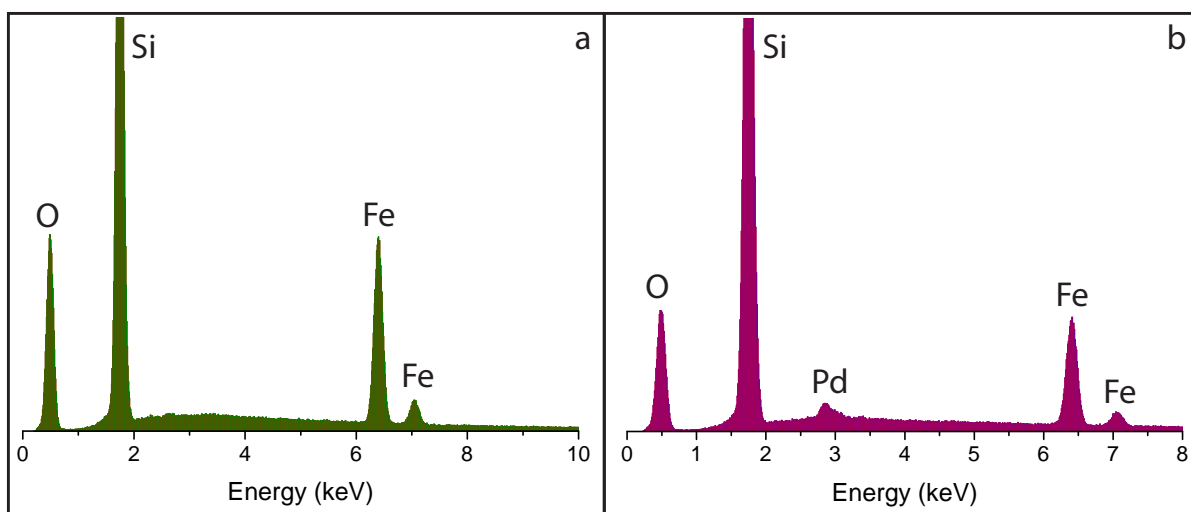


Figure 6.5: EDX analysis traces for samples (a) 1aN and (b) 2aN.

not change with probe depth, while the Fe content increases with decreasing probe depth, suggesting that Fe is more abundant at the surface of the films. Similar behaviour was observed for all Pd containing ceramics and is consistent with previous studies [173]

X-Ray Diffraction (XRD) analysis was carried out to investigate the bulk composition and crystal structure of the ceramic products. The XRD patterns are shown in figure 6.6. All samples had a strong reflection peak at 69.13° arising from the Si wafer used as the substrate. This peak was used to align the individual scans and to determine the accurate position of the other peaks; it is not shown in figure 6.6 for clarity. XRD characterisation of samples 1bA, 2bA and 3bA was carried out on a different generator to that used for the other samples. Harmonic peaks are observed from the Si(400) peak when using this generator due to the absence of a filter. These three spectra are plotted together along with the spectra of the silicon substrate for clarity (figure 6.6d). The PFEMS polymer precursor 1 is amorphous, exhibiting no sharp reflection peaks, but a diffuse halo in the 2θ angle region centred around 13° between 10° to 18° . The diffuse halo is also seen for the Pd containing precursor films 2 and 3 along with additional peaks, which come from the Pd. Comparison of precursor films 1 and 3, show that the $\text{Pd}(\text{acac})_2$ has strong peaks at $2\theta = 11.85^\circ$ $d = 7.47 \text{ \AA}$,

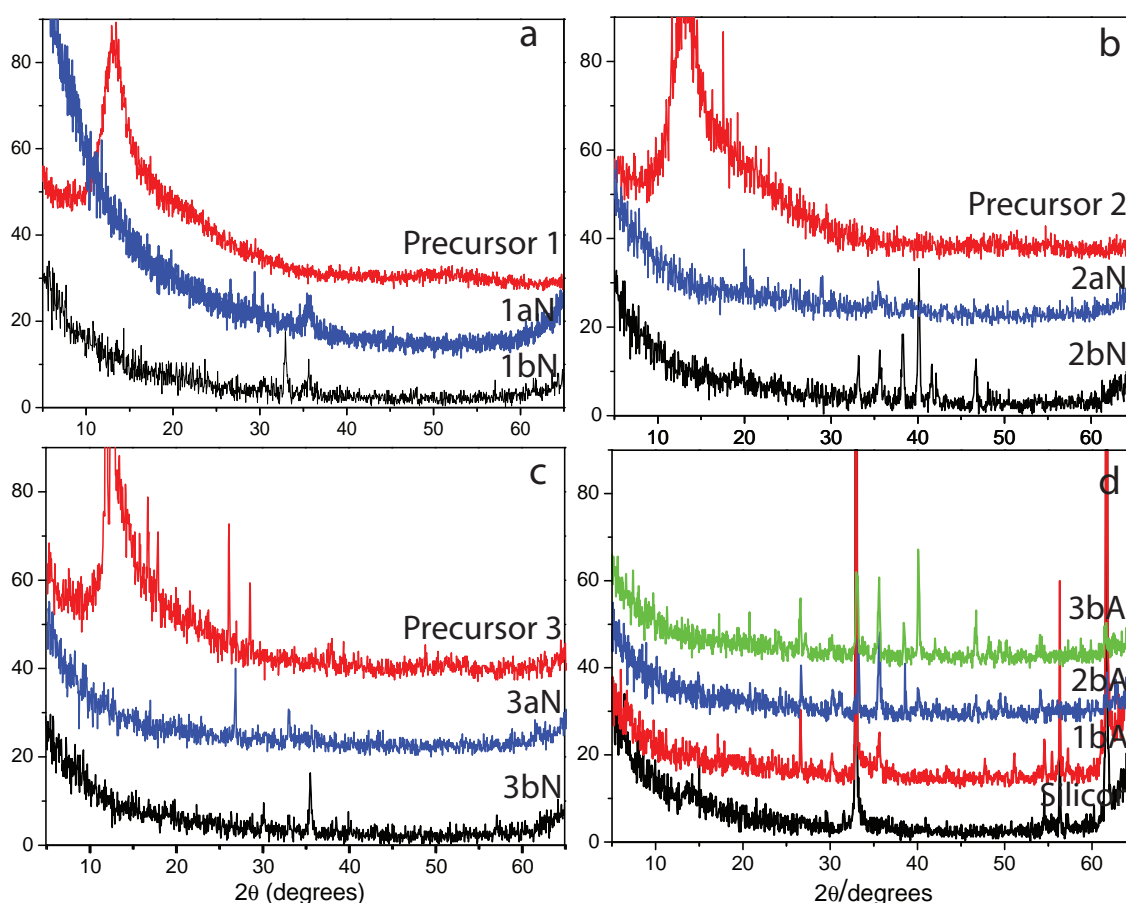


Figure 6.6: XRD data (a) PFEMS precursor and ceramic films. (b) PFEMS precursor and ceramic films containing Pd nanoparticles. (c) PFEMS precursor and ceramic films containing Pd(acac)₂. (d) Ceramic films pyrolysed under argon.

12.66° (6.99 Å), 16.39° (5.41 Å), 17.90° (4.96 Å), 26.08° (3.42 Å) and 28.45° (3.14 Å). These correspond very closely to those found for powdered Pd(acac)₂ at by Cominos *et al.* [174].

The ceramic products of 1, 2 and 3 show diffraction patterns with numerous Bragg reflections, indicating that the ceramics contain a number of crystalline species. The Scherrer equation [175] can be used to estimate the size of the crystals present in the samples. The equation is given by

$$\tau = \frac{K\lambda}{\beta \cos \theta} \quad (6.1)$$

where K is the shape factor, λ is the X-ray wavelength, β is the line broadening of the

peak at full width half maximum and θ is the Bragg angle. Using equation 6.1, the size of the crystals is estimated to be between 18–45 nm. This is smaller than the size of the crystals seen in the SEM images (figure 6.4), which are on the order of 100 – 200 nm in size, suggesting that the ceramic crystalline structures, as seen by SEM, are not pure in composition. Instead clusters of different species coexist.

Data files from the crystallographic database were used to identify the peaks observed in the XRD spectra (figure 6.6). The results are summarised in table 6.3. All the ceramics show reflection peaks at $2\theta \approx 35.6^\circ$ ($d = 2.52 \text{ \AA}$) corresponding to ferrimagnetic Fe_3O_4 and $\gamma\text{-Fe}_2\text{O}_3$. Sample 1bA exhibits an additional higher order reflection peak of $\gamma\text{-Fe}_2\text{O}_3$ at 57.24° (1.61 \AA). This was not detected for the other ceramic samples, probably due to imperfect packing of the crystals. The reflection peaks associated with $\alpha\text{-Fe}_2\text{O}_3$ at 33.15° (2.70 \AA) and 35.61° (2.52 \AA) are seen for all ceramics apart from 1aN and 2aN. The second order reflection observed in the XRD spectra from $\alpha\text{-Fe}_2\text{O}_3$ suggests that Fe_2O_3 exists mainly in the α form. The peaks associated with reflections of $\alpha\text{-Fe}$ metal are only seen in the spectra for 1bA, where a very weak peak is observed. Thus, the majority of iron species exist in oxide form. The stronger peaks are observed for the ceramics pyrolysed at 1000°C under argon (1bA, 2bA, 3bA).

For ceramics pyrolysed under nitrogen, carbon is only observed in the spectra of 3aN. It is present in all samples pyrolysed under argon. This strongly suggests impurities in the nitrogen atmosphere used for pyrolysis lead to oxidative degradation. The reflection peaks of SiO_2 and SiC are weak and broad. This is most likely due to the majority of silicon and carbon species existing in the amorphous state.

Pd exists as pure Pd (3aN), PdSi (2aN) and Pd_2Si . The peaks of Pd_2Si are observed at 38.26° (2.35 \AA) for all Pd containing samples apart from 2aN. Ceramics 2bN and 3bA also show higher order reflections peaks for Pd_2Si at 41.53° (2.17 \AA), 42.22° (2.14 \AA) and 48.76° (1.87 \AA). The peaks are most prominent in ceramics pyrolysed under argon.

Pd and FePd alloys exhibit similar reflection peaks. Bryden *et al.* [176] have shown that pure Pd exhibits a peak at $\sim 40^\circ$. They synthesised FePd alloys and showed that

Crystal	1aN	1bN	1bA	2aN	2bN	2bA	3aN	3bN	3bA	File
α -Fe			43.4(2.05)							31-0619
Fe ₃ O ₄	35.62(2.52)	35.53(2.53)	35.65(2.52)	35.51(2.53)	35.61(2.52)	35.62(2.52)	35.63(2.52)	35.63(2.52)	35.55(2.53)	19-0629
α -Fe ₂ O ₃		32.93(2.72)	33.08(2.71)		33.16(2.70)	33.08(2.71)	33.08(2.71)	33.08(2.71)	33.08(2.71)	33-0664
		35.53(2.53)	35.65(2.52)		35.61(2.52)	35.62(2.52)	35.63(2.52)	35.63(2.52)	35.55(2.53)	
γ -Fe ₂ O ₃						54.08(1.7)			54.13(1.69)	
	35.62(2.52)	35.53(2.53)	35.65(2.52)	35.51(2.53)	35.61(2.52)	35.62(2.52)	35.63(2.52)	35.63(2.52)	35.55(2.53)	39-1346
SiO ₂			57.24(1.61)							
	30.33(2.95)	30.49(2.93)	30.28(2.95)	29.03(3.08)				30.13(2.97)	30.08(2.71)	72-2310
	29.14(3.06)									72-1601
C			26.64(3.35)							
SiC						26.65(3.35)	26.83(3.32)		26.52(3.39)	75-2078
					35.61(2.52)	35.62(2.52)	35.63(2.52)	35.63(2.52)	35.55(2.53)	75-1541
Pd					38.25(2.35)	38.56(2.33)	38.60(2.33)	38.39(2.34)	38.46(2.34)	
								40.5(2.23)		7440-05-3
PdFe					40.16(2.25)	40.06(2.25)		40.01(2.25)		[176, 177]
PdSi					46.68(1.95)	46.74(1.94)			46.60(1.95)	
				29.03(3.08)						07-0127
Pd ₃ Si					38.25(2.35)	38.56(2.35)	38.60(2.33)	38.39(2.34)	38.46(2.34)	06-0559
					41.53(2.17)			42.31(2.14)	41.94(2.15)	
					42.22(2.14)				48.24(1.89)	
					48.76(1.87)					

Table 6.3: Nanocrystals in the ceramics as identified by XRD analysis

as the volume fraction of Fe in the alloys increases, secondary reflections at $\sim 46^\circ$ start to appear and grow stronger. A small shift in the position of FePd peaks relative to Pd peaks has also been reported [177]. Ceramic 3bN exhibits a small peak at 40.5° (2.23 Å), corresponding to a reflection peak of Pd, no higher order reflections are seen. Ceramics 2bA and 3bA have a reflection peak at 40.01° (2.25 Å), which is lower than that seen in 3bN and have higher order reflections at 46.6° (1.95 Å) suggesting that the reflections come from FePd. This peak increases in magnitude from sample 2bA to 3bA, which is indicative of an increase in iron content in the FePd alloys [176].

SQUID magnetometry was used to investigate the magnetic behaviour of the films in a magnetic field at room temperature. The ceramics films fabricated from polymer precursors with the addition of Pd nanoparticles and Pd(acac)₂ and pyrolysed at different temperatures and under different atmospheres displayed different magnetic properties. The magnetisation curves are shown in figure 6.7. The precursor films 1, 2 and 3 all displayed paramagnetic behaviour at room temperature. The PFEMS precursor film (precursor 1) had a susceptibility of $11.28 \pm 0.08 \times 10^{-6}$ emu/g³. The addition of Pd in nanoparticle form to the PFEMS increased the susceptibility four-fold. Films made from precursor 3, where the Pd(acac)₂ had been mixed directly with the polymer, had a susceptibility nearly ten times greater than that of precursor 1 (table 6.4).

The pyrolysed samples were all found to display ferromagnetic behaviour (figure 6.7). The saturation magnetisation M_s , remanent magnetisation M_r and coercivity H_c for the samples are given in table 6.4. Films pyrolysed from precursor 1 had the lowest coercivity. This increased as Pd was added first in nanoparticle form (samples pyrolysed from precursor 2) and then directly as Pd(acac)₂ (samples pyrolysed from precursor 3). The highest coercivity was seen for samples pyrolysed under argon. Increasing the pyrolysis temperature to 1000 °C resulted in an increase in the coercivity for all the ceramics. The coercivity of samples 1bN and 2bN are comparable, whilst sample 3bN had a coercivity four times greater. For samples pyrolysed under argon,

³Units of mass magnetisation: $1 \text{ emu/g} = 4\pi \times 10^{-7} \text{ Am}^2/\text{kg}$

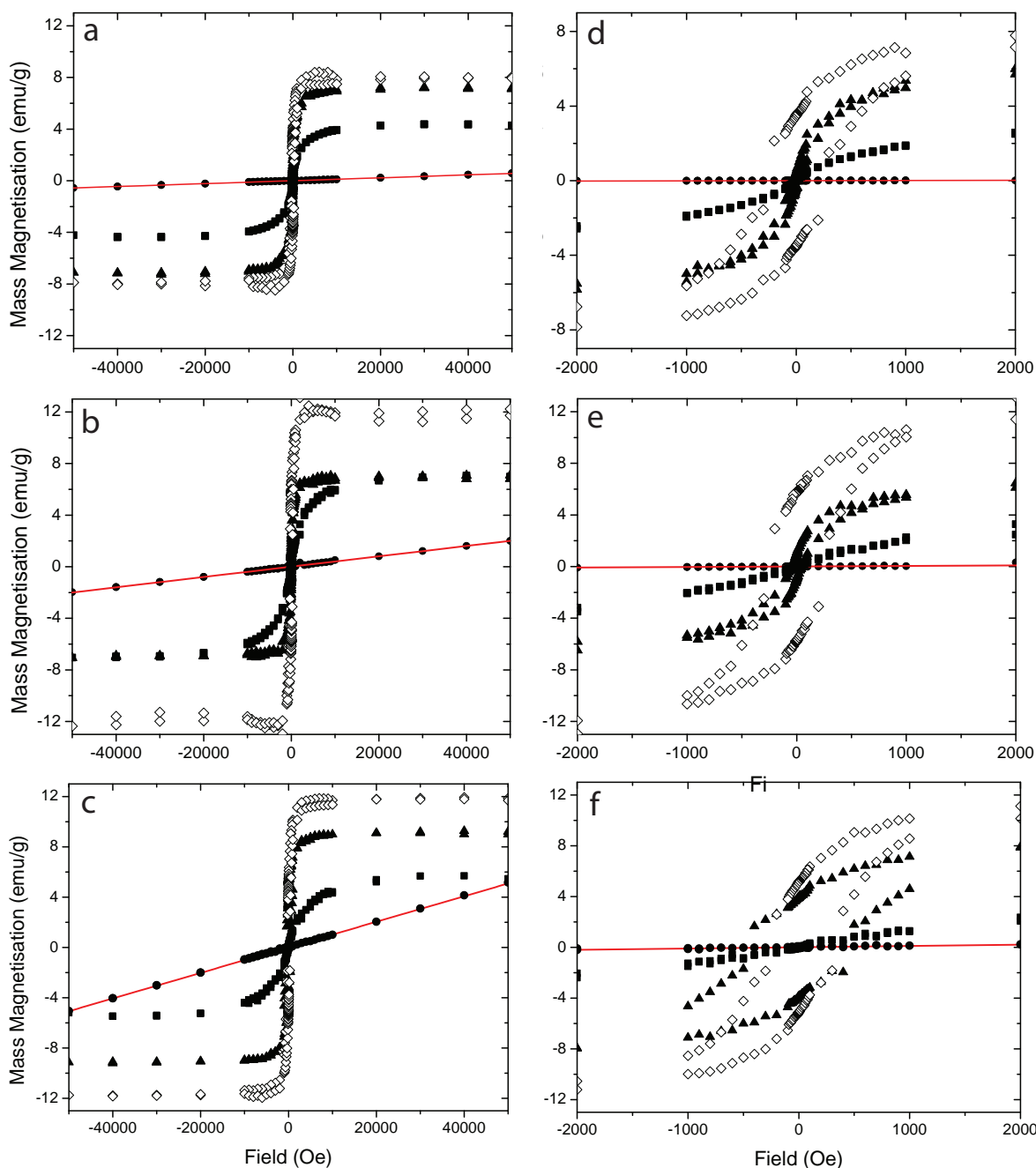


Figure 6.7: SQUID magnetisation curves at room temperature. (a) Precursor 1 and ceramics. (b) Precursor 2 and ceramics. (c) Precursor 3 and ceramics. (d), (e), (f) Magnification of (a), (b) and (c) respectively. (●) Precursor films. (■) Ceramics pyrolysed at 600°C under nitrogen, (▲) at 1000°C under nitrogen and (◇) at 1000°C under argon.

the coercivity of ceramics 1bA and 2bA was the same, with a small increase being observed for 3bA.

The remanent magnetisation measured for the ceramic films from the SQUID mag-

Sample	χ_ρ ($\times 10^{-6}$ emu/g)	M_s (emu/g)	M_r (emu/g)	H_c (Oe)
Precursor 1	11.28 ± 0.08	–	–	–
Precursor 2	40.04 ± 0.4	–	–	–
Precursor 3	101.6 ± 0.3	–	–	–
1aN	–	4.3 ± 0.1	0.031 ± 0.005	9.7 ± 0.5
2aN	–	6.96 ± 0.2	0.17 ± 0.01	64 ± 2
3aN	–	5.68 ± 0.2	0.20 ± 0.01	80 ± 5
1bN	–	7.16 ± 0.07	1.16 ± 0.01	77 ± 5
2bN	–	6.95 ± 0.3	1.26 ± 0.02	87 ± 2
3bN	–	9.12 ± 0.1	3.99 ± 0.02	338 ± 20
1bA	–	8.18 ± 0.2	3.48 ± 0.01	257 ± 5
2bA	–	12.2 ± 0.2	5.74 ± 0.01	256 ± 10
3bA	–	12.0 ± 0.2	5.30 ± 0.01	298 ± 10

Table 6.4: Magnetic properties of the precursors and ceramics. Susceptibility χ_ρ , saturation magnetisation M_s , remanent magnetisation M_r and coercivity H_c .

netisation curves at RT are shown in figure 6.8b. The remanence increases with increasing pyrolysis temperature and from films pyrolysed under N_2 to those pyrolysed under Ar (table 6.4). An increase in the remanence is seen on addition of Pd, with films pyrolysed from precursor 3 displaying the largest remanent magnetisation.

The remanent magnetisation for precursor 1 pyrolysed at 600°C is 0.031 ± 0.005 emu/g. This increased five-fold for Pd containing films. There was only a small difference between the Pd containing ceramics 2aN and 3aN formed using the two different Pd deposition methods. For films pyrolysed at 1000°C under N_2 the remanent magnetisation for 1bN and 2bN was comparable and strongly increased for 3bN. For ceramics pyrolysed under argon from precursor 1, the remanence was increased three fold as compared to those pyrolysed under N_2 . The remanence for films 2bA and 3bA also strongly increased.

The change in saturation magnetisation for the different ceramics is shown in figure 6.8c. A strong enhancement is seen for films containing Pd and from samples pyrolysed under argon. Ceramics 2bA and 3bA had saturation magnetisations of 12.2 ± 0.2 emu/g and 12.0 ± 0.2 emu/g respectively. This is nearly three times higher than the saturation magnetisation of ceramic 1aN of 4.3 ± 0.1 emu/g.

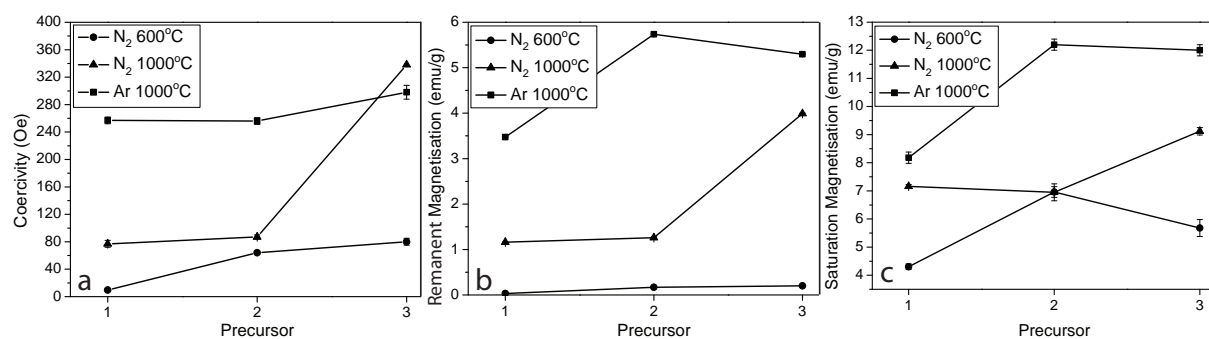


Figure 6.8: (a) Coercivity, (b) remanent magnetisation and (c) saturation magnetisation from the SQUID data for samples measured at room temperature.

6.3 Discussion

The pure PFEMS polymer and Pd doped polymer precursors are shown to be paramagnetic, with susceptibilities ranging from $11 - 102 \times 10^{-6} \text{ emu/g}$. This appears to be the first time that such data on the paramagnetic behaviour of PFEMS have been reported. This behaviour may arise from small amounts of oxidation of the Fe(II) centres to the Fe(III) state. Pd is a strong paramagnet with a susceptibility of $567.4 \times 10^{-6} \text{ emu/g}$ at room temperature. The increase in susceptibility of the precursor on addition of Pd, is most likely a result of the Pd acting as additional localised dipoles in the precursor. When pyrolysed under nitrogen, the pure PFEMS film forms a ceramic predominantly containing Fe oxides, in particular Fe_3O_4 or $\gamma\text{-Fe}_2\text{O}_3$. Both these oxides are ferrimagnetic materials. Only the main XRD peaks are seen here (figure 6.6), which are similar and therefore are hard to distinguish from one another. While the X-ray results do not show unambiguous stoichiometry, in some cases the EDX results can be used to deduce whether Fe_3O_4 or $\gamma\text{-Fe}_2\text{O}_3$ is most prevalent in the sample. Analysis of the data for samples 1aN and 2aN suggests that the peak at 35.62° most likely comes from Fe_3O_4 due to the amount of oxygen available to form Fe-oxides. However, the presence of $\gamma\text{-Fe}_2\text{O}_3$ cannot be ruled out and it is likely that a mixture of the two oxides is present in the ceramics.

The EDX analysis of the ceramics indicates that oxidation of the samples occurs either during or after pyrolysis. Analysis of sample 1bA shows that elemental iron

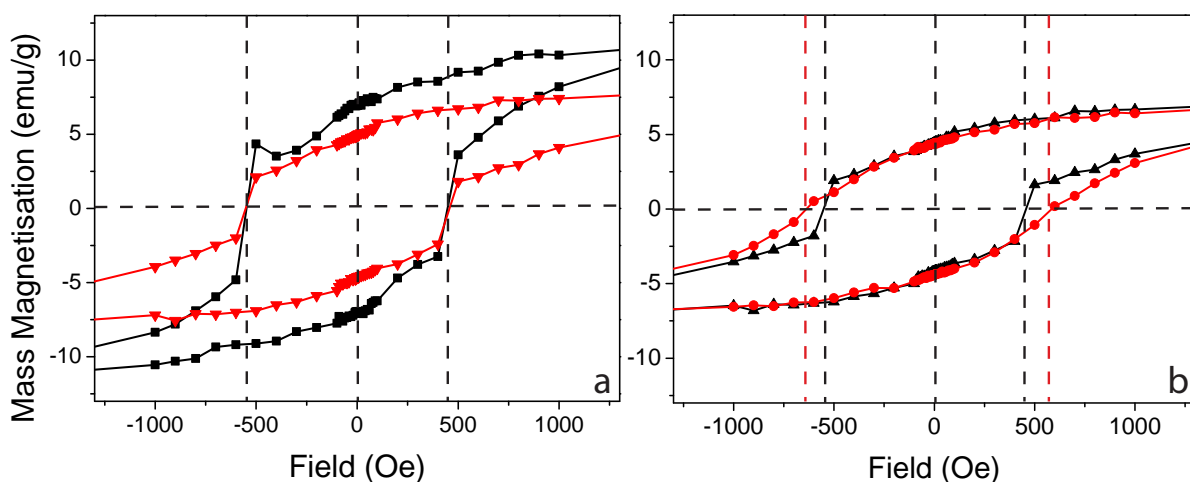


Figure 6.9: SQUID magnetisation curves at 5K. (a) Ceramics (▼) 1bA and (■) 2bA. (b) Ceramics (▲) 1bN and (●) 2bN. Dashed lines are a guide for the eye indicating the exchange bias.

formed during pyrolysis, suggesting that Fe forms initially and is then oxidised. The lack of carbon in the ceramics pyrolysed under nitrogen, suggests that for these samples, oxidation occurs both during and after pyrolysis, perhaps as a result of a contaminated atmosphere. For the ceramics pyrolysed under argon, the results indicate that oxidation of the Fe predominantly occurs post-pyrolysis. It should be noted that while the ceramics were allowed to cool to room temperature in the furnace under the nitrogen and argon atmospheres, they were not encapsulated. Once removed from the furnace the ceramics immediately came into contact with the air in the room.

The presence of the antiferromagnetic α -Fe₂O₃ (hematite) phase is confirmed by X-ray analysis in the majority of the samples and by magnetometry results. An exchange bias effect [178] is observed in pure PFEMS (1bN and 1bA) and in Pd nanoparticle doped ceramics (2bN and 2bA) pyrolysed at 1000 °C upon field cooling of the samples with a 1 T applied field to 5 K, as shown in figure 6.9. This is below the Morin transition temperature⁴ of 250 K [179]. The resulting exchange bias fields were -90 Oe⁵ for 1bA and 2bA, -60 Oe for 1bN and -40 Oe for 2bN. These results indicate the presence of core-shell clusters of ferromagnetic Fe (1bA) and ferrimagnetic Fe-oxides sur-

⁴A magnetic phase transition temperature in α -Fe₂O₃.

⁵Units of applied magnetic field: 1 Oe = 10³/4 π Am⁻¹

Physical phenomena of thin surface layers

rounded by a shell of α -Fe₂O₃, similar to those seen by Crisan *et al.* [180]. No such effect was observed for the ceramics arising from PFEMS and Pd(acac)₂ (3bN and 3bA). The exchange bias effect, which arises from the pinning of the ferromagnetic domain by the adjunct antiferromagnetic surface, results not only in a shift of the hysteresis known as the exchange bias field, but can also significantly alter the coercivity of the ferromagnet/ferrimagnet by acting as a pinning site of the domains upon reversal of the magnetisation. The absence of this effect in the ceramics pyrolysed from the Pd(acac)₂ precursor, indicates the absence of physical contact between hematite and the FePd clusters.

The magnetic properties of Fe-oxides are reported to be highly dependent on crystallinity, particle size, sample shape and purity [181]. The saturation and remanent magnetisation of nanocomposites of Fe₂O₃ and Fe₃O₄ have been widely studied [180–183] and were found to be significantly lower than the values reported for bulk material [184, 185]. The difference is attributed to the small particle size effect [186] and the inclusion of non-magnetic nanocomposites within the matrix of other materials, which reduces mass magnetisation. For γ -Fe₂O₃ nanoparticles of 20 nm with an amorphous SiO₂ coating, the saturation magnetisation, remanent magnetisation and coercivity were reported as 4 emu/g, 1.07 emu/g and 252.92 Oe respectively [181]. These correspond to the values seen here for ceramics pyrolysed from precursor 1, which did not contain any Pd and to those reported in the literature for ceramics pyrolysed from similar Fe-containing polymers [152, 153] confirming that the observed magnetic behaviour is indeed a result of the presence of Fe-oxides.

Two methods were used to dope the PFEMS films with Pd prior to pyrolysis: evaporation and reduction of Pd(acac)₂ to form nanoparticles and thermal degradation of Pd(acac)₂ mixed directly into the PFEMS. The results show that while both methods produce Pd-containing ceramics with enhanced magnetic properties, as compared to the ceramics formed from pure PFEMS, direct mixing of the Pd(acac)₂ into the precursor was the most successful method. Ceramics pyrolysed at a temperature of

1000 °C showed the greatest increase in magnetic properties. Argon is the most efficient of the two pyrolysis atmospheres and results in the creation of ceramics containing FePd alloys.

Binary alloys of FePd have attracted considerable technological interest due to their high magneto-crystalline anisotropy, rendering them suitable for next generation hard-disk drives. In contrast to FePt alloys, they seem to retain a ferromagnetic groundstate even at small cluster sizes [162, 163]. As with Fe-oxide nanoparticles, the magnetic properties of FePd alloys depends on a number of parameters, including the size of the crystal and the composition [185]. Fe₅₀Pd₅₀ particles at room temperature have been reported to have a coercivity ranging from 200 Oe for 6 nm particles [162] to 1251 Oe for 40 nm particles [187]. The coercive fields seen here for FePd-containing ceramics are ~ 290–340 Oe. This is higher than the coercive fields reported for Fe-oxides, indicating that the enhanced magnetic behaviour is a result of the presence of FePd alloys.

Metal alloy nanoparticles and films are prepared using a number of physical and chemical methods [176, 188, 189] including sputter deposition under ultra high vacuum, electrodeposition and chemical vapour deposition. All of these methods require specialist equipment and can be costly and time consuming. By incorporating the Pd into iron-containing polymers, FePd containing ceramics can be produced cheaply and quickly in a one-step process. The polymer precursors can be molded or shaped prior to calcination, enabling the formation of structured and shaped ceramics [153]. Complex patterns can be templated using the self-assembly of block copolymers [190]. This self-assembly has been used to pattern organometallic polymers [165] with structures on the order of 10–20 nm [191]. Liu *et al.* [192] have recently shown that iron-containing polymer films can be structured on the nanoscale using an imprint method, with feature sizes of 50 – 100 nm. This feature size is similar to the grain sizes currently used in hard-disk drive technology. This structure is retained on pyrolysis to form the ceramics. Structuring of these Pd-containing ceramics in a sim-

ilar manner could be used to form regular arrays of pillars with desirable properties for data storage, providing an alternative to current data storage technologies.

6.4 Conclusions

In summary, it has been shown that PFEMS can be successfully doped with Pd, either as nanoparticles or by directly mixing Pd(acac)₂ to the polymer prior to film deposition, to form precursors for magnetic ceramics. These pure and doped PFEMS precursors all exhibited paramagnetic behaviour. Increasing magnetic susceptibility was observed with Pd content. On pyrolysis of the polymer precursors, ferromagnetic ceramics are formed for all samples. The magnetic behaviour is dependent on the temperature and atmosphere used for pyrolysis. For ceramics containing Pd, pyrolysed under argon at 1000 °C, FePd alloys were observed. The formation of these alloys results in enhanced coercivity, remanent magnetisation and saturation magnetisation of the ceramics.

The formation of FePd alloys is highly desirable due to their application in data storage technologies. However, to be relevant for these applications structured films are required with feature sizes ~ 50 nm. Previous work has shown that patterned precursors retain their structure on pyrolysis. Based on these results it is suggested that an imprint method, recently developed by Liu *et al.* [192], could be used to fabricate FePd containing ceramics for use in high-density magnetic data storage technologies.

IRIDESCENCE IN TROPICAL FERNS

Optically active structures occur widely in nature and have a range of roles in both fauna and flora [9]. These structures often produce vivid, pure, iridescent colours, such as those seen on the feathers of birds of paradise and the wings of butterflies [193, 194]. The structures producing the iridescence are very diverse, with three main mechanisms being observed; multilayer lamellae, diffraction gratings and periodically ordered three-dimensional structures that act as photonic crystals [195, 196]. Examples of these can be seen in figure 7.1. The function of colour in nature is equally varied [197], with visual roles including the attraction of mates [198], warning signals and camouflage and more physiological roles such as the control of thermal energy exchange [199], photoprotection or vision enhancement in eyes [200]. The butterfly *Cyanophrys remus* is an interesting example of the use of structural colour; the dorsal scales display a vivid metallic blue iridescence, while the ventral scales are a matt pea-green [201]. Both of these colourations come from three-dimensional photonic crystal structures located on the wing surfaces. The two sides of the wing have very different functions; the blue is used to attract mates, while the green is used as a camouflage mechanism when the butterfly is resting and the wings are folded, so called cryptic colouration.

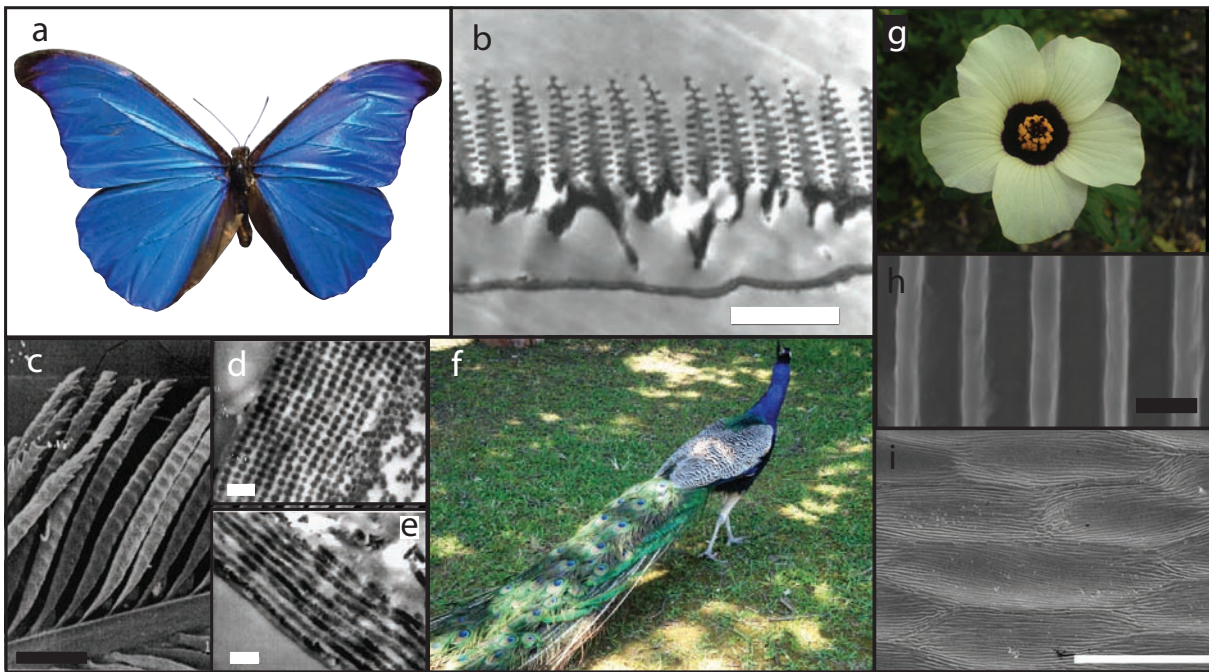


Figure 7.1: Optical structures in nature. (a) The butterfly *Morpho rhetenor*, (b) section through a scale showing a cuticle-air multilayer structure. (c) Barbules from a blue peacock feather. (d) Transverse and (e) longitudinal sections of a barbule from (c). (f) A Peacock. (g) *Hibiscus trionum*. (h) An epoxy cast and (i) a petal of (g) showing diffraction grating structure. Scale bars (b) 1.5 μm (d, e, h) 1 μm (i) 50 μm . Images from [202–204].

Optical structures are also seen in plants, but have not been as widely studied as those in insects and birds. However, they are equally as interesting and recent research suggests just as important [205–207]. Plants not only use light as an energy source for photosynthesis but also as an environmental signal. They respond to its intensity, wavelength and direction and attract pollinators or deter herbivores by reflecting light of a perceived colour. The multifunctional plant surface is one feature that plants can use to manipulate ambient light.

The structural mechanisms used by animals to cause the interference of light can also be seen in plants. One example is the plant Edelweiss (*Leontopodium nivale*), which is found growing in the Alps at altitudes of up to 3400m, where there is a high flux of harmful UV radiation. However, this does not seem to have any adverse effect on the plant. Vigneron *et al.* suggest that the reason for this are the tiny white hairs, which cover the leaves around the flower [195]. These hairs are seen to absorb all

incident UV radiation, before it reaches the leaf, providing a protective layer against damage. Protection against UV light is also thought to be the primary function of waxy deposits on the surface of *Dudleya brittonii* [208] and *Picea pungens* [209]. The leaves of these plants appear blue. The colouration is a result of Rayleigh scattering within the waxy layers on the surface of the leaves, with preferential scattering of shorter wavelengths. This acts to reduce relative penetration of UV light, giving protection against UV damage.

Iridescence generated through diffraction gratings, seen on the petals of tulips, has been shown to act as a cue to pollinators [202]. Instead of the conical cells found on other species of angiosperm flower petals, the cells are flat and elongated. The cuticle overlying the cells is arranged in raised stripes with long-range order. The periodicity is such that these ridges act as a diffraction grating. Whitney *et al.* demonstrate that bees can see the angularly changing colour of the iridescent structure on the petals and that the plants may use this to attract the pollinators. Tulips are not the only plant species to produce petals which have striated structures [210]. The location, patterning and visibility of iridescence to pollinating insects suggests that iridescence can enhance floral attraction for insects [205].

Optical multilayer structures are also observed in plants which grow in the understorey¹ of the rainforest. While the function of iridescent diffraction gratings in plants has a clear role, the adaptive advantage of multilayer structures seen on the leaves of several species is unknown. This chapter will discuss the multilayer iridescence seen in one such plant *Selaginella willdenowii* and the potential role that this iridescence has to play.

¹A layer of vegetation growing on the floor of the forest.

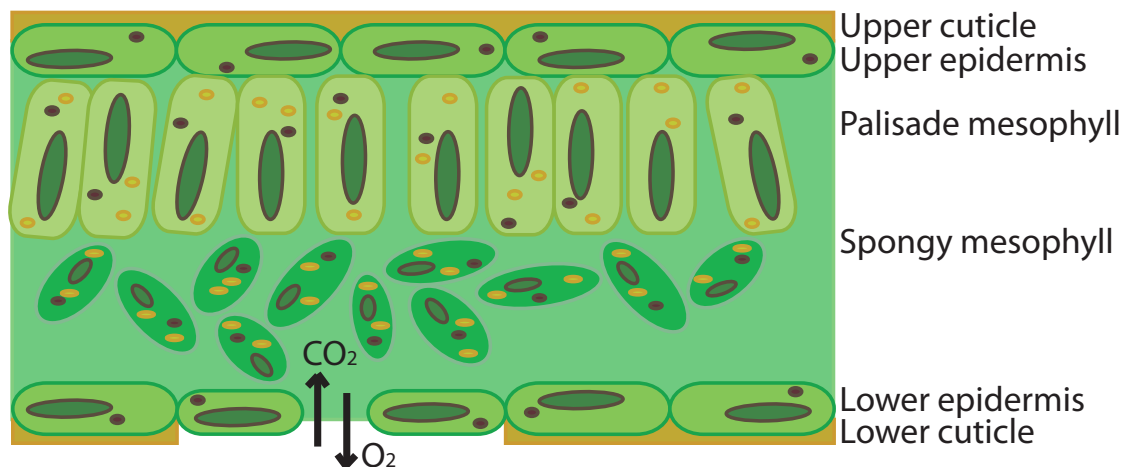


Figure 7.2: Cartoon schematic of a leaf showing the different layers. A leaf typically consists of the following tissues: An epidermis that covers the upper and lower surfaces, an interior called the mesophyll and an arrangement of veins (not shown here).

7.1 Introduction

The herbaceous ground flora of tropical rainforests grow under specialised conditions with high humidity and low light levels. The leaves of these plants often display unique features [211]. Some plants have velvety leaves resulting from cells in the epidermis which project as papillae [212]. The leaves are usually hydrophobic, which is thought to increase photosynthetic efficiency. Other plants are seen to have red pigmentation located in the mesophyll cells immediately beneath the palisade layer [213] (see figure 7.2). Initial studies suggested that the role of this pigmentation was to increase energy absorption by backscattering of transmitted light into the palisade cells. However, Hughes *et al.* have recently shown that this is not the case and instead that the red pigment acts to attenuate light damage during intermittent exposure to high-intensity light [214]. A third set of plants, which grow in deep shade, have leaves with a bluish iridescence [215].

One species that exhibits blue iridescence is the lycophyte *Selaginella willdenowii*, which is found growing in the rainforests of Malaya [216]. The colouration was initially thought to result from reflective granules present in the cuticle (the waxy layer

overlying the epidermal walls) [217,218]. However, no such granules have been found [216] and only the photosynthetic pigments found in chloroplasts can be extracted [219]. It has also been observed that the blue colouration of the microphyllous leaves disappears when they are made wet, or when they wilt [220], showing that the colour must result from an optical structure close to the leaf surface, rather than arising from pigment-based absorption. In *Selaginella willdenowii* the iridescence is attributed to a quarter wavelength interference filter [221]. Cross-sectional images show two 80 nm thick lamellae at the outer edge of the cell wall of the upper epidermis. These lamellae are not found in leaves which appear green. The iridescence is also seen to be dependent on the conditions under which the plant is grown. Lee *et al.* grew plants in light conditions with different red (R) to far-red (FR) ratios. They found that only plants grown under a R:FR ratio of at least 0.35 produced intensely blue leaves. The treatment was reversible; when plants were moved from one growth chamber to another, new growth was seen to develop the characteristics of the new chamber. However, this treatment was also seen to change the leaves in other ways [221].

Iridescence is also seen in the leaves of the ferns *Danaea nodosa*, *Trichomeanes elegans* and *Diplazium tomentosum* and in the angiosperm *Begonia pavonina*. In *Danaea nodosa* the iridescence is attributed to light interference from helicoidal alternating electron opaque and electron transparent layers of cellulose microfibrils in the plant cell walls, where between 18 and 30 parallel lamellae are observed [222] (figure 7.3b). For green leaves of *Danaea nodosa* these layers are either not present or of the wrong size. In *Begonia pavonina* and *Diplazium tomentosum* the blue colouration is attributed to specialised plastids termed iridoplasts adjacent to the lower periclinal wall of the adaxial epidermis [223] (figure 7.2a,c). These iridoplasts contain 16 alternating electron-opaque and electron-translucent bands, which are thought to form a stack of alternating high and low refractive index lamella resulting in thin-film multilayer interference. In *Trichomeanes elegans* the blue colouration is attributed to uniform grana stacks in specialised chloroplasts adjacent to the adaxial epidermis

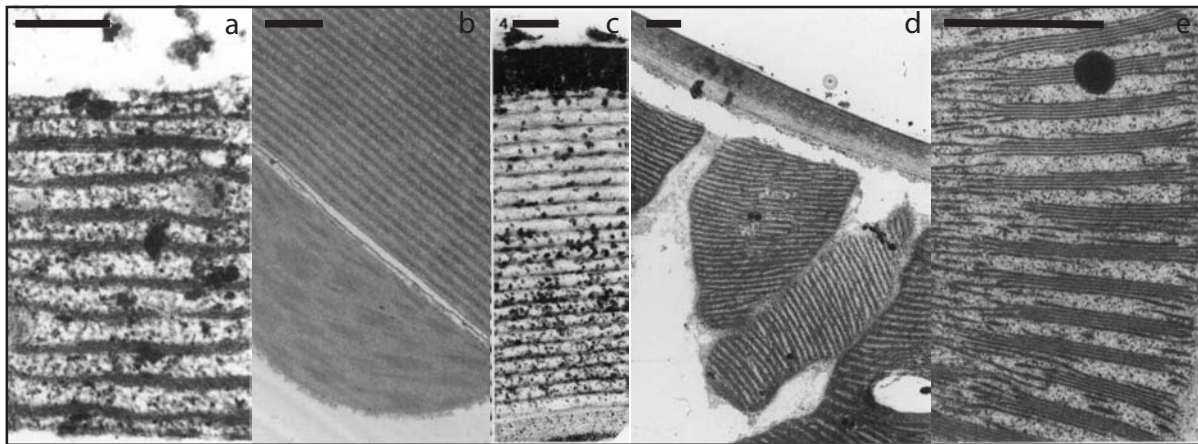


Figure 7.3: Multilayer structure seen in (a) iridoplasts of *Begonia Pavonia*, (b) upper epidermis of *Danaea nodosa*, (c) upper epidermis of *Diplazium tomentosum*, (d) chloroplasts of *Trichomeanes elegans* and (e) enlargements of (d) showing grana stacks within the chloroplasts. Scale bar (a,c) 0.5 μm (b,d,e) 1 μm . Images taken from [222, 223].

[222] (figure 7.3d,e). Golden-green iridescence is also seen in the moss *Schistostega* [224].

The way in which the colouration is produced strongly influences the wavelength of light for which iridescence occurs. For *Selaginella willdenowii*, where the colouration is a result of interference effects from lamella on the surface of the leaf, Lee *et al.* observed a blue peak in the reflectance at around 405 nm. However, for plants where the colour results from light interference within specialised plastids or chloroplasts, the peak in reflectance is observed at much longer wavelengths. The reflectance peak is seen at 480 nm for *Danaea nodosa*, at 446 nm for *Diplazium tomentosum* and at 530 nm in *Trichomeanes elegans*.

The function of blue iridescence in these plants is unknown. In *Trichomeanes elegans* the blue colouration does not come from surface interference filters and it has been suggested that the iridescence may be a by-product of ultrastructure with no selective advantage [222]. However, Graham *et al.* argue that since there is a strong association with extreme shade this suggests otherwise and the iridescence may alter internal light environments in a way that is advantageous to the plants.

Lee *et al.* hypothesise that the lamellae observed in *Selaginella willdenowii* function as an anti-reflective coating, reflecting light at short wavelengths and enhancing

the absorption of light at longer wavelengths through destructive interference [216]. Due to the filtering effect of foliage in the upper layers of the rainforests [225,226], the plants which grow in the extreme shade, receive light enhanced in the R:FR part of the electromagnetic spectrum; 520 – 620 nm and 700 – 1100 nm [227]. Light levels at the ground in the understorey have been reported to be between 0.1 – 1.9% of full sunlight [225]. An interference filter which suppresses the reflection of red light would allow for enhanced light capture for photosynthesis. However, it would also reduce the amount of light absorbed in the blue part of the spectrum, which is equally important for photosynthesis [228,229].

This work aims to further our understanding of the iridescence produced in leaves of *Selaginella willdenowii*. While the blue colouration exhibited on the leaves of this fern has been said to be iridescent, this has not been shown. Studying the optical properties of the plant quantitatively and systematically, will allow for the nature and source of the optical properties to be found and questions on the function of the colouration to be explored. The theory of light interference in multilayer structures is presented in section 7.2 followed by a discussion on the experimental methods used to study the ferns (section 7.3). The rest of the chapter then focusses on the results and the conclusions about the colouration and the role it has to play.

7.2 Theoretical Background

The majority of biological samples displaying iridescence do so as a result of thin-film interference. The structures consist of multilayers of alternating higher and lower refractive index transparent materials. At each interface a proportion of the light is reflected. The intensity of reflected light is dependent on the thicknesses and refractive indices of the layers and the wavelength of light.

The method described here for the determination of the reflectance from thin-film multilayer structures is based on the formalisms of Hecht [230] and Heavens [231] and approaches the problem using electromagnetic theory. All calculations are carried out for ideal thin-film systems, consisting of parallel sided layers.

7.2.1 A single interface

Consider light incident on a single interface between two transparent media (figure 7.4a). The two media are assumed to be homogenous lossless dielectrics, which extend to infinity. The origin in space is taken to occur at the interface and the incident light is assumed to be an idealised monochromatic electromagnetic plane wave. The form of the incident wave is then given by

$$\mathbf{E}_i = \mathbf{E}_{0i} \cos(\mathbf{k}_i \cdot \mathbf{r} - \omega_i t) \quad (7.1)$$

where ω is the frequency of the wave and \mathbf{k} is the wavevector. The subscript i denotes the incident wave. The reflected and transmitted waves are then given by

$$\mathbf{E}_r = \mathbf{E}_{0r} \cos(\mathbf{k}_r \cdot \mathbf{r} - \omega_r t) \quad (7.2)$$

$$\mathbf{E}_t = \mathbf{E}_{0t} \cos(\mathbf{k}_t \cdot \mathbf{r} - \omega_t t) \quad (7.3)$$

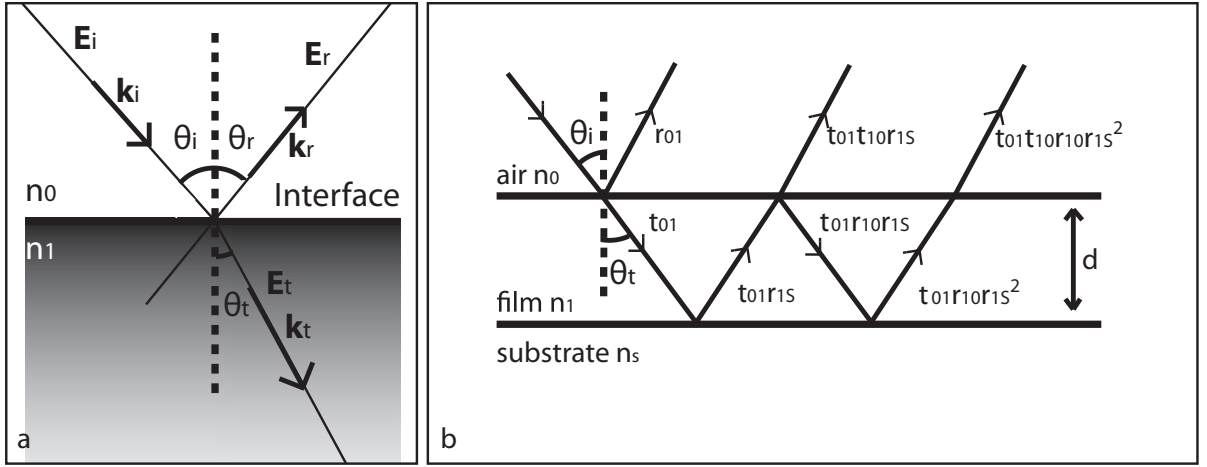


Figure 7.4: (a) Electromagnetic wave incident on an interface. (b) Successive reflected beams across a single film.

where the subscripts r , t denote the reflected and transmitted waves respectively. Considering the laws of electromagnetic theory, the boundary condition that the tangential component of \mathbf{E} is continuous across the interface, must be satisfied. This leads to the following

$$\omega_i = \omega_r = \omega_t \quad (7.4)$$

$$\theta_i = \theta_r \quad (7.5)$$

$$n_0 \sin \theta_i = n_1 \sin \theta_t \quad (7.6)$$

Equation 7.5 and equation 7.6 are the Law of Reflection and Snell's law respectively.

To find the amplitude of the reflected and transmitted waves, we consider separately, the components of the electromagnetic field perpendicular and parallel to the plane of incidence. Taking first the component of \mathbf{E} perpendicular to the plane of incidence, the boundary conditions require that \mathbf{E} is continuous across the interface such that

$$\mathbf{E}_{0i} + \mathbf{E}_{0r} = \mathbf{E}_{0t} \quad (7.7)$$

while the normal component of $\epsilon\mathbf{E}$ must be the same on both sides of the interface.

Physical phenomena of thin surface layers

From this the perpendicular amplitude reflection and transmission coefficients can be found, which are the ratios of $\mathbf{E}_{0r}/\mathbf{E}_{0i}$ and $\mathbf{E}_{0t}/\mathbf{E}_{0i}$ respectively.

$$r_s = \frac{\mathbf{E}_{0r}}{\mathbf{E}_{0i}} = \frac{n_0 \cos \theta_i - n_1 \cos \theta_t}{n_0 \cos \theta_i + n_1 \cos \theta_t} \quad (7.8)$$

$$t_s = \frac{\mathbf{E}_{0t}}{\mathbf{E}_{0i}} = \frac{2n_0 \cos \theta_i}{n_0 \cos \theta_i + n_1 \cos \theta_t} \quad (7.9)$$

Considering now the component of \mathbf{E} which lies in the plane of incidence, continuity at the interface requires that

$$\mathbf{E}_{0i} \cos \theta_i - \mathbf{E}_{0r} \cos \theta_r = \mathbf{E}_{0t} \cos \theta_t \quad (7.10)$$

remembering that $\theta_i = \theta_r$ the parallel amplitude reflection and transmission coefficients can be found and are given by

$$r_p = \frac{n_0 \cos \theta_t - n_1 \cos \theta_i}{n_0 \cos \theta_t + n_1 \cos \theta_i} \quad (7.11)$$

$$t_p = \frac{2n_0 \cos \theta_i}{n_0 \cos \theta_t + n_1 \cos \theta_i} \quad (7.12)$$

Together r_p , r_s , t_p and t_s are known as the Fresnel coefficients. The reflectance is defined as the ratio of the reflected power to the incident power. When there is no absorption $R_p = r_p^2$, $R_s = r_s^2$ and the transmittance is given by²

$$T = \left(\frac{n_1 \cos \theta_t}{n_0 \cos \theta_i} \right)^2 t^2 \quad (7.13)$$

7.2.2 A single thin film on a substrate

Consider now a thin dielectric film of thickness d deposited on a substrate, where the refractive indices of the film and the substrate are n_1 and n_s respectively (figure 7.4b).

² $R+T=1$

Both the substrate and air are considered to be non-absorbing layers. The incident beam can be divided into its reflected and transmitted parts. The amplitudes of successively reflected and transmitted beams can be written in terms of the Fresnel equations given by equations 7.8-7.12. To find the reflectance characteristics we must consider the reflected and transmitted waves at both the air/film interface and the film/substrate interface. The Fresnel coefficient for light reflected from the air/film interface is denoted by r_{01} and from the film/substrate interface by r_{1S} , where light is reflected toward the air layer. Similarly for light reflected from the film/air interface the Fresnel coefficient is denoted by r_{10} and from the substrate/film interface by r_{S1} , where light is reflected in the direction of the substrate. The transmission coefficients are similarly named.

From equations 7.8-7.12 we can see that $r_{01} = -r_{10}$ and $t_{01}t_{10} = 1 - r_{01}^2$. The phase change for a beam traversing the film is

$$\delta_1 = \frac{2\pi}{\lambda} n_1 d_1 \cos \theta_t \quad (7.14)$$

where λ is the wavelength of the light. The reflected amplitude is then found by considering the sum of the successive beams reflected at the air/film interface

$$r_{01S} = r_{01} + t_{01}t_{10}r_{1S} \exp(-2i\delta_1) - t_{01}t_{10}r_{01}r_{1S}^2 \exp(-4i\delta_1) + \dots = \frac{r_{01} + r_{1S} \exp(-2i\delta_1)}{1 + r_{01}r_{1S} \exp(-2i\delta_1)} \quad (7.15)$$

7.2.3 Multilayer reflections

For a multilayer consisting of a stack of alternating dielectric media, medium 1 and medium 2, with refractive indices n_1, n_2 , the reflectance can be found by considering each layer in turn (figure 7.5). Taking the bottom layer of the stack to be material 2 the reflection coefficient $r_{\text{bottom}} = r_{12S}$ can be calculated using equation 7.15, where the

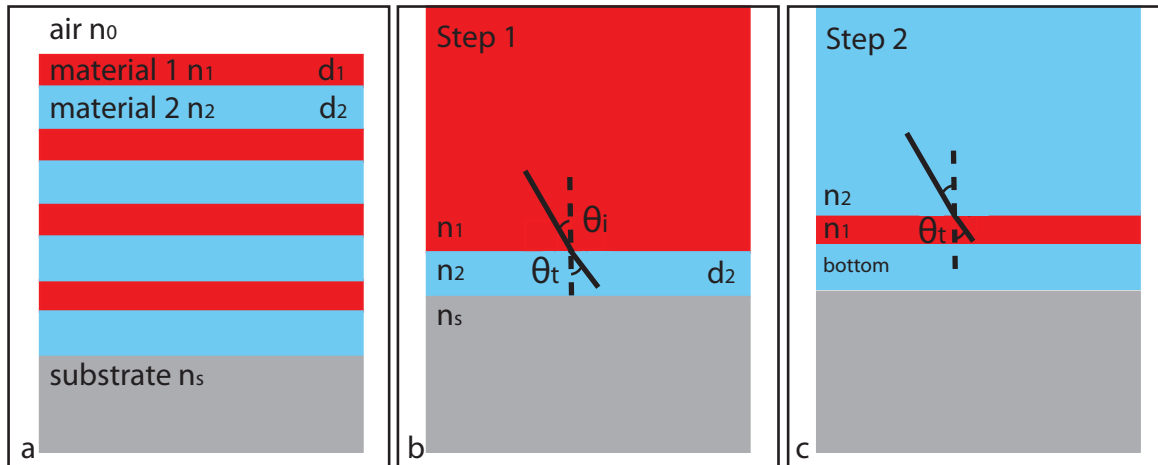


Figure 7.5: (a) Multilayer stack of alternating layers of material 1 and material 2. (b) Step 1: Reflections at the bottom layer are considered to determine a virtual complex refractive index of the bottom layer and the substrate. (c) Step 2: Reflections from the next layer up in the stack are considered taking into account the virtual refractive index of the bottom layer and the substrate.

upper medium is medium 1 and the lower medium is the substrate.

$$r_{\text{bottom}} = r_{12S} = \frac{r_{12} + r_{2S} \exp(-2i\delta_2)}{1 + r_{12}r_{2S} \exp(-2i\delta_2)} \quad (7.16)$$

Moving one layer up in the stack medium 1 can now be thought of as being sandwiched between medium 2 and a semi-infinite layer for which r_{bottom} is the Fresnel coefficient. The reflection coefficient r_{next} is given by

$$r_{\text{next}} = \frac{r_{21} + r_{\text{bottom}} \exp(-2i\delta_1)}{1 + r_{21}r_{\text{bottom}} \exp(-2i\delta_1)} \quad (7.17)$$

This continues until the air interface is reached. The reflectance of the multilayer stack is then $R = r_{\text{stack}}^2$.

7.3 Materials and Methods

Selaginella willdenowii plant material was obtained from The Royal Botanic Gardens Kew, accession number 1994-1186-RONI 57. The plant was grown in a glass house

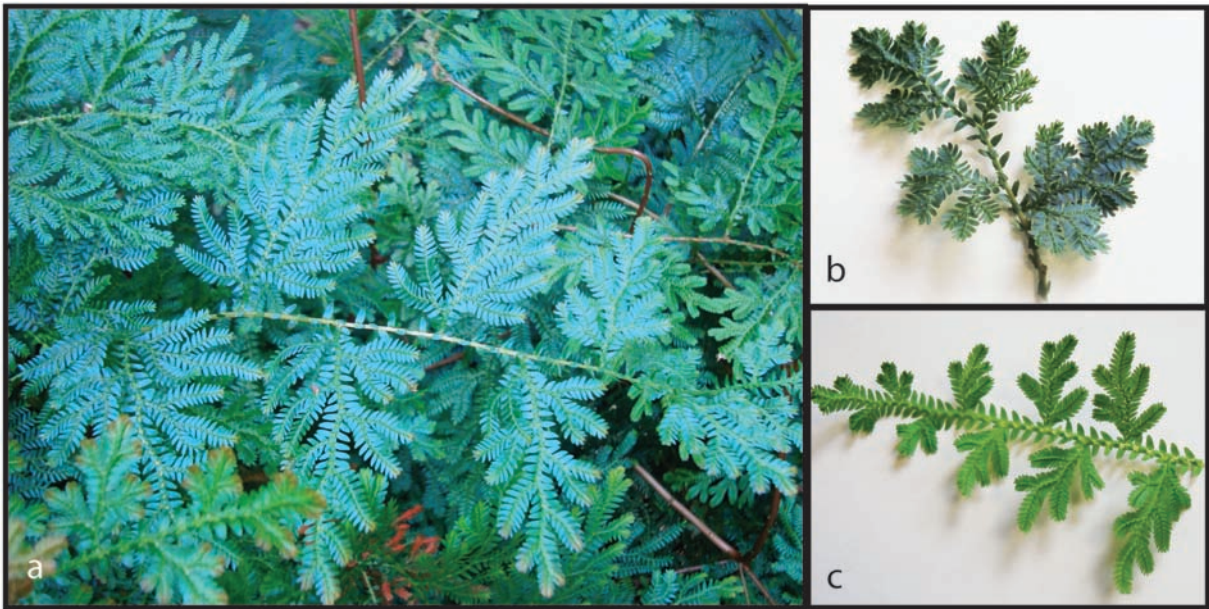


Figure 7.6: (a) Photograph of *Selaginella willdenowii* plant grown at The Royal Botanical Gardens, Kew. (b) Blue juvenile leaf. (c) Mature green leaf.

under the following conditions: night temperature 18 °C, day temperature 22 °C, vent temperature 25 °C, humidity 70 – 80%. The plants were grown under normal sunlight levels, with partial shading of the greenhouse for incident light with an intensity greater than 100 W/m² and full shading for incident light with an intensity greater than 200 W/m². Plant material from the same plant was also kept at the Cambridge University Botanic Garden and grown under the same conditions, with partial shading of the plant. A photograph of the plant grown at Kew can be seen in figure 7.6 along with photographs of individual young and old leaves.

Spectroscopy

Spectroscopic reflection measurements of *Selaginella willdenowii* were carried out using a fibre-optic based gonio-spectroscopic set-up, with independently adjustable light incidence and collection angles. The set-up can be seen in figure 7.7. An Ocean Optics DHL2000 light source with a combined deuterium halogen lamp provided a collimated 2 mm wide beam for illumination of the samples with light in the spectral range of 300 – 900 nm. Reflected or scattered light was detected with an Ocean

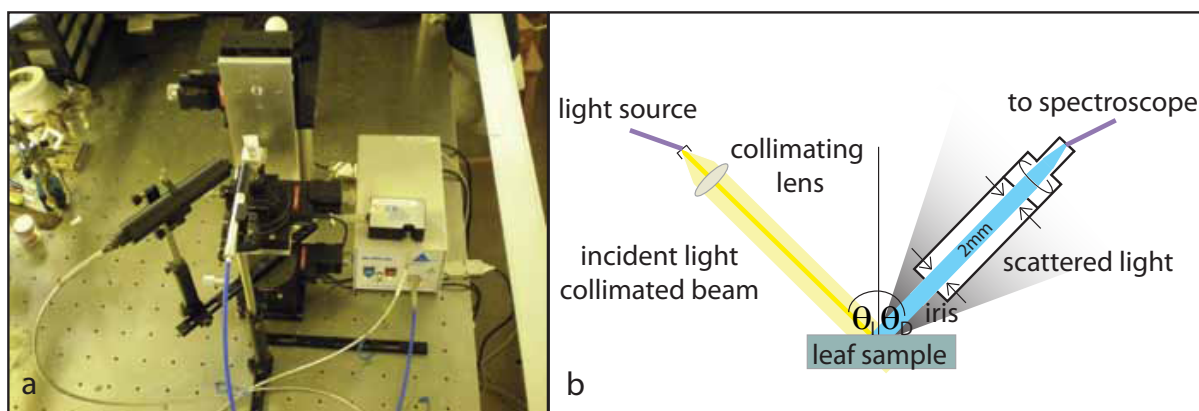


Figure 7.7: (a) Photograph of the gonio-spectroscope set up used. (b) Schematic representation of (a).

Optics USB4000 spectroscopy. The plant leaves were mounted on metal washers so that the leaves were flat and free standing. Both specular reflection and scattering measurements were carried out. For specular reflection measurements, the angle of light incidence θ_I , measured from the sample surface normal, was varied from 16° to 60° in 2° steps. The detection angle was adjusted to $\theta_D = -\theta_I$ in order to detect the specularly reflected light. For scattering measurements, the angle of incidence was fixed at 36° and the angle of detection was varied from 0° to 90° . The reflection measurements were normalised with respect to a Spectralon[®] diffuse reflectance standard of 99% reflectance. Absolute reflection measurements were carried out using a Labsphere[®] integrating sphere. Measurements were carried out on a mature green leaf and a semi-iridescent blue leaf.³

Microscopy

For ultrastructural studies small branches of the leaves were fixed in Karnovsky's fixative (2% paraformaldehyde, 2.5% glutaraldehyde in 0.1 M phosphate buffer at pH 7.2) overnight at 4°C . Sections $1 \times 2 \text{ mm}^2$ were then cut, rinsed in buffer and post-fixed in a 1% osmium tetroxide (Agar) phosphate buffer solution for 2 hrs. They were then rinsed in buffer and dehydrated in absolute ethanol solutions in steps from 30% EtOH

³Due to problems with growing the plants, a juvenile fully iridescent leaf was not available at the time of the integrating sphere measurements.

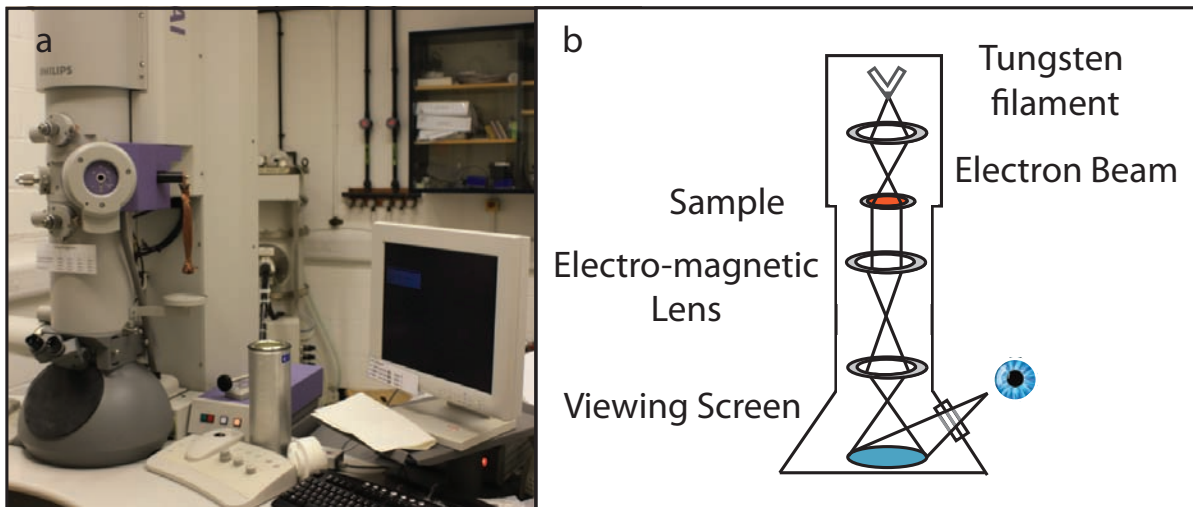


Figure 7.8: (a) Photograph of FEI Phillips Technai 20. (b) Schematic representation of (a).

to 100% EtOH. The material was embedded in optical grade LR Resin (Agar) and left for one week at 4 °C to allow the resin to infiltrate. The resin was changed daily. The samples were cured under vacuum at 400 mbar for 20 hrs at 58 °C. Thin sections were cut using a Leica Ultracut UCT microtome and stained using a Leica EM stain with uranyl acetate and lead citrate. Images were taken using a FEI Philips Tecnai 20 TEM at 200 kV.

Surface structures were obtained by taking casts of the leaves in dental wax. The cast was allowed to set. Once set the leaf was removed and the casts were then filled with epoxy. After the epoxy had set, the dental wax cast was removed, leaving a positive replica of the plant leaf [232]. This was imaged using optical microscopy. Specular reflection and scattering measurements were also made on the epoxy casts.

Transmission electron microscopy

Transmission electron microscopy (TEM) was used for ultrastructural imaging of the plant leaves. TEM allows for the imaging of thin sections of materials with a much higher resolution than other microscopy techniques; the resolution of the TEM is limited to about 0.2 nm as compared to light microscopy which has a resolution limit of 0.2 μm [233].

Physical phenomena of thin surface layers

The sample is irradiated with a beam of electrons, focussed using electromagnetic lenses. As the beam passes through the sample, the electrons interact with the sample. The level of this interaction depends on the electron density of the material present; the more dense a material, the more the electrons are scattered. A fluorescent screen at the bottom of the microscope is used to image the transmitted electrons, forming a 'shadow' image, where the sample is imaged according to the density of the material. More dense materials will appear darker, while less dense materials appear brighter. A schematic representation of a TEM microscope can be seen in figure 7.8 along with a photograph of the TEM used here.

Soft materials, such as plant leaves and polymers, often have a low scattering power resulting in low contrast between different components. This contrast can be enhanced through the use of staining. Widely used stains for biological samples include osmium tetroxide, uranyl acetate and lead citrate. Osmium tetroxide is used as a fixative and while it does have some staining ability, the contrast, which comes from a lack of unsaturated bonds in the specimen, is insufficient for epoxy resin sections, such as those used here. Uranyl acetate and lead citrate are both general biological stains with low specificity and are used to enhance the contrast of cells, tissues and secretions. While each stain can be used on its own, double staining provides enhanced resolution of small features as more components of the sample are stained. Results with lead citrate are also improved if osmium tetroxide has been used at some point during the fixation procedure [234].

7.4 Results

The spectroscopic measurements of the juvenile blue leaves and mature green leaves can be seen in figure 7.9. Both leaves were taken from the same branch of the same

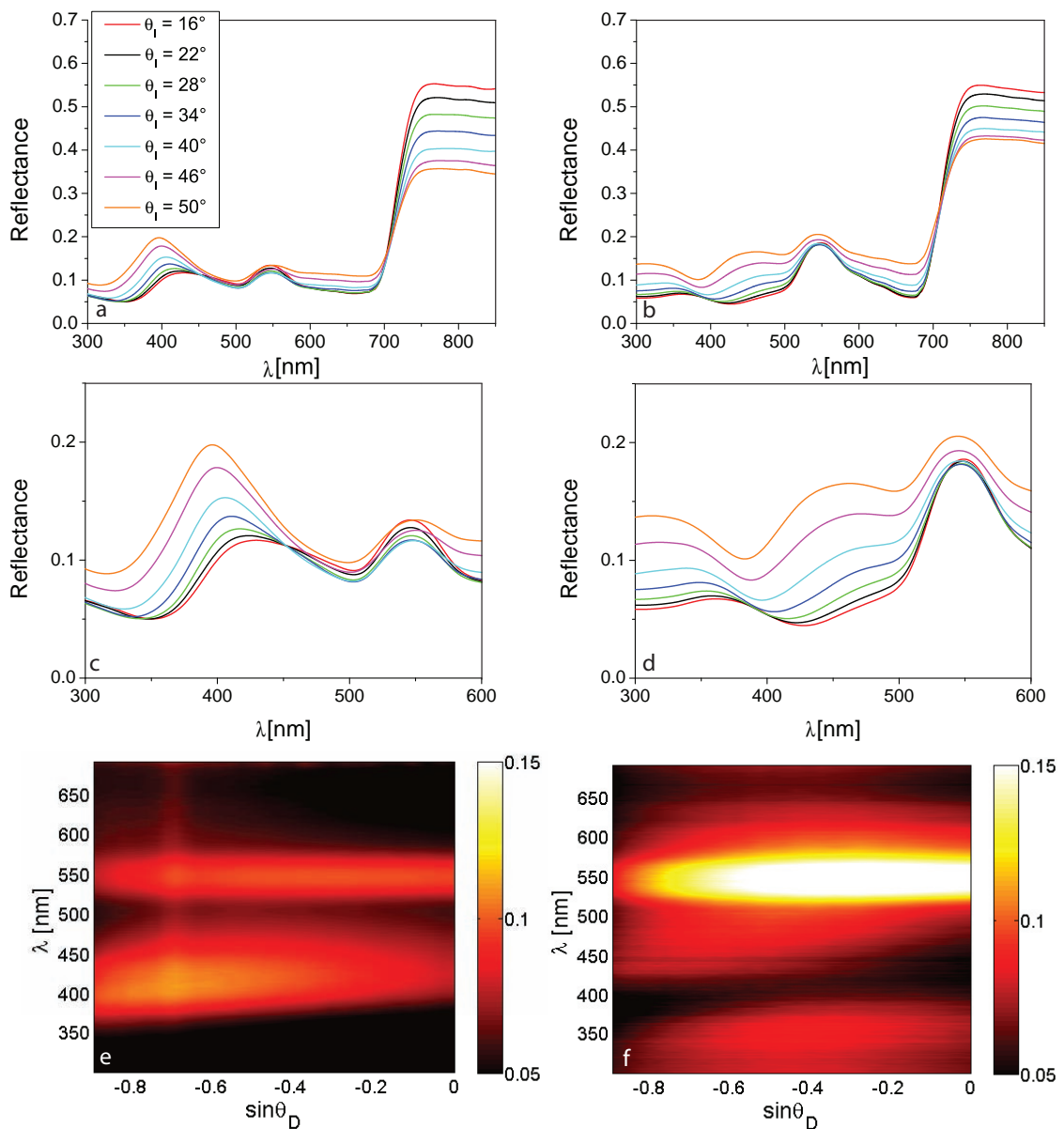


Figure 7.9: Specular reflection and scattering spectra of juvenile blue (left) and mature green (right) *Selaginella willdenowii* leaves. Intensity of specularly reflected light as a function of light incidence angle for (a) juvenile blue leaves and (b) mature green leaves. (c) and (d) Enlargement of the reflection peaks in the blue and green spectral range from (a) and (b), respectively. Scattered intensity as a function of detection angle for a fixed light incidence angle of 36° for (e) juvenile blue leaves and (f) mature green leaves. The intensity is colour coded, with red (dark) corresponding to a lower intensity and yellow (bright) a higher intensity.

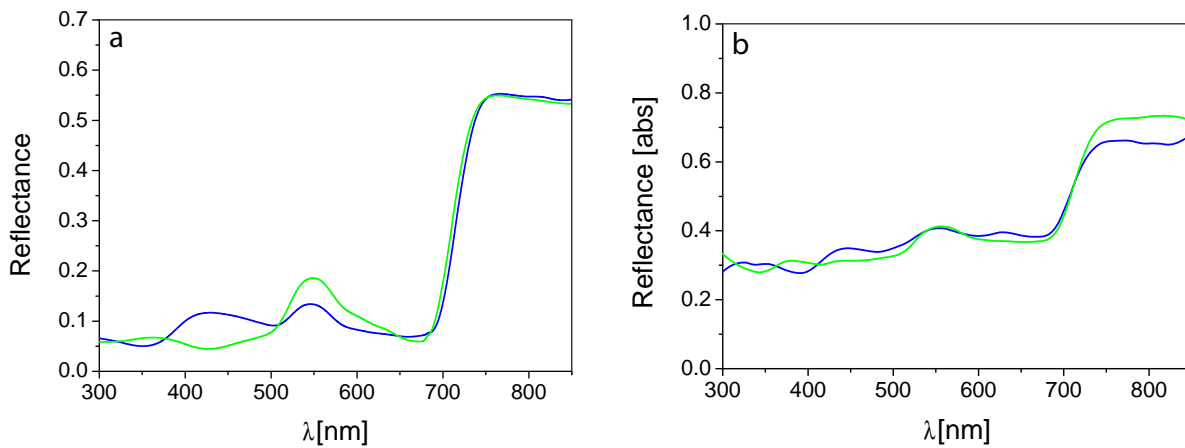


Figure 7.10: (a) Spectrally resolved specular reflection of juvenile blue (blue line) and mature green (green line) *Selaginella willdenowii* leaves at $\theta_i = -\theta_D = 16^\circ$. (b) Integrating sphere reflection measurements of blue (blue line) and mature green (green line) leaves.

plant. The blue leaf was from the newest growth on the branch, while the green leaf was from older growth. Leaves in between were seen to vary in colouration from blue to green depending on age. For the juvenile blue leaves a peak in the reflectance spectra is observed at around 430 nm in specular reflection, for an angle of incidence $\theta_i = 16^\circ$ (figure 7.10). This peak shifts to lower wavelengths when increasing θ_i from 16° to 50° (figure 7.9a, c) and is not present in the spectra measured for the mature green leaves (figure 7.9b, d). In both sets of data a peak at 545 nm is observed. This peak does not change position as θ_i is varied. The 545 nm peak has a 50% increased reflectance in the green leaf compared to the blue leaf, but the overall reflectance of both leaves is the same.

Figures 7.9e, f show the scattering measurements for the blue and green leaves respectively, for $\theta_i = 36^\circ$. The horizontal band at 545 nm stems from the green reflectance peak, seen for both leaves. This band is independent of the incidence and detection angles. For higher $|\theta_D|$ a weak peak is observed in the scattering data at around 450 nm in figure 7.9f, which is also present in the specular reflection measurements (figure 7.9b). This suggests that the multilayer stack of the juvenile blue leaf is still partially present in the green leaf. The different position of this peak in figure 7.9f as compared to figure 7.9e suggests that the thicknesses and/or contrast between the

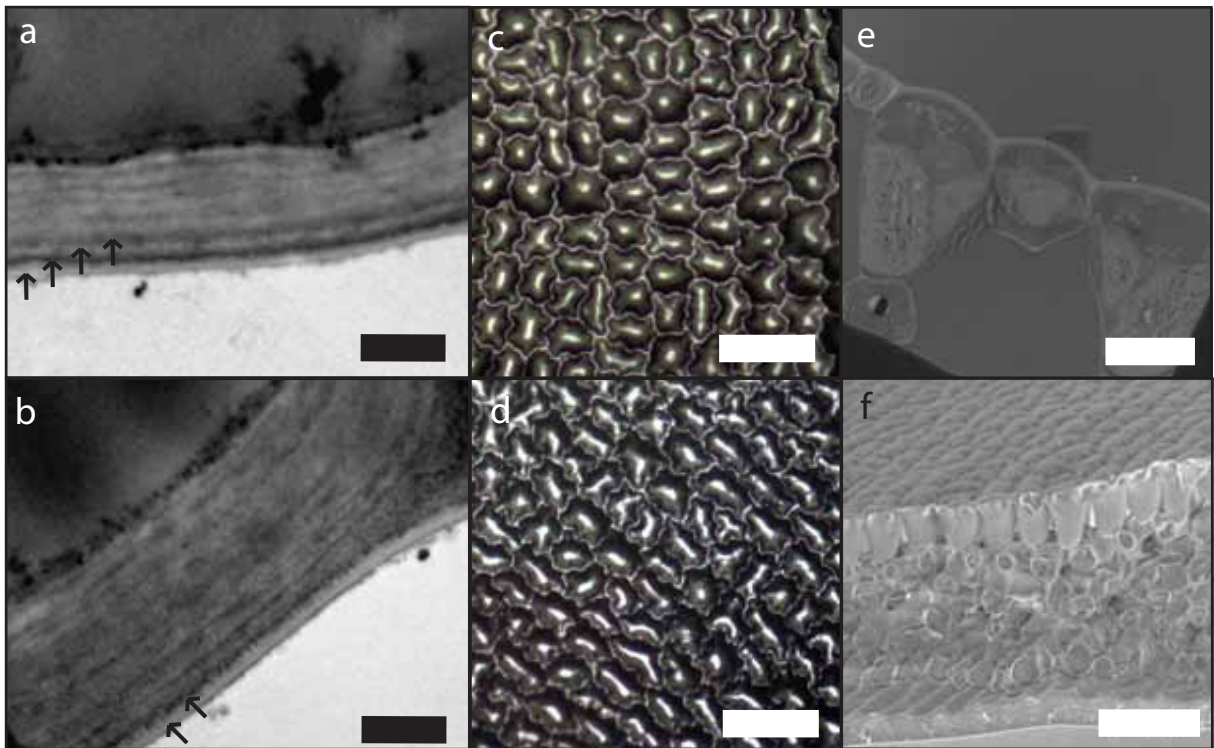


Figure 7.11: TEM micrographs of the outer cell wall and the cuticle from the upper epidermis of (a) a juvenile blue leaf and (b) an older green leaf. Scale bar is 500 nm. Arrows indicate the layers observed in the cuticle. Optical micrographs of surface morphology of plant cells for (c) a juvenile blue leaf and (d) a mature green leaf. Scale bar is 50 μm . (e) TEM micrograph of juvenile blue leaf showing cell structure. Scale bar is 20 μm . (f) ESEM micrograph showing leaf structure of a juvenile blue leaf. Scale bar is 50 μm .

layers has changed as the leaf has aged. The gradual increase in broad-band intensity for values from θ_D are intrinsic to our experimental configuration and independent of the sample; the spot size on the sample, from which the light is detected, increases with increasing $|\theta_D|$.

Figure 7.10b shows the experimental spectra for the integrating sphere measurements. The measurements were carried out on a mature green leaf and a semi-iridescent blue leaf. The blue leaf, while being the youngest growth on the plant was not a juvenile leaf. The results give an indication of the absolute reflectance of the leaves and show that the relative intensities of the leaves in the range 300 – 700 nm as measured in specular reflection are comparable (figure 7.10a). The spectra are averaged over three different measurements.

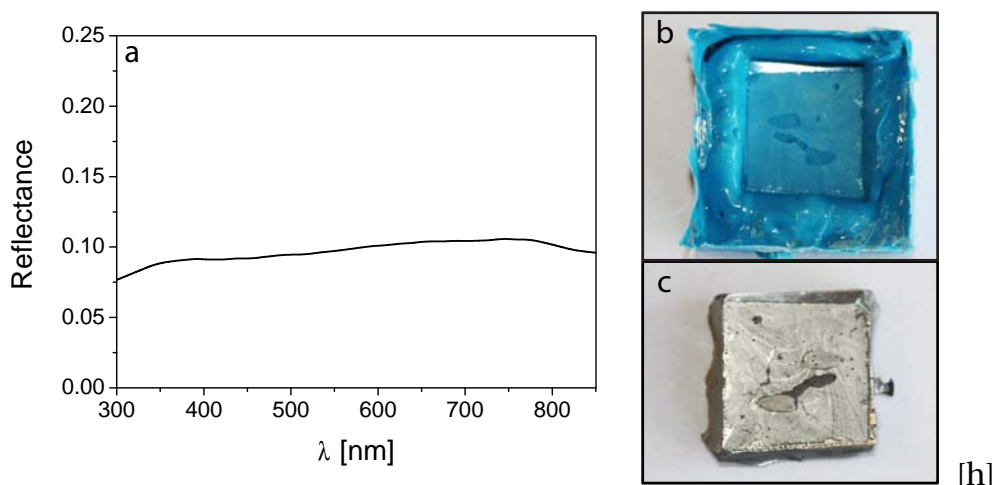


Figure 7.12: (a) Reflection of epoxy cast of a young blue leaf at $\theta_I = \theta_D = 16^\circ$. (b) Dental wax cast of a juvenile blue leaf. (c) Epoxy cast of (b), this has been coated with platinum for contrast.

Figure 7.11 shows cross-sectional TEM images of the blue and green *Selaginella willdenowii* leaves. The images show the outer cell wall and the cuticle from the upper epidermis of the leaves. In figure 7.11a four distinct layers are observed in the cuticle of the blue leaf, followed by a more disordered layer structure in the lower epidermis. These alternating light and dark bands correspond to electron-transparent and electron-opaque layers, respectively. This alternating layer structure is not visible in the cross-section of the green leaf (figure 7.11b). Instead, only a single dark layer is discernible, followed by a more disordered lamellar structure. The cuticle of the green leaf of $\sim 1.1 \mu\text{m}$ is much thicker as compared to the blue leaf $\sim 700 \text{ nm}$.

The surface structures of the blue and green leaves are shown in figures 7.11c, d. There is very little difference between the two images, both show epidermal cells arranged in disordered rows. The cells have a size on the order of $20 \mu\text{m}$. Spectroscopic measurements of the epoxy casts show a constant reflectance for $300 - 850 \text{ nm}$, which corresponds to the reflection properties of the epoxy (figure 7.12). This confirms that the surface cell structure does not contribute to the blue colouration seen in the young leaves.

7.4.1 Modelling

The results show that the position of the peak wavelength seen at ~ 430 nm decreases as the angle of incidence increases. From this it is reasonable to assume that the blue colour in the juvenile leaves comes from multilayer interference arising from the four lamellae observed in the upper cuticle. Optical modelling of a 4-layer structure was therefore used to account for the optical properties of the *Selaginella willdenowii* leaves.

The thickness of each layer was measured from TEM cross-sections (figure 7.11a). Layer one, the outermost layer, has a thickness of 66 ± 5 nm and layer two has a thickness of 50 ± 5 nm (as measured from cross-sections taken of three different iridescent leaves). The refractive index of cellulose is known to vary with the degree of hydration [235], with a more hydrated cellulose having a lower refractive index. It is therefore likely that the outer layer, L1, has a higher refractive index than the underlying layer, L2, which is presumably less hydrated. The refractive index of the underlying cell is approximately 1.36 as calculated by Charney *et al.* for the refractive index of plant cell cytoplasm [236].

The model structure is shown schematically in figure 7.13a. The lamellae L1 and L2, are approximated as homogeneous, transparent dielectric films with refractive indices n_1 and n_2 and thicknesses d_1 and d_2 . The reflectance of such a planar multilayer structure can be calculated by propagating a plane wave through the stack, considering interfacial reflections and interference using Fresnel's equations [237, 238] as discussed in section 7.2.

The experimental spectra for $\theta_1 = 16^\circ$ and the corresponding model calculations, are shown in figure 7.13b,d. While the model calculations allow us to confirm whether the peak in the experimental reflectance data corresponds to that of the model, the simple model does not predict the absolute intensity of the measured reflectance and therefore cannot be compared using this method. While the blue colour clearly arises

Physical phenomena of thin surface layers

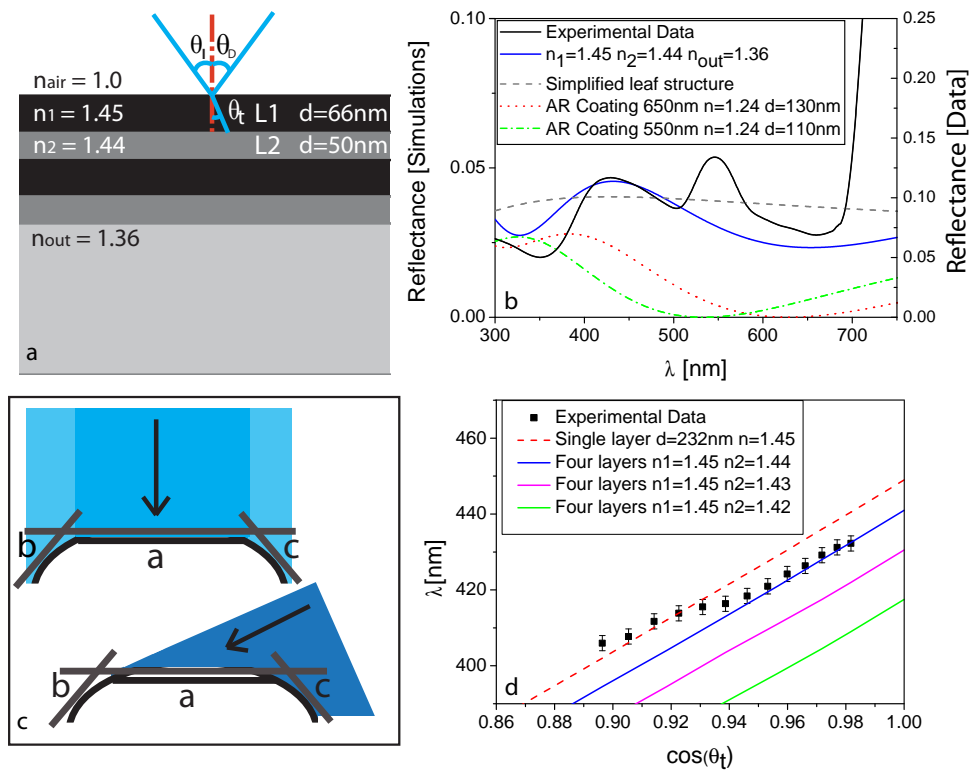


Figure 7.13: (a) Multilayer model. (b, d) Experimental data and simulated reflectance from an optical multilayer with $d_1 = 66$ nm and $d_2 = 50$ nm, with different combinations of n_1 and n_2 . (b) Simulations for a simplified leaf structure (dashed line) on top of a homogeneous optical medium. Simulated reflectance for the simplified leaf covered by an anti-reflective coating optimised for (red) 650 nm and (green) 550 nm, respectively. (d) Peak in the reflectance seen between 380 and 450 nm. Theoretical peak shift as calculated using (a) (blue line). Theoretical peak shift for other combinations of n_1 and n_2 (pink and green lines). Theoretical peak shift for a simplified structure with $d = 232$ nm (dashed line). Black points show experimental data and are an average of three measurements. (c) Contributions from faces a, b and c for light with normal incidence and light with a higher incident angle.

from multilayer interference, the optical signal stemming from the overall structure of the leaf is complex. Its optical signature is a superposition of Bragg interference with intensities arising from scattering off irregularities at the surface and in the multilayer, backscattering of light from the cytoplasm and variations in the surface-normal of the multilayer due to the cell shape and leaf curvature (see also below). The measurements also do not take into account any polarisation effects of the multilayer; the reflected intensity varies as a function of polarisation. All simulations shown here are for unpolarised light.

The model assumes that $d_1 = 66$ nm, $d_2 = 50$ nm, $n_1 = 1.45$, $n_2 = 1.44$ and $n_{\text{out}} = 1.36$. Figure 7.13d shows the wavelength λ_{max} of the multilayer reflectance peak as a function of incidence angle for the juvenile blue leaves. The wavelength is averaged over spectra from three different leaves. While the data extracted from the specular reflection experiments (points) are well described by the model calculation (blue line) for small angles of incidence, the model and the data deviate for higher angles. The model assumes planar, horizontally flat homogenous layers. The shape of the epidermal cells are however, dome-shaped (figure 7.11c). The cell morphology determines the local optical geometry. For normal incidence, the flat top part of the cell locally approximates the planar surface of the model in figure 7.13a. For larger incident angles more light impinges on the cell edges, which now play an increasing role. The local angle of light incidence at the illuminated cell edges is smaller than the global incidence angle. The reflected intensity detected at $\theta_D = -\theta_I$ results from superposition of the light that is specularly reflected from the top part of the cell and light that scatters from the cell edges (figure 7.13c). The detected wavelength is consequently red-shifted compared to the planar multilayer model, somewhat reducing the iridescent nature of the blue peak.

Other combinations of n_1 and n_2 were also simulated, to assess whether different configurations would result in the same reflectivity behaviour. Figure 7.13d shows that increasing the refractive index contrast between the two layers shifts the peak in the reflectance to lower wavelengths than those found experimentally.

The small enhancement of the specular reflectance at around 450 nm for the green leaf (figure 7.9b) seen at high angles is consistent with a double layer interference filter with $n_1 = 1.45$, $d_1 = 75$ nm and $n_2 = 1.44$, $d_2 = 25$ nm. This corresponds to the two partial lamellae seen in figure 7.13b. For small θ_I , this maximum broadens and shifts to 500 nm, almost disappearing into the peak at 500 nm that results from scattering pigments in the leaf.

7.5 Discussion

Our detailed reflectance measurements show that the blue colouration seen in juvenile *Selaginella willdenowii* leaves is iridescent and stems from the four-layer interference filter in the cuticle on the upper surface of the leaves. The blue iridescence disappears as the leaf ages. The TEM images and reflection data suggest that the loss in the blue colouration comes from a degradation or increasing disorder of the multilayer structure, starting with the lower layers. For the older green leaves, only weak double layer interference is still present.

Modelling of the data suggests that the refractive index contrast between the two layers is on the order of 0.01. This difference is very small compared to other optical multilayers found for example in beetles and butterflies. Here however, the layer structure consists of only one material and the refractive index variation arises from a difference in hydration. This strongly limits the achievable refractive index contrast. The comparison of model calculations with experimental spectra confirms that the observed blue iridescence can arise from such a weak refractive index contrast.

Figure 7.9e shows a blue reflection band stretching across a wide range of detection angles. The ideal planar Bragg multilayer assumed in the model calculations would result instead in a localised specular signal at $\theta_D = \theta_I$ (i.e. at $\sin \theta_D \approx -0.6$) with little intensity at other angles. The wide blue intensity band of figure 7.9e stems from the disorder in the surface-normal of the multilayer. This disorder arises from the cell shape and from the curvature of the leaves. As a result, parts of the leaf locally fulfil Bragg's condition for any observation angle causing the angle-invariance of the observed colour. A similar optical response is seen for other natural multilayer structures. For example, the blue iridescence of *Morpho rhetenor* has a similar angle-invariance arising from the curvature of the multilayers on its wing-scales [239, 240]. The simple model used to describe multilayer interference therefore only approximates the optical response of the complex surface structures found in nature.

Modelling of the data shows that the multilayer structure preferentially reflects light in the blue part of the spectrum, a photosynthetically important spectral region, which is deficient in the light present in the natural habitat of these shade-dwelling plants. In this low-light environment the light is enriched in the R:FR part of the spectrum. Lee *et al.* have suggested that the blue-reflecting multilayer more effectively couples the long optical wavelength into the leaf, thereby enhancing photosynthesis. Our more detailed data allows the testing of this hypothesis.

A comparison of figures 7.9a and b shows that the reflectance in the 600 – 700 nm spectral range is strongly angle dependent. For the more important small angles of incidence, the average log wavelength reflectance is comparable. This is best seen in figure 7.10 where reflectance of the green leaf dips below the that of the blue leaf for ~ 660 nm, the maximum for red-absorption of chlorophyll.

Due to the complex optical signature of leaves, it is instructive to address the question of enhanced red-adsorption in terms of model calculations. The dashed line in figure 7.13b is the prediction for a simplified leaf structure consisting only of an optically dense top cuticle layer and an optically less dense lower phase. The predicted optical response of this simplified leaf structure in the 600-700 nm spectral range is very similar to the model 4-layer structure of the blue leaf. While this comparison illustrates the unsuitability of the multilayer to couple red light into the leaves, it is perhaps instructive to compare the measured spectra to optical coatings that are optimised for this effect.

Antireflective coatings consisting of a bilayer of low and high refractive index materials are well known. The optimisation condition for such a bilayer is $n_{\text{out}}n_1^2 = n_2^2$, with $\lambda/4$ thicknesses for each layer [242]. Superimposing the simplified leaf (dashed line in figure 7.13b) with a 110 – 130 nm thick layer of refractive index $n = 1.24$ significantly reduces the reflected light not only for the optimised wavelengths of 550 nm (dash-dotted line) and 650 nm (dotted line), respectively, but over most of the visible spectrum. The possibility of optical coatings consisting of porous or nanostructured

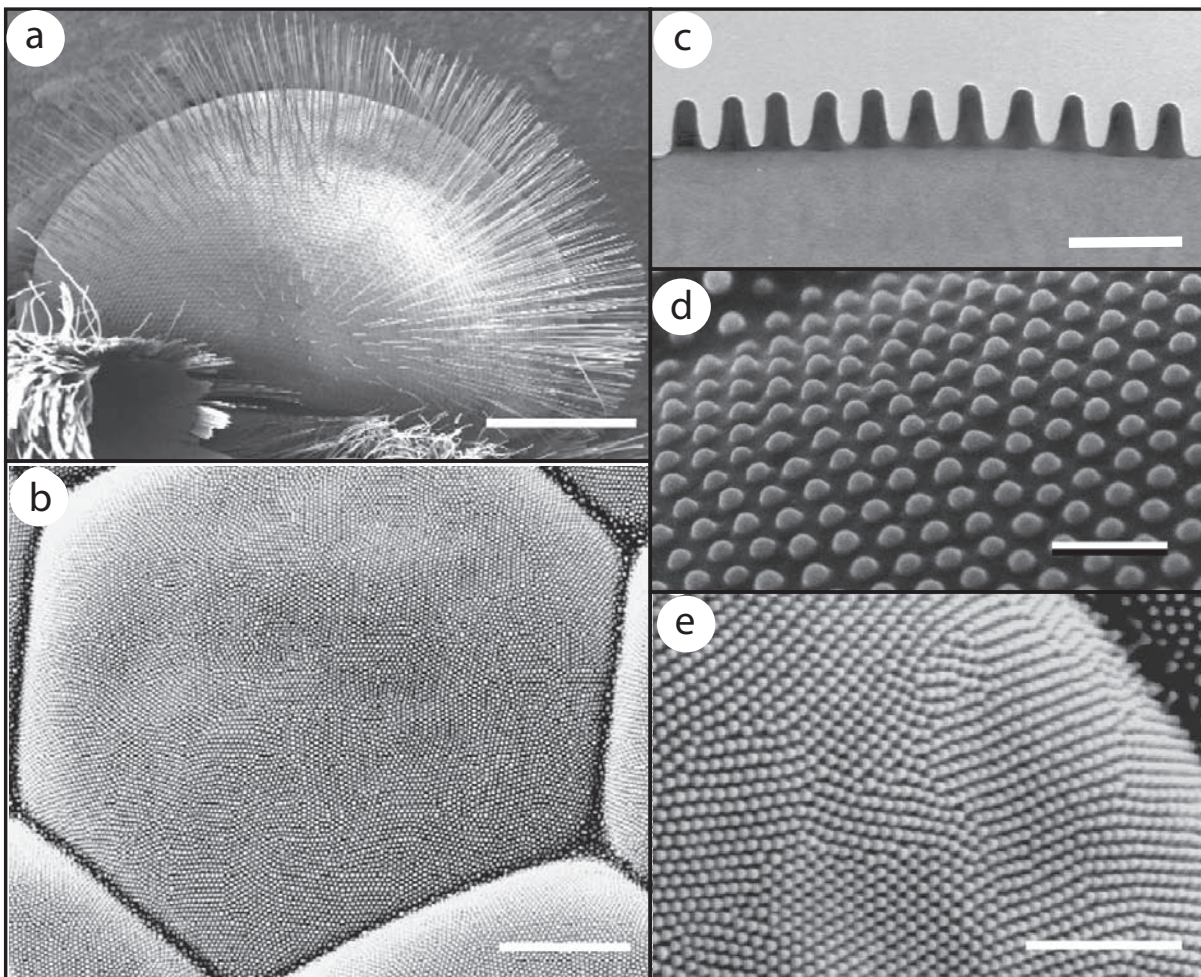


Figure 7.14: (a) Complete eye of the peacock nymphalid butterfly *Inachis io*. (b) Nipple array of one facet lens of (a). Corneal nipple array in (c) the nymphalid *Bicyclus anynana*, (d) the lycenid *Pseudozizeeria maha* and (e) in *Inachis io*. Scale bars (a) 500 μm , (b) 5 μm , (c,d) 500 nm and (e) 2 μm . Pictures taken from [241].

cuticle, becomes evident when considering the coatings found on the eyes of moths and on butterfly wings [241], where a wide variety of optically active nanostructures are observed (figure 7.14).

Figure 7.10 shows that the juvenile blue leaves have a lower reflectance between 500–600 nm as compared to the mature green leaves and a similar reflectance between 600 – 700 nm. A similar behaviour is seen for *Danaea nodosa*, where the iridescence is seen in the juvenile leaves and disappears in the adult leaves due to the loss of the multilayer structures responsible for the iridescence [222]. Graham *et al.* also studied the difference in the optical properties of twelve rainforest sun and thirteen rainforest

extreme shade plants [243], including iridescent species. Their results show that the absorption spectra of sun and extreme shade plants are identical apart from a small increase for the shade plants at 550 nm. Our data and model calculations show that the role of blue iridescence in *Selaginella willdenowii* is not to couple in more red light, refuting the hypothesis by Lee *et al.*

7.6 Possible adaptive advantages of iridescence

A taxonomically diverse range of photosynthetic organisms, from diatoms [244] to algae [245–247] through to angiosperms [222], produce a vivid iridescence over the surface of their photosynthetic apparatus. An equally diverse range of methods are used to produce this iridescence. This strongly suggests that the production of iridescence has evolved multiple times and has some unknown adaptive advantage for life in deep shade.

Our results show that it is unlikely that a multilayer structure acts to increase light capture in photosynthetically important wavelength ranges under low light conditions in this case, since no enhancement of absorption by the blue leaves is seen in the red part of the spectrum. While an interesting hypothesis, this idea is counter intuitive for a number of reasons. Firstly, it makes no sense that the plant would want to sacrifice the absorption of any incident blue light in favour of red light. Blue light is important for both photosynthesis and plant development.

Secondly, the multilayer filter does not act as an effective anti-reflective coating. As shown in figure 7.13b, a simple strategy to implement a broad-band antireflective coating consists of the deposition of a low refractive index ($n = 1.24$) $\lambda/4$ layer on top of a generic leaf surface. Compared to optical multilayers, a porous or structured low refractive index surface layer is optically more robust and presumably less resource intensive for the plant. The evolutionary feasibility of this is well documented in insects [241]. Stavenga *et al.* show that the papillae seen on the eyes of butterflies,

Physical phenomena of thin surface layers

act to produce a graded refractive index surface layer, which acts as an antireflective surface.

Increased capture of photosynthetically important wavelengths is not the only adaptive advantage that leaf iridescence may offer. Others include a visual defence against herbivores, a photoprotective mechanism to protect shade-adapted plants against sun-flecks and other potentially damaging sudden high light levels and a polarisation filter enhancing orientation of photosynthetic apparatus within the cell.

A visual defence against herbivores

Whitney *et al.* have recently shown that insects can see iridescence independently of any other cue [202]. Iridescence can act to increase detectability due to the changing colour of the object when perceived from different angles, delivering more stimulus to the photoreceptors of the eye. However, this may come with a cost; the very changeability of iridescence that increases detectability could corrupt object identity, making it harder for insects to form a search image [248]. In certain situations this potential corruption of identity could be a significant advantage. The constantly changing colours produced by iridescence would alternatively blend or contrast with any background, producing an effect similar to conventional disruptive colouration, like that of the zebra [249, 250]. The iridescence produced on the leaves of plants could act to confuse moving insects and herbivores by camouflaging the shape and edge of the leaf and making it difficult to form a target search image.

Alternatively the iridescence may serve to deter herbivores by causing the leaves to look sufficiently different to all other food sources that iridescent leaves are not recognised as food, or avoided. Evidence for these hypotheses has been found in the iridescent alga *Mazzaella flaccida*, where non-iridescent thalli of this seaweed were seen to suffer more from herbivory than their iridescent counterparts [247].

A photoprotective mechanism

All of the plants that produce blue leaf iridescence grow in extremely sheltered low-light environments and as such are thought to be strongly shade-adapted. Such plants would be extremely vulnerable to photodamage if even transiently exposed to sun flecks (where small patches of light break through the canopy), due to the increased sensitivity of their photosynthetic apparatus. The constructive interference produced by the blue leaf iridescence in the wavelengths of 400 – 485 nm may therefore function to protect against photoinhibition (the inhibition of photosynthesis due to excessive irradiance) and damage via reduced light absorption at those wavelengths [251]. Light attenuation mechanisms have been suggested for other shade dwelling plants, which have red leaves due to the presence of anthocyanins. These pigments are seen to function in light attenuation by intercepting quanta which would otherwise be absorbed by the chlorophyll, protecting the leaves from photoinhibition when exposed to sun flecks [214, 252].

A polarisation filter

If optimised for this purpose, optical multilayers can enhance the polarisation of light that occurs upon reflection and transmission at each surface. Ferns in particular have been shown to respond to light polarised in a particular plane, a response known as polarotropism [253]. Two features of plants appear to be key for the polarotropic response, the ordering of the cellulose fibrils within the cell wall and plant photoreceptors with a dichroic function.

There are two potential functions that iridescence could be fulfilling if its role is to act as a polarisation filter. Firstly, polarisation of light might enhance orientation of photosynthetic apparatus within the plant cell and thus increases photosynthetic efficiency [254, 255]. Secondly, by determining the plane of light polarisation additional information about a rare resource might be obtained.

Theories of how polarised light may be used as an additional environmental cue

Physical phenomena of thin surface layers

are found mainly in the insect vision literature. The spider *Dracones cupreus* has a pair of specialised secondary eyes that, like the iridescent leaves of *Selaginella willdenowii*, strongly reflect blue light. These eyes act as polarising filters, with one eye permitting the passage of horizontally polarised light, the other permitting the passage of vertically polarised light. The spider can use the ratio of light in each eye to determine the polarisation angle of light around it in the environment, which in turn can be used for navigation [256].

In the forest environment in which shade-adapted iridescent plants occur, direct sunlight is obscured. While the light that has been transmitted through other leaves is unpolarised, any light that is reflected from the vertical sides of trees is generally perpendicularly polarised and light reflected from leaves is predominately parallel polarised [257, 258]. The polarisation of light reflected from leaves under these conditions could potentially provide more detail about the surrounding environment, allowing modulation of development of physiological processes to maximise fitness. In particular, changes to the polarisation environment resulting from the fall of trees might provide opportunities for light capture or threats to sensitive photosynthetic machinery, both of which might result in plant acclimation. It would therefore be interesting to include polarisation measurements in future quantitative optical studies of *Selaginella willdenowii*.

7.7 Conclusions

In summary, it has been shown that the blue colouration seen in the leaves of *Selaginella willdenowii* is indeed iridescent. For an angle of incidence of 16° a peak in the reflectance spectra is observed at 430 nm. As the angle of incidence is increased, this peak shifts to lower wavelengths.

Transmission electron microscopy studies reveal a layered lamellar structure in the upper epidermis of the leaves. Modelling of the thin film multilayer structures

confirms that they are responsible for the iridescence observed in the leaves. As the leaves age the blue colouration is seen to disappear, with older leaves of the same plant appearing green. Comparison of the juvenile blue and mature green leaves indicates that the loss of blue iridescence corresponds to a loss and disorder of the multilayer structures.

The results reported here do not support the idea that iridescence in *Selaginella willdenowii* acts to enhance light capture of photosynthetically important wavelengths. The reflectance of light in the range 600 – 700 nm is the same for both iridescent and non-iridescent leaves. However, due to the occurrence of blue colouration in a wide variety of shade dwelling plants it is likely that this iridescence has some other adaptive benefit.

CONCLUSIONS

This thesis covers a number of different thin film phenomena, from the intrinsic behaviour and stability of thin films, to their potential use in hard-drive disk technologies, to the stunning optical effects that films can be used to produce. This chapter summarises the main conclusions of the work, discuss their implications and possible directions for future research.

Thin film polymer blends

In chapter 3 the stability of thin film polystyrene (PS)/ poly(vinylmethylether) (PVME) blends was investigated. These polymers are miscible at room temperature and phase separate upon heating. The behaviour of varying blend compositions was studied at temperatures where the PS and PVME are miscible. The PVME was seen to enrich the polymer/air interface, forming a layer with a width comparable to the correlation length of the PVME. Further heating close to the demixing temperature resulted in the formation of capillary instabilities at the polymer surface. These exhibited a spinodal-like pattern with a characteristic wavelength dependent on the blend composition. The formation of these instabilities was observed for all blend compositions investigated.

Physical phenomena of thin surface layers

Dr. Nigel Clarke at the University of Durham had previously shown, using a thermodynamic model, that when thin binary mixture films are subject to coupled height and composition fluctuations, the film is more unstable than if either the height or concentration fluctuations are considered in isolation. In collaboration with Clarke, his model was adapted for this system, taking into account the composition dependent Hamaker constant and the experimental parameters. The model showed good agreement with the experimental data, suggesting that the instabilities observed in the blend resulted from coupled height and composition fluctuations within the PVME wetting layer.

The formation of instabilities was only observed when the blends were heated close to the demixing temperature. PVME wetting layers were also observed to form at the polymer/air interface for blends kept at room temperature for extended periods of time. These blends were stable; no instabilities were seen. It would be interesting to find the temperature at which the blends become unstable and whether the annealing temperature, influences the wavelength of the instabilities that form.

Non-equilibrium behaviour of thin films

In chapter 4 thin films were destabilised using an electric field, in order to probe the effects of sample preparation on the rheology and stresses within the film. Films were spun from five different solvents: toluene, trans-decalin, chloroform, tetrahydrofuran and methylethylketone. The casting solvent had a strong effect on the onset time and the wavelength of the instabilities that formed.

The characteristic time of destabilisation is directly proportional to the film viscosity. The experimental onset times were much smaller than those predicted from linear stability analysis using bulk viscosity of the polymer and varied with casting solvent quality. The discrepancy is explained in terms of non-equilibrium effects caused by the spin coating process; the fast evaporation of the solvent from the films during spin coating creates a lower entanglement density in the film compared to that of an

equilibrium melt. This results in an increased mobility of the chains. The difference between the films spun from the various solvents can be explained by the changes in chain conformations in the initial solutions and the amount of solvent remaining in the film at vitrification.

The characteristic wavelength of the instabilities in as-cast films was observed to be higher than the theoretical value, indicating a weak stabilising pressure in the films. These could arise from frozen-in normal stresses in the as-cast films. In addition the wavelength was dependent on the casting solvent, with the greatest wavelength being observed for films spun from toluene and the smallest for films spun from trans-decalin. It is suggested that spin-coating results in an asymmetric deformation of the chains due to evaporation of the remaining solvent in the film after vitrification. This deformation is possibly dependent on the conformation of the chains prior to vitrification and on the molecular weight of the polymer.

Both the frozen-in normal stresses and viscosity deviations were removed upon annealing the films above the glass transition temperature. The time scale on which the frozen-in stresses were removed was much less than the annealing time required to restore bulk viscosity. This suggests that local rearrangements of the chains are sufficient to remove the anisotropy responsible for the residual stress. Recovery of bulk viscosity however, requires complete equilibration of the chains and much longer annealing times.

The results indicate that the boiling point of the solvent, the film formation time, the solubility of PS in the solvent and the amount of solvent remaining in the film on vitrification are all significant. No single property could be used to consistently describe the trends observed in the data. Instead the behaviour observed must result from a combination of all of these parameters.

The behaviour observed in these experiments can be explained in terms of the entanglements of the polymer chains. On these length scales, the chains can be considered as being far from equilibrium in the as-cast films. In polymer films the glass

Physical phenomena of thin surface layers

transition temperature has been observed to deviate from the bulk value, even when relatively thick films are investigated. The reason for this deviation is not well understood.

The glass transition temperature is dependent on effects happening on the segmental length scale of the polymer chain. This work shows that the polymer chain is far from equilibrium at the entanglement length scale and raises questions about what is happening on the segmental length scale. Are the chains also far from equilibrium on the segmental length scale and is this responsible for the deviations in the glass transition temperature observed? A possible extension of this project would be to prepare polymer films as far from equilibrium as possible. By using a Langmuir-Blodgett¹ technique for example, films could be built up chain-by-chain with no inter-chain entanglements. Studying both the glass transition and the rheology of such a film may provide some answers as to how the two length scales are connected and why a decrease in the glass transition temperature is observed.

Magnitude of residual stress in thin films

In chapter 5 the feasibility of using focused ion beam milling to study the overall magnitude of the stresses in as-cast films was investigated. Cantilevers were cut into PS films spun-cast onto low stress silicon nitride membranes. On completion of the milling the cantilevers were observed to bend upwards. By modelling the cantilever as a plate, the stresses in the polymer film were calculated from the deflection of the cantilever. For as spun films the stress was measured to be 211 MPa, with a reduction being observed for films aged at room temperature.

While this chapter shows the feasibility of this method for measuring the magnitude of stored stresses in polymer films, the results seem to contradict those of chapter 4. For the cantilever to bend, the film must be in a state of tensile stress. Such a stress should drive instability formation, resulting in a smaller wavelength of insta-

¹Langmuir-Blodgett films are deposited monolayer by monolayer and are normally formed from amphiphilic molecules with a hydrophilic head and a hydrophobic tail e.g. fatty acids.

bility forming with a faster onset time. This is opposite to the behaviour observed in chapter 4.

The combination of these results and those in chapter 4 therefore suggest that the stress distribution within the film is more complex than a simple uniform in-plane stress or frozen-in normal stress. The nature of the stresses in as-cast polymer films is thus not yet fully understood.

Magnetic thin films

In chapter 6 the magnetic properties of ceramic films pyrolysed from palladium doped polyferrocenylethylmethylsilane (PFEMS) were investigated. The palladium was added in nanoparticle form and through directly mixing palladium acetylacetonate with the polymer prior to film deposition. The polymer precursors were all seen to exhibit paramagnetic behaviour. Increasing magnetic susceptibility was observed with palladium content. Pyrolysis of the polymer precursors resulted in the formation of ferromagnetic ceramics. The magnetic behaviour was seen to depend on the temperature and atmosphere used for pyrolysis. Pyrolysis of the palladium containing precursors under argon at 1000 °C, resulted in the formation of ceramics containing FePd alloys. These ceramics had an enhanced coercivity, remanent magnetisation and saturation magnetisation.

The formation of FePd alloys is highly desirable due to their application in data storage technologies. Metal alloy nanoparticles and films are normally prepared using methods such as sputter deposition under ultra high vacuum, electrodeposition and chemical vapour deposition. All of these methods require specialist equipment, can be costly and are time consuming. Here the incorporation of palladium into the iron-containing PFEMS, allows for FePd containing ceramics to be formed. This would enable iron-palladium containing ceramics to be produced quickly and cheaply in a one step process.

To be relevant for data storage technologies, structured films are required with

Physical phenomena of thin surface layers

feature sizes on the order of 50 nm. Iron-containing polymers have previously been structured on the nanoscale using an imprint method. This pattern is retained on pyrolysis. Future work will focus on using similar methods to pattern the palladium doped PFEMS. This would allow a regular array of ceramic pillars to be formed with the required properties, providing an alternative to current data storage technologies.

Iridescent thin films

Finally, in chapter 7 the bright blue colouration observed on the leaf of the tropical fern *Selaginella willdenowii* was studied. This fern grows in the understorey of the rainforest where the light intensity is less than 1% of that at the canopy. The blue colouration is shown to be iridescent in nature, with a peak in the reflectance spectra for the juvenile blue leaves being observed at around 430 nm for an angle of incidence of 16°. This peak shifts to lower wavelengths as the angle of incidence is increased and is not observed in more mature green leaves.

Transmission electron microscopy studies confirm the presence of a layered lamellar thin film structure on the upper cuticle of the iridescent leaves. These thin film multilayers were modelled using literature values for the refractive indices of the plant cell cytoplasm and cuticular wax, showing that they are responsible for the iridescence observed. Blue and green leaves from the same plant were compared. The loss of the blue iridescence corresponds to a loss of the multilayer structures.

It had previously been postulated that the iridescence in these plants might act to enhance light capture of photosynthetically important wavelengths. The results in chapter 7 do not support this hypothesis. The reflectance of light in the range of 600–700 nm is the same for both the iridescent and non-iridescent leaves. Blue iridescence is not confined to *Selaginella willdenowii*, but is observed in a wide variety of shade dwelling photosynthetic organisms. As a result it is likely that the iridescence has some other adaptive benefit. While some possibilities are discussed in chapter 7, further investigations are required before any conclusions, on the role of iridescence,

in these plants can be made. Insight into the role of the iridescence could be achieved through identification of the genes that control production of the iridescence. So far identification of these genes, in both plants and animals, has eluded biologists. If the genes could be found and implanted into non-iridescent species, direct comparison of iridescent and non-iridescent plants could be carried out. It would also allow for some pretty cool plants to be grown!

BIBLIOGRAPHY

- [1] M Geoghegan and G Krausch. Wetting at polymer surfaces and interfaces. *Prog. Polym. Sci.*, 28(2):261–302, 2003.
- [2] F Bruder and R Brenn. Spinodal decomposition in thin films of a polymer blend. *Phys. Rev. Lett.*, 69(4):624–627, 1992.
- [3] H Wang and J Composto. Thin film polymer blends undergoing phase separation and wetting: Identification of early, intermediate and later stages. *J. Chem. Phys.*, 113(22):10386–10397, 2000.
- [4] QS Bhatia, DP Pan, and JT Koberstein. Preferential surface adsorption in miscible blends of polystyrene and poly(vinyl methyl ether). *Macromolecules*, 21:2166–2175, 1988.
- [5] E Schäffer, T Thurn-Albrecht, TP Russell, and U Steiner. Electrically induced structure formation and pattern transfer. *Nature*, 403:874–877, 2000.
- [6] ZQ Lin, T Lerle, TP Russell, E Schaffer, and U Steiner. Structure formation at the liquid/liquid bilayer in electric fields. *Macromolecules*, 35:3971–3976, 2002.
- [7] D Barbero and U Steiner. Nonequilibrium polymer rheology in spin-cast films. *Phys. Rev. Lett.*, 102:248303, 2009.
- [8] MJ MacLachlan, M Ginzburg, N Coombs, TW Coyle, NP Raju, JE Greeden, GA Ozin, and Manners I. Shaped ceramics with tunable magnetic properties from metal-containing polymers. *Science*, 287:1460–1463, 2000.
- [9] P Vukusic and R Sambles. Photonic structures in biology. *Nature*, 424:852–855, 2003.
- [10] PJ Flory. Thermodynamics of high polymer solutions. *J. Chem. Phys.*, 10:51–61, 1942.

- [11] ML Huggins. Some properties of solutions of long-chain compounds. *J. Chem. Phys.*, 146:1942, 151-158.
- [12] XF Gong, KS Shing, and WV Chang. Effect of composition dependent flory interaction parameter χ on polymer adsorption theory. *Polym. Bull.*, 22:71–78, 1989.
- [13] J Eckelt, R Sugaya, and BA Wolf. Pullulan and dextran: Uncommon composition dependent flory-huggins interaction parameters of their aqueous solutions. *Biomacromolecules*, 9:1691–1697, 2008.
- [14] S Qian, SJ Mumby, and BE Eichinger. Phase diagrams of binary polymer solutions and blends. *Macromolecules*, 24:1655–1661, 1991.
- [15] M Rubenstein and RH Colby. *Polymer Physics*. Oxford University Press, Oxford, 2006.
- [16] E Schäffer, S Harkema, M Roerdink, R Blossey, and U Steiner. Morphological instability of a confined polymer film in a thermal gradient. *Macromolecules*, 36:1645–1655, 2003.
- [17] M Nedelcu, MD Morariu, D Harkema, NE Voicu, and U Steiner. Pattern formation by temperature-gradient driven film instabilities in lateral geometries. *Soft Matter*, 1:62–65, 2005.
- [18] A Oron, SH Davis, and SG Bankoff. Long-scale evolution of thin liquid films. *Rev. Mod. Phys.*, 69(3):931–980, 2002.
- [19] R Seeman, S Herminghaus, C Neto, S Schlagowski, D Podzimek, R Konrad, H Mantz, and K Jacobs. Dynamics and structure formation in thin polymer melt films. *J. Phys.-Condes. Matter*, 17(9):S267–S290, 2005.
- [20] MB Williams and SH Davis. Nonlinear theory of film rupture. *J. Colloid Interface Sci.*, 90(1):220–228, 1982.
- [21] G Reiter. Dewetting of thin polymer-films. *Phys. Rev. Lett.*, 68(1):75–78, 1992.
- [22] G Reiter. Unstable thin polymer films: Rupture and dewetting processes. *Langmuir*, 9(9):1344–1351, 1993.
- [23] A Pototsky, Bestehorn. M, D Merkt, and U Thiele. Evolution of interface patterns of three-dimensional two-layer liquid films. *Europhys. Lett.*, 74(4):665–671, 2006.

-
- [24] A Sharma and J Mittal. Instability of thin liquid films by density variations: A new mechanism that mimics spinodal dewetting. *Phys. Rev. Lett.*, 89(18):186101, 2002.
- [25] E Schäffer. *Instabilities of thin polymer films: structure formation and pattern transfer*. PhD thesis, Universität Konstanz, 2001.
- [26] F London. Zur theorie und systematik der molekularkräfte. *Z Phys.*, 63:245–279, 1930.
- [27] R Seeman, S Herminghaus, and K Jacobs. Dewetting patterns and molecular forces: A reconciliation. *Phys. Rev. Lett.*, 86:5534–5537, 2001.
- [28] J Israelachvili. *Intermolecular and Surface Forces*. Academic Press,, London, 1991.
- [29] R Yerushalami-Rozen, T Kerle, and J Klein. Alternative dewetting pathways of thin liquid films. *Science*, 285:1254–1255, 1999.
- [30] S Madruga and U Thiele. Decomposition driven interface evolution for layers of binary mixtures. ii. influence of connective transport on linear stability. *Phys. Fluids*, 21:062104, 2009.
- [31] VI Kovalchuk, H Kamusewitz, D Vollhardt, and NM Kovalchuk. Auto-oscillation of surface tension. *Phys. Rev. E*, 60(2):2029–2036, 1999.
- [32] U Thiele, S Madruga, and L Frastia. Decomposition driven interface evolution for layers of binary mixtures. i. model derivation and stratified base states. *Phys. Fluids*, 19:122106, 2007.
- [33] N Clarke. Instabilities in thin-film binary mixtures. *Eur. Phys. J. E*, 14(3):207–210, 2004.
- [34] N Clarke. Toward a model for pattern formation in ultra-thin binary mixtures. *Macromolecules*, 38(16):6775–6778, 2005.
- [35] MD Morariu, NE Voicu, E Schaffer, Z Lin, TP Russell, and U Steiner. Heirarchical structure formation and pattern replication induced by an electric field. *Nat. Mater.*, 2:48–52, 2003.
- [36] P Goldberg-Oppenheimer and U Steiner. Rapid electrohydrodynamic lithography using low-viscosity polymers. *Small*, 6(11):1248–1254, 2010.

- [37] JW Swan. Stress and other effects produced in resin and in a viscid compound of resin and oil by electrification. *P. Roy. Soc. London*, 62:38–46, 1897.
- [38] A Onuki. Interface instability induced by an electric field in fluids. *Physica A*, 217:38–52, 1995.
- [39] S Herminghaus. Dynamical instability of thin liquid films between conducting media. *Phys. Rev. Lett.*, 83(12):2359–2361, 1999.
- [40] LF Pease and WB Russel. Limitations on length scales for electrostatically induced submicrometer pillars and holes. *Langmuir*, 20:795–804, 2004.
- [41] X Li, L Wu, P Deshpande, Z Yu, W Wu, H Ge, and SY Chou. 100nm period gratings produced by lithographically induced self-construction. *Nanotechnology*, 14:786–790, 2003.
- [42] P Deshpande, LF Pease III, L Chen, SY Chou, and WB Russel. Cylindrically symmetric electrohydrodynamic patterning. *Phys. Rev. E*, 70:041601, 2004.
- [43] NE Voicu, S Harkema, and U Steiner. Electric-field-induced pattern morphologies in thin liquid films. *Adv. Funct. Mater.*, 16:926–934, 2006.
- [44] U Steiner. Force measurements using capillary instabilities. *J. Polym. Sci. Pol. Phys.*, 43(23):3395–3405, 2005.
- [45] U Steiner. *Nanoscale assembly. Chemical techniques*. Springer, 2005.
- [46] U Steiner and J Klein. Growth of wetting layers from liquid mixtures. *Phys. Rev. Lett.*, 77(12):2536–2529, 1996.
- [47] U Steiner, J Klein, E Eiser, A Budkowski, and LJ Fetter. Complete wetting from polymer mixtures. *Science*, 258(5085):1126–1129, 1992.
- [48] JMG Cowie, BG Devlin, and IJ McEwan. Surface enrichment in ps/pvme blends: 2. the effect of specific interaction in the bulk mixture. *Polymer*, 34(19):4130–4135, 1993.
- [49] PG deGennes. Wetting: statics and dynamics. *Rev. Mod. Phys.*, 57(3):827–863, 1985.
- [50] PG deGennes. *Scaling concepts in polymer physics*. Cornell University Press, Ithaca, 1979.

-
- [51] J Genzer and RJ Composto. Surface segregation and amplification in miscible blends near criticality. *Europhys. Lett.*, 38(3):171–176, 1997.
- [52] MD Morariu, E Schäffer, and U Steiner. Capillary instabilities by fluctuation induced forces. *Eur. Phys. J. E*, 12(3):375–381, 2003.
- [53] J You, Y Liao, X Li, Z Su, and L An. Temperature dependence of surface composition and morphology in polymer blend film. *Polymer*, 49:4456–4461, 2008.
- [54] RAL Jones, LJ Norton, EJ Kramer, FS Bates, and P Wiltzius. Surface-directed spinodal decomposition. *Phys. Rev. Lett.*, 66(10):1326–1329, 1991.
- [55] HP Fischer, P Maass, and W Dieterich. Diverging time and length scales of spinodal decomposition modes in thin films. *Europhys. Lett.*, 42(1):49–54, 1998.
- [56] HP Fischer, P Maass, and W Dieterich. Novel surface modes in spinodal decomposition. *Phys. Rev. Lett.*, 79(5):893–896, 1997.
- [57] Y Nishi and TK Kwei. Cloud point curves for poly(vinyl methyl ether) and monodisperse polystyrene mixtures. *Polymer*, 16:285–290, 1975.
- [58] T Shiomi. Thermodynamics of polymer blends of poly(vinyl methyl ether) and polystyrene. *Macromolecules*, 23:229–233, 1990.
- [59] K El-Mabrouk. Assessment of morphology in transient and steady state regimes resulting from phase separation in polystyrene/poly(vinyl methyl ether). *Rheol. Acta.*, 45:877–889, 2006.
- [60] A Ajji, L Choplin, and RE Prudhomme. Rheology of polystyrene poly(vinyl methyl ether) blends near the phase transition. *J. Poly. Sci. B: Poly. Phys.*, 29(13):1573–1578, 1991.
- [61] MB Djordjevic and PS Porter. C-13 nmr characterisation of intermolecular interactions for polymers. *Poly. Eng. Sci.*, 22:1109–1116, 1982.
- [62] PA Mirau and JL White. Solid state nmr studies of intermolecular interactions in solid polymer blends. *Magn. Reson. Chem.*, 32:S23–S29, 1994.
- [63] B Reidl and RE Prudhomme. Temperature dependence of the interaction parameter between n-heptane, carbon-tetrachloride and benzene and poly(vinyl methyl ether) between 120c and 180c. *J. Poly. Sci. B*, 28:2411–2420, 1990.

- [64] M Bank, J Leffingwell, and C Thies. The influence of solvent upon the compatibility of polystyrene and poly(vinyl methyl ether). *Macromolecules*, 4(1):43–46, 1971.
- [65] CC Han, BJ Bauer, JC Clark, Y Muroga, Y Matsushuta, M Okada, Q Tran-cong, and T Chang. Temperature, composition and molecular weight dependence of the binary interaction parameter of polystyrene/poly(vinyl methyl ether) blends. *Polymer*, 29:2002–2014, 1988.
- [66] El-Mabrouk. K and M Bousmina. Effect of molecular weight and shear on phase diagram of ps/pvme blend. *Rheol. Acta.*, 45:959–969, 2006.
- [67] K El-Mabrouk, M Belaiche, and M Bousmia. Phase separation in ps/pvme thin and thick films. *J. Colloid Interf. Sci.*, 306(2):354–367, 2007.
- [68] RM Briber and BJ Bauer. Effect of cross-links on the phase separation behaviour of a miscible polymer blend. *Macromolecules*, 21:3296–3303, 1988.
- [69] C Forrey, JT Koberstein, and DH Pan. Surface segregation in miscible blends of polystyrene and poly(vinyl methyl ether): Comparison of theory and experiment. *Interface Sci.*, 11:211–223, 2003.
- [70] DH Pan and WM Prest. Surface of polymer blends: x-ray photoelectron-spectroscopy studies of polystyrene/ poly(vinyl methyl ether) blends. *J. Appl. Phys.*, 58(8):2861–2870, 1985.
- [71] D Wang and H Ishida. Surface microscale semi-heterogeneous structures in compatible polystyrene and poly(vinyl methyl ether) blend thin films investigated by lateral-force microscopy. *Macromol. Chem. Physic.*, 208(19-20):2222–2228, 2007.
- [72] H Wang and RJ Composto. Wetting and phase separation in polymer blend films: Identification of four thickness regimes with distinct morphological pathways. *Interface Sci.*, 11(11):237–248, 2003.
- [73] T Nishi, TT Wang, and TK Kwei. Thermally induced phase separation behaviour of compatible polymer mixtures. *Macromolecules*, 8(2):227–234, 1975.
- [74] H Ogawa, T Kanaya, and G Matsuba. Composition fluctuations before dewetting in polystyrene/ poly(vinyl methyl ether) blend thin films. *Polymer*, 49:2553–2559, 2008.

-
- [75] T Wagler, PL Rinaldi, CD Han, and H Chun. Phase behaviour and segmental mobility in binary blends of polystyrene and poly(vinyl methyl ether). *Macromolecules*, 33:1778–1789, 2000.
- [76] A Asano, K Takegoshi, and K Hikichi. C-13 cp/mass nmr-study on the miscibility and phase-separation of a polystyrene poly(vinyl methyl ether) blend. *Macromolecules*, 35(26):5630–5636, 1994.
- [77] K Takegoshi and K Hikichi. Effects of blending on local chain dynamics and glass transition: polystyrene/ poly(vinyl methyl ether) blends as studied by high-resolution solid-state ¹³c nuclear magnetic resonance spectroscopy. *J. Chem. Phys.*, 94(4):3200–3206, 1991.
- [78] TK Kwei, T Nichi, and RF Roberts. A study of compatible polymer mixtures. *Macromolecules*, 7(5):667–674, 1974.
- [79] K Schmidt-Rohr, J Clauss, and HW Spiess. Correlation of structure, mobility and morphological information in heterogeneous polymer materials by two-dimensional wideline-separation nmr spectroscopy. *Macromolecules*, 25(12):3273–3277, 1992.
- [80] R Brown, editor. *Handbook of polymer testing*. Marcel Dekker Inc., New York, 1999.
- [81] P Duckworth, H Richardson, C Carelli, and JL Keddie. Infrared ellipsometry of interdiffusion in thin films of miscible polymers. *Surf. Inter. Anal.*, 36:33–41, 2004.
- [82] K Hinrichs, M Gensch, N Nikonenko, J Pionteck, and KJ Eichhorn. Spectroscopic ellipsometry for characterization of thin films of polymer blends. *Macromol. Symp.*, 230:26–32, 2005.
- [83] BB Sauer and DJ Walsh. Use of neutron reflection and spectroscopic ellipsometry for the study of the interface between miscible polymer blends. *Macromolecules*, 24(22):5948–5955, 1991.
- [84] TP Russell. The characterization of polymer interfaces. *Annu. Rev. Mater. Sci.*, 21:249–268, 1991.
- [85] JE Mark, editor. *Polymer Data Handbook*. Oxford University Press, online edition, 1999.

- [86] J Brandrup, EH Immergrut, and EA Grulke, editors. *Polymer Handbook*, volume 1 and 2 of *New Jersey*. Wiley-Interscience, fourth edition, 1999.
- [87] DE Aspnes. Local-field effects and effective-medium theory: A microscopic perspective. *Am. J. Phys.*, 50:8, 1982.
- [88] RP Feynman, RB Leighton, and M Sands. *The Feynman Lectures on Physics*, volume 2. Addison-Wesley Publishing Company, Reading, MA, 1965.
- [89] DAG Bruggeman. Calculation of various physics constants in heterogeneous substances 1. dielectric constants and conductivity of mixed bodies from isotropic substances. *Ann. Physik*, 416(8):665–679, 1935.
- [90] R Gelles and CW Frank. Phase separation in polystyrene/poly(vinyl methyl ether) blends as studied by excimer fluorescence. *Macromolecules*, 15:1486–1491, 1982.
- [91] RAL Jones and RW Richards. *Polymers at Surfaces and Interfaces*. Cambridge University Press, Cambridge, 1999.
- [92] M Shibayama, H Yang, RS Stein, and CC Han. Study of the miscibility and critical phenomena of deuterated polystyrene and hydrogenated poly(vinyl methyl ether) by small angle neutron scattering. *Macromolecules*, 18:2179–2187, 1985.
- [93] RAL Jones, EJ Kramer, MH Rafailovich, J Sokolov, and SA Schwarz. Surface enrichment in an isotropic polymer blend. *Phys. Rev. Lett.*, 62(3):280–283, 1989.
- [94] T Gal. Functional differentiation under conservation constraints. *J. Phys. A: Math, Gen.*, 35:5899–5905, 2005.
- [95] T Gal. Differentiation of functionals with variables coupled by conservation constraints: Analysis through a fluid-dynamical model. *J. Math. Phys.*, 48:053520, 2007.
- [96] SF Edwards. *Proc. Phys. Soc.*, 88(2):365–280, 1966.
- [97] M Souche and N Clarke. Phase equilibria in polymer blend thin films: A hamiltonian approach. *J. Chem. Phys.*, 131:244903, 2009.
- [98] JL Keddie, RAL Jones, and RA Cory. Size-dependent depression of the glass transition temperature in polymer films. *Europhys. Lett.*, 27(1):59–64, 1994.

-
- [99] T Miyazaki, K Nishida, and T Kanaya. Contraction and reexpansion of polymer thin films. *Phys. Rev. E*, 69:022801, 2004.
- [100] M Mukherjee, M Bhattacharya, MK Sanyal, Th Geue, J Grenzer, and U Pietsch. Reversible negative thermal expansion of polymer films. *Phys. Rev. E*, 66:061801, 2002.
- [101] J-L Masson and PF Green. Viscosity of entangled polystyrene thin film melts: film thickness dependence. *Phys. Rev. E*, 65:031806, 2002.
- [102] RL Jones, SK Kumar, DL Ho, RM Briber, and TP Russell. Chain conformation in ultrathin polymer films. *Nature*, 400:146–149, 1999.
- [103] H Kim, A Rühm, LB Lurio, JK Basu, J Lal, SGJ Mochrie, and SK Sinha. Synchrotron radiation studies of the dynamics of polymer films. *J. Phys. Condens. Matter*, 16:S3491–S3497, 2004.
- [104] H Kim, A Rühm, LB Lurio, JK Basu, J Lal, D Lumma, SGJ Mochrie, and SK Sinha. Surface dynamics of polymer films. *Phys. Rev. Lett.*, 90(6):068302, 2003.
- [105] G Reiter, S Al Akhrass, M Hamieh, P Damman, S Gabriele, T Vilmin, and E Raphaël. Dewetting as an investigative tool for studying properties of thin polymer films. *Eur. Phys. J. Special Topics*, 166:165–172, 2009.
- [106] G Reiter, M Hamieh, P Damman, S Sclavons, S Gabriele, T Vilmin, and E Raphaël. Residual stresses in thin polymer films cause rupture and dominate early stages of dewetting. *Nat. Mater.*, 4:754–758, 2005.
- [107] P Damman, S Gabriele, S Coppee, S Desprez, D Villier, T Vilmin, E Raphaël, M Hamieh, S Al Akhrass, and G Reiter. Relaxation of residual stress and reentanglement of polymers in spin-coated films. *Phys. Rev. Lett.*, 99:036101, 2007.
- [108] T Vilmin and E Raphaël. Dewetting of thin polymer films. *Eur. Phys. J. E*, 21:161–174, 2006.
- [109] Z Yang, C-H Lam, E DiMasi, N Bouet, J Jordon-Sweet, and OKC Tsui. Method to measure the viscosity of nanometer liquid films from surface fluctuations. *App. Phys. Lett.*, 94:251906, 2009.
- [110] D Barbero. *Study of the rheology of thin liquid films - novel flexible molds for nanoimprinting*. PhD thesis, University of Cambridge, 2009.

- [111] OKC Tsui, YJ Wang, FK Lee, C-H Lam, and Z Yang. Equilibrium pathway of spin-coated polymer films. *Macromolecules*, 41:1465–1468, 2008.
- [112] JH Park and E Kim. Effect of electric-field assisted thermal annealing of poly(4-vinylphenol) film on its dielectric constant. *App. Phys. Lett.*, 92(10):103311, 2008.
- [113] TG Fox and PJ Flory. Second order transition temperatures and related properties of polystyrene. 1. influence of molecular weight. *J. Appl. Phys.*, 21:581–591, 1950.
- [114] EM Meyer, H Hug, and R Bennewitz. *Scanning probe microscopy: The lab on a tip*. Springer-Verlag., Berlin, 2003.
- [115] JC Moreira and NR Demarquette. Influence of temperature, molecular weight and molecular weight dispersity on the surface tension of ps, pp and pe. 1. experimental. *J. Appl. Polym. Sci.*, 82(8):1907–1920, 2001.
- [116] T Vilmin and E Raphaël. Dynamic instability of thin viscoelastic films under lateral stress. *Phys. Rev. Lett.*, 97:036105, 2006.
- [117] A Bach, K Almdal, HK Rasmussen, and O Hassanger. Elongational viscosity of narrow molar mass distribution polystyrene. *Macromolecules*, 36:5174–5179, 2003.
- [118] S-T Sun, I Nishio, G Swislow, and T Tanaka. The coil-globule transition: Radius of gyration of polystyrene in cyclohexane. *J. Chem. Phys.*, 73(12):5971–5875, 1980.
- [119] M Daoud and G Jannink. Temperature-concentration diagram of polymer solutions. *J. Phys-Paris*, 37:973–979, 1976.
- [120] SH Maron and CA Daniels. Thermodynamics of polystyrene solutions 1. interaction parameters and polymer order. *J. Macr. Science Part B*, 2(4):743–767, 1968.
- [121] SR Quake. Topological effects of knots in polymers. *Phys. Rev. Lett.*, 73(24):3317–3320, 1994.
- [122] Q Zhou and RG Larson. Direct molecular dynamics simulation of branch point motion in asymmetric star polymer melts. *Macromolecules*, 40:3443–3449, 2007.

-
- [123] Y Zhang, Q Ren, and Y Zhao. Modelling analysis of surface stress on a rectangular cantilever beam. *J. Phys. D: Appl. Phys.*, 37:2140–2145, 2004.
- [124] W Fang and JA Wickert. Determining mean and gradient residual stresses in thin films using micromachined cantilevers. *J. Micromech. Microeng.*, 6:301–309, 1996.
- [125] GG Stoney. The tension of metallic films deposited by electrolysis. *Proc. R. Soc. Lond. A*, 82:172–175, 1909.
- [126] M Ree, S Swanson, and W Volksen. Effect of precursor history on residual stress and relaxation behaviour of high temperature polyimides. *Polymer*, 34(7):1423–1430, 1993.
- [127] SG Croll. Internal stress in a solvent-cast thermoplastic coating. *J. Coating Technol.*, 50(638):33–38, 1978.
- [128] SG Croll. The origin of residual internal stress in solvent-cast thermoplastic coatings. *J. Appl. Polym. Sci.*, 23:847–858, 1979.
- [129] JW Judy. Microelectromechanical systems (mems):fabrication, design and applications. *Smart. Mater. Struct.*, 10:1115–1134, 2001.
- [130] AM Korsunsky, M Sebastiani, and E Bemporad. Focused ion beam ring drilling for residual stress evaluation. *Mater. Lett.*, 63:1961–1963, 2009.
- [131] N Sabate, D Vogel, A Gollhardt, J Keller, C Cane, I Gracia, JR Morante, and B Michel. Measurement of residual stress by slot milling with focused ion-beam equipment. *J. Micromech. Microeng.*, 16:254–259, 2006.
- [132] S Reyntjens and R Puers. A review of focused ion beam applications in microsystems technology. *J. Micromech. Microeng.*, 11:287–300, 2001.
- [133] EM Corcoran. Determining stresses in organic coatings using plate beam deflection. *J. Paint Technol.*, 41:635–640, 1969.
- [134] TS Chow, CA Liu, and RC Penwell. Strains induced upon drying thin films solvent-cast on flexible substrates. *J. Polym. Sci. Pol. Phys.*, 14:1311–1316, 1976.
- [135] Z Rongjing. *Mechanical characterisation of thin films with application to ferroelectrics*. PhD thesis, California institute of technology, 2006.

- [136] BA Walmsley, Y Liu, ZH Zhi, MB Bush, JM Dell, and L Farone. Poisson's ratio of low-temperature pecvd silicon nitride thin films. *J. Microelectromech. S.*, 16:622–627, 3 2007.
- [137] JY Chung, Q Chastek, MJ Fasolka, HW Ro, and CM Stafford. Quantifying residual stress in nanoscale thin polymer films via surface wrinkling. *ACS Nano*, 3:844–852, 4 2009.
- [138] RA Shalliker, PE Kavanagh, IM Russell, and Hawthorne. The measurement of molecular weight distribution of some polydisperse polystyrene by reversed phase and size exclusion chromatography. *Chromatographia*, 33:427–433, 1992.
- [139] RD Mathad, HGH Kumar, B Sannakki, S Ganesh, KSS Sarma, and MV Badiger. High energy electron irradiation effects on polystyrene films. *Radiat. Eff. Defect. S.*, 164:656–664, 10 2009.
- [140] RDA Hudson. Ferrocene polymers: current architectures, syntheses and utility. *J. Organometallic Chemistry*, 637:47–69, 2001.
- [141] BW Rockett and G Marr. Ferrocene: Annual survey covering the year 1977. *J. Organometallic Chemistry*, 167:51–134, 1979.
- [142] KJ Wynne and RW Rice. Ceramics via polymer pyrolysis. *Ann. Rev. Mater. Sci.*, 14:297–334, 1984.
- [143] AS Abd-El-Aziz and EK Todd. Organoiron polymers. *Coord. Chem. Rev.*, 246:3–52, 2003.
- [144] TJ Kealy and PL Paulson. A new type of organo-iron compound. *Nature*, 168:1039–1040, 1951.
- [145] I Manners. Putting metals into polymers. *Science*, 294:1665–1667, 2001.
- [146] PD Pomogalio. *Catalysis by polymer immobilized metal complexes*. Gordon and Breach Science Publishers, Amsterdam, 1998.
- [147] RP Kingsborough and TM Swager. Transition metals in polymeric π -conjugated organic frameworks. *Prog. Inorg. Chem.*, 48:123, 1999.
- [148] JA Massey, MA Winnik, and I Manners. Fabrications of oriented nanoscopic ceramic lines from cylindrical micelles of an organometallic polyferrocene block copolymer. *J. Am. Chem. Soc.*, 123(13):3147–3148, 2001.

- [149] V Bellas and M Rehahn. Polyferrocenylsilane-based polymer systems. *Angew. Chem. Int. Ed.*, 46:5082–5104, 2007.
- [150] DE Herbert, UFJ Mayer, and I Manners. Strained metallocenophanes and related organometallic rings containing pi-hydrocarbon ligands and transition-metal centers. *Angew. Chem. Int. Ed.*, 46(27):5060–5081, 2007.
- [151] B-Z Tang, R Petersen, DA Foucher, A Lough, N Coombs, R Sodhi, and I Manners. Novel ceramic and organometallic depolymerisation products from poly(ferrocenylsilanes) via pyrolysis. *J. Chem. Soc. Chem. Commun.*, pages 523–525, 1993.
- [152] P Petersen, DA Foucher, B-Z Tang, A Lough, NP Raju, JE Greedan, and I Manners. Pyrolysis of poly(ferrocenylsilanes): Synthesis and characterization of ferromagnetic transition metal-containing ceramics and molecular depolymerisation products. *Chem. Mater.*, 7:2045–2053, 1995.
- [153] M Ginzburg, MJ MachLachlan, SM Yang, N Coombs, TW Coyle, NP Raju, JE Greeden, RH Herber, GA Ozin, and I Manners. Genesis of nanostructured, magnetically tunable ceramics, from the pyrolysis of cross-linked polyferrocenylsilane networks and formation of shaped macroscopic objects and micron scale patterns by micromolding inside silicon wafers. *J. Am. Chem. Soc.*, 124(11):2625–2639, 2002.
- [154] K Kulbaba, A Cheng, A Bartole, S Greenberg, R Resendes, N Coombs, S Safa-Sefat, JE Greeden, HDH Stover, GA Ozin, and I Manners. Polyferrocenylsilane microspheres: Synthesis, mechanism of formation, size change tunability, electrostatic self-assembly and pyrolysis to spherical magnetic ceramic particles. *J. Am. Chem. Soc.*, 124:12522–12534, 2002.
- [155] Q Sun, JWY Lam, K Xu, H Xu, JAK Cha, PCL Wong, G Wen, X Zhang, X Jing, F Wang, and BZ Tang. Nanocluster-containing mesoporous magnetoceramics from hyperbranched organometallic polymer precursors. *Chem. Mater.*, 12:2617–2624, 2000.
- [156] D Chung. *Carbon*, 39:379, 2001.
- [157] K Kulbaba and I Manners. Polyferrocenylsilanes: Metal-containing polymers for materials science, self-assembly and nanostructure applications. *Macro. Rap. Comm.*, 22(10):711–724, 2001.

- [158] C-L Liu, Kand Ho, S Aouba, Y-Q Zhao, Z-H Lu, Si Petroc, N Coombs, P Dube, H E. Ruda, W-Y Wong, and I Manners. Synthesis and lithographic patterning of FePt nanoparticles using a bimetallic metallopolyyne precursor. *Angew. Chem.-Int. Edit.*, 47(7):1255–1259, 2008.
- [159] K Liu, SB Clendenning, L Friebe, WY Chan, X Zhu, MR Freeman, GC Yang, CM Yip, D Grozea, ZH Lu, and I Manners. Pyrolysis of highly metatalized polymers: ceramic thin films containing magnetic coFe alloy nanoparticles from a polyferrocenylsilane with pendant cobalt clusters. *Chem. Mater.*, 18:2591–2601, 2006.
- [160] L Friebe, K Liu, B Obermeier, S Petrov, P Dube, and I Manners. Pyrolysis of polycarbosilanes with pendant nickel clusters: synthesis and characterisation of magnetic ceramics containing nickel and nickel silicide nanoparticles. *Chem. Mater.*, 19(10):2630–2640, 2007.
- [161] GJ Nieuwenhuys. Magnetic behavior of cobalt, iron and manganese dissolved in palladium. *Adv. Phys.*, 24(4):515–591, 1975.
- [162] H Naganuma, K Sato, and Y Hirotsu. Particle size dependence of atomic ordering and magnetic properties of FePt nanoparticles. *J. Magn. Magn. Mater.*, 310:2356–2358, 2007.
- [163] ME Gruner and A Dannenberg. Structure and magnetism of near-stoichiometric FePt nanoparticles. *J. Magn. Magn. Mater.*, 321(7):861–864, 2009.
- [164] D Weller and MF Doerner. Extremely high-density longitudinal magnetic recording media. *Annu. Rev. Mater. Sci.*, 30:611–644, 2000.
- [165] DA Rider, KA Cavicchi, KN Power-Billard, TP Russell, and I Manners. Diblock copolymers with amorphous atactic polyferrocenylsilane blocks: Synthesis, characterization, and self-assembly of polystyrene-block-poly(ferrocenylethylmethylsilane) in the bulk state. *Macromolecules*, 38:6931–6938, 2005.
- [166] S Horiuchi, MI Sarwar, and Y Nakao. Nanoscale assembly of metal clusters in block copolymer films with vapor of a metal-acetylacetonato complex using a dry process. *Adv. Mater.*, 12(20):1507–1511, 2000.
- [167] RL Fagaly. Superconducting quantum interference device instruments and applications. *Rev. Sci. Instrum.*, 77:101101, 2006.

-
- [168] D Cohen. Magnetoencephalography: Detection of the brain's electrical activity with a superconducting magnetometer. *Science*, 175:664–666, 1972.
- [169] J Clarke. Geophysical applications of squids. *IEEE trans. magn.*, 19(3):288–294, 1972.
- [170] H Weinstock, editor. *SQUID sensors: Fundamentals, Fabrication and Applications*, volume 329 of *Series E: Applied Sciences*. Kluwer Academic Publishers, 1995.
- [171] C Hammond. *The basics of crystallography and diffraction*. Oxford Science Publications, New York, 1997.
- [172] S Lee, H Younan, Z Siping, and M Zhiqiang. Studies on electron penetration versus beam acceleration voltage in dispersive x-ray molecules. pages 610–613, Kuala Lumpur, Malaysia, 2006. ICSE2006 Proc.
- [173] DA Rider, K Liu, J-C Eloi, L Vanderark, L Tang, J-Y Wang, D Grozea, Z-H Lu, TP Russell, and I Manners. Nanostructured magnetic thin films from organometallic block copolymers: Pyrolysis of self-assembled polystyrene-block-poly(ferrocenylethylmethylsilane). *ACS Nano*, 2(2):263–270, 2008.
- [174] V Cominos and A Gavriilidis. Sublimation and deposition behaviour of palladium (ii) acetylacetonate. *Eur. Phys. J. Appl. Phys*, 15:25–33, 2001.
- [175] A Guinier. *X-Ray Diffraction in crystals, imperfect crystals and amorphous bodies*. General Publishing Company, Toronto, Canada, 1994.
- [176] KJ Bryden and YY Jackie. Electrodeposition synthesis and hydrogen absorption properties of nanostructures palladium-iron alloys. *Nanestruc. Mater.*, 9:485–488, 1997.
- [177] W Li and P Haldar. Supportless pdfe nanorods as highly active electrocatalyst for proton exchange membrane fuel cell. *Electrochem. Commun.*, 11:1195–1198, 2009.
- [178] WH Meiklejohn and CP Bean. New magnetic anisotropy. *Phys. Rev.*, 102:1413, 1956.
- [179] I Dzyaloshinsky. A thermodynamic theory of weak ferromagnetism of antiferromagnets. *J. Phys. Chem. Solids*, 4:241, 1958.

- [180] O Crisan, K von Haeften, AM Ellis, and C Binns. Structure and magnetic properties of Fe/Fe oxide clusters. *J. Nanopart. Res.*, 10:193–199, 2008.
- [181] E Zhang, Y Tang, K Peng, C Guo, and Y Zhang. Synthesis and magnetic properties of γ -Fe₂O₃/SiO₂ core-shell nanoparticles under hydrothermal conditions. *Solid State Commun.*, 148:496–500, 2008.
- [182] LE Wenger, GM Tsoi, PP Vaishnava, U Senaratne, EC Buc, R Naik, and VM Naik. Magnetic properties of γ -Fe₂O₃ nanoparticles precipitated in alginate hydrogels. *IEEE T. Magn.*, 44(11):2760–2763, 2008.
- [183] MP Fernandez, DS Schmool, AS Silva, M Sevilla, AB Fuertes, P Gorria, and JA Blanco. Control of crystalline phases in magnetic Fe nanoparticles inserted inside a matrix of porous carbon. *J. Magn. Mater.*, 322:1300–1303, 2010.
- [184] S Veintemillas-Verdaguer, MP Morales, and CJ Serna. Continuous production of gamma-Fe₂O₃ ultrafine powders by laser pyrolysis. *Mater. Lett.*, 35:227–231, 1998.
- [185] RM Bozorth. *Ferromagnetism*. IEEE Press, USA, 1993.
- [186] M Zayat, F Monte, MP Morales, G Rosa, H Guerro, CJ Serna, and D Levy. Highly transparent γ -Fe₂O₃/Vycor-glass magnetic nanocomposites exhibiting Faraday rotation. *Adv. Mater.*, 15(21):1809–1812, 2003.
- [187] AR Deshpande, H Xu, and JMK Wiezorek. Effects of grain size on coercivity of combined-reaction-processed FePd intermetallics. *Acta Mater.*, 52:2903–2911, 2004.
- [188] S Wagner and A Pundt. Mechanical stress impact on thin Pd_{1-x}Fe_x film thermodynamic properties. *Appl. Phys. Lett.*, 92:051914, 2008.
- [189] SC Tjong and H Chen. Nanocrystalline materials and coatings. *Mat. Sci. Eng. R.*, 45:1–88, 2004.
- [190] JKW Wang, TS Jung, J-B Chang, RA Mickiewicz, A Alexander-Katz, CA Ross, and KK Berggren. Complex self-assembled patterns using sparse commensurate templates with locally varying motifs. *Nat. Nanotechnol.*, 5:256–260, 2010.
- [191] VP Chuang, J Gwyther, RA Mickiewicz, I Manners, and CA Ross. Templated self-assembly of square symmetry arrays from an ABC tri-block terpolymer. *Nano. Lett.*, 9(12):4363–4369, 2009.

-
- [192] K Liu, S Fournier-Bidoz, GA Ozin, and I Manners. Highly ordered magnetic ceramics nanorod arrays from a polyferrocenylsilane by nanoimprint lithography with anodic aluminium templates. *Chem. Mater.*, 21:1781–1783, 2009.
- [193] P Vukusic. Structural colour in lepidoptera. *Curr. Bio.*, 16:R621–R623, 2006.
- [194] M Srinivasarao. Nano-optics in the biological world: Beetles, butterflies, birds and moths. *Chem. Rev.*, 99(7):1935–1962, 1999.
- [195] JP Vigneron, M Rassart, Z Vértésy, K Kertész, M Sarrazin, LP Biró, D Ertz, and V Lousse. Optical structure and function of the white filamentary hair covering the edelweiss bracts. *Phys. Rev. E*, 71:011906, 2005.
- [196] AE Seago, P Brady, JP Vigneron, TD Schultz, and M Meadows. Gold bugs and beyond: a review of iridescence and structural colour mechanisms in beetles (coleoptera). *J. R. Soc. Interface*, 6:S165–S184, 2009.
- [197] M Doucet and M Meadows. Iridescence: A functional perspective. *J. R. Soc. Interface*, 6:S115–S132, 2009.
- [198] A Loyau. Iridescent structurally based colouration of eyespots correlates with mating success in the peacock. *Behav. Ecol.*, 18:1123–1131, 2007.
- [199] LP Biró, Z Bálint, K Kertész, Z Vértésy, GL Márk, ZE Hováth, J Balázs, D Méhn, I Kiricsi, V Lousse, and JP Vigneron. Role of photonic-crystal-type structures in the thermal regulation of a lycaenid butterfly sister species pair. *Phys. Rev. E*, 67:021907, 2003.
- [200] RH Douglas and NJ Marshal. A review of vertebrate and invertebrate ocular filters. In *Adaptive mechanisms in the ecology of vision*. Springer Publishing Company, 1999.
- [201] LP Biró, Z Bálint, Z Vértésy, K Kertész, GL Márk, V Lousse, and JP Vigneron. Living photonic crystals: Nanostructure of the scales of *Cyanophrys remus* butterfly. *Nanopages*, 1(2):195–208, 2006.
- [202] HM Whitney, M Kolle, P Andrew, L Chittka, U Steiner, and BJ Glover. Floral iridescence, produced by diffractive optics, acts as a cue for animal pollinators. *Science*, 323(5910):130–133, 2009.
- [203] S Yoshioka and S Kinoshita. Effect of macroscopic structure in iridescent color of the peacock feathers. *Forma.*, 17:169–181, 2002.

Physical phenomena of thin surface layers

- [204] P Vukusic. Taken from website http://newton.ex.ac.uk/research/emag/butterflies/iridescence_in_nature.html, March 2010.
- [205] H Whitney, M Kolle, R Alvarez-Fernandez, U Steiner, and B Glover. Contributions of iridescence to floral patterning. *Comm. Int. Bio.*, 2(3):230–232, 2009.
- [206] BJ Glover and HM Whitney. Structural colour and iridescence in plants: the poorly studied relations of pigment colour. *Ann. Bot.*, 105:505–511, 2010.
- [207] DW Lee, GT Taylor, and AK Irvine. Structural fruit colouration in *delarbrea michieana* (araliaceae). *Int. J. Plant Sci.*, 161:297–300, 2000.
- [208] TW Mulroy. Spectral properties of heavily glaucous and non-glaucous leaves of a succulent rosette-plant. *Oecologica*, 38:349–357, 1979.
- [209] JB Clark and GR Lister. Photosynthetic action spectra of trees. ii. the relationship of cuticle structure to the visible and ultraviolet spectral properties of needles from four coniferous species. *Plant Physiol.*, 55:407–413, 1975.
- [210] QON Kay, HS Daoud, and CH Stirton. Pigment distribution, light-reflection and cell structure in petals. *Bot. J. Linn. Soc.*, 83:57–83, 1981.
- [211] TC Volgelmann. Plant tissue optics. *Ann. Rev. Plant Phys.*, 44:231–251, 1993.
- [212] PW Richards. *The tropical rainforest*. Cambridge University Press, Cambridge, 2nd edition, 1996.
- [213] DW Lee, JB Lowry, and BC Stone. Abaxial anthocyanin layers in leaves of tropical rainforest plants - enhancer of light capture in deep shade. *Biotropica*, 11(1):70–77, 1979.
- [214] NM Hughes, TC Vogelmann, and WK Smith. Optical effects of abaxial anthocyanin on absorption of red wavelengths by understorey species: revisiting the back scatter hypothesis. *J. Exp. Bot.*, 59:3435–3442, 2008.
- [215] DW Lee. *On the economy of plant form and function*, chapter 4. Cambridge University Press, 1986.
- [216] DW Lee and JB Lowry. Physical basis and ecological significance of iridescence in blue plants. *Nature*, 254:50–51, 1975.
- [217] E Stahl. *Ann. Jard. Bot. Buitenez.*, 13:137–216, 1896.

-
- [218] G Gentner. Über den blauglanz auf blättern und früchten. *Biotropica*, 99:337–354, 1909.
- [219] DW Lee. Iridescent blue plants. *Am. Sci.*, 85:56–63, 1986.
- [220] DL Fox and JR Wells. Scemocromic leaf surfaces of selaginella. *Am. Fern. J.*, 61(3):137–144, 1971.
- [221] DW Lee and C Hébant. Ultrastructural basis and developmental control of blue iridescence in selaginella leaves. *Amer. J. Bot.*, 71(2):216–219, 1984.
- [222] RM Graham, DW Lee, and K Norstog. Physical and ultrastructural basis of blue leaf iridescence in two neotropical ferns. *Am. J. Bot.*, 80(2):198–203, 1992.
- [223] KS Gould and DW Lee. Physical and ultrastructural basis of blue leaf iridescence in four malaysian understory plants. *Am. J. Bot.*, 83(1):45–50, 1996.
- [224] PW Richards. Ecology of bryology. In *Manual of Bryology*. Cornell University Press, The Hague, 1932.
- [225] FA Bazzaz and STA Pickett. Physiological ecology of tropical succession - a comparative review. *Annu. Rev. Eco. Syst.*, 11:287–310, 1980.
- [226] RL Chazdon, RW Pearcy, DW Lee, and N Fletcher. Photosynthetic responses of tropical forest plants to contrasting light environments. In *Tropical forest plant ecophysiology*. Chapman and Hall, 1996.
- [227] M Théry. Forest light and its influence on habitat selection. *Plant Ecol.*, 153:251–261, 1998.
- [228] RE Blakenship. *Molecular mechanisms of photosynthesis*. Blackwell Science Ltd, Oxford, 2002.
- [229] MF Hipkins and NR Baker, editors. *Photosynthesis energy transduction: a practical approach*. IRL Press Limited, Oxford, 1986.
- [230] E Hecht. *Optics*. Addison Wesley, 2002.
- [231] OS Heavens. *Optical properties of thin solid films*. Dover publications inc., 1991.
- [232] PB Green and P Linstead. A procedure for sem of complex shoot structures applied to the inflorescence of snapdragon (antirrhinum). *Protoplasma*, 158:33–38, 1990.

Physical phenomena of thin surface layers

- [233] B Fultz and JM Howe. *Transmission Electron Microscopy and Diffractometry of Materials*. Springer, 3rd edition, 2008.
- [234] PR Lewis and DP Knight. *Staining methods for sectioned material*. North-Holland Publishing company, Amsterdam, 1988.
- [235] JT Woolley. Refractive index of soybean leaf cell-walls. *Plant Physiol.*, 11(2):172–174, 1975.
- [236] E Charney and FS Brackett. The spectral dependence of scattering from a spherical alga and its implications for the state of organization of the light-accepting pigments. *Arch. Biochem. Biophys.*, 92(1):1–12, 1961.
- [237] AF Huxley. A theoretical treatment of the reflexion of light by multilayer structures. *J. Exp. Bio.*, 48:227–245, 1968.
- [238] E Hecht. *Optics*. Addison Wesley, San Francisco, 2002.
- [239] S Kinoshita and S Yoshioka. Structural colours in nature: The role of regularity and irregularity in the structure. *Chem. Phys. Chem.*, 6:1442–1459, 2005.
- [240] P Vukusic, JR Sambles, CR Lawrence, and RJ Wootton. Quantified interference and diffraction in single morpho butterfly scales. *Proc. R. Soc. Lond. B*, 266:1403–1411, 1999.
- [241] DG Stavenga, S Foletti, G Palasantzas, and K Arikawa. Light on the moth-eye corneal nipple array of butterflies. *Proc. Biol. Sci.*, 273:661–667, 2006.
- [242] HA Macleod. *Thin-film optical filters*. IOP Publishing, London, 3rd edition, 2001.
- [243] DW Lee and Graham. R. Leaf optical properties of rainforest sun and extreme shade plants. *Am. J. Bot.*, 73(8):1100–1108, 1986.
- [244] R Gordon, D Losic, MA Tiffany, and SS Nagy. The glass menagerie: diatoms for novel applications in nanotechnology. *Trends Biotechnol.*, 27:116–127, 2009.
- [245] IA Abbott. On the species of iridaea (rhodophyta) from the pacific-coast of north america. *Syesis*, 4:51–72, 1972.
- [246] I Fournet, E Deslandes, and JY Floch. Iridescence - a useful criterion to sort gametophytes from sporophytes in the red alga *Chondrus crispus*. *J. Appl. Phycol.*, 5(5):535–537, 1993.

-
- [247] WH Gerwick and NJ Lang. Structural, chemical and ecological studies of iridescence in iridacea (rhodophyta). *J. Phycol.*, 13(2):121–127, 1977.
- [248] HM Whitney, M Kolle, P Andrew, L Chittka, U Steiner, and BJ Glover. Response to comment on: Floral iridescence, produced by diffractive optics acts as a cue for animal pollinators. *Science*, 325:1072, 2009.
- [249] M Stevens and S Merliaita. Defining disruptive coloration and distinguishing its functions. *Philos. T. R. Soc. B*, 364:481–488, 2009.
- [250] TN Sherratt, A Rashed, and CD Beatty. Hiding in plain sight. *Trends Eco. Evo.*, 20(8):414–416, 2005.
- [251] DW Lee, J Kelley, and JH Richards. Blue leaf iridescence as a by-product of photoprotection in tropical rainforest understory plants. Vancouver, Canada, July 2008. Botanical Society of America.
- [252] KS Gould, DN Kuhn, DW Lee, and SF Oberbauer. Why leaves are sometimes red. *Nature*, 378:241–242, 1995.
- [253] M Wada, T Murata, and M Shibata. Changes in microtubule and microfibril arrangement during polarotropism in adiantum protonemata. *Bot. Mag. Tokyo*, 103:391–401, 1990.
- [254] W Haupt. Role of light in chloroplast movement. *Bioscience*, 23(5):289–296, 1973.
- [255] W Haupt. Light mediated movement of chloroplasts. *Ann. Rev. Plant. Physiol.*, 33:205–233, 1982.
- [256] M Dacke, D-E Nilsson, EJ Warrant, AD Blest, MF Land, and DC O’Carroll. Built-in polarizers form part of a compass organ in spiders. *Nature*, 410:470–473, 1999.
- [257] N Shashar, TW Cronin, LB Wolff, and MA Condon. The polarization of light in a tropical rainforest. *Biotropica*, 30(2):275–285, 1998.
- [258] LB Wolff. Polarization-based material classification from specular reflection. *IEEE T. Pattern Anal.*, 12(10):1059–1071, 1990.

List of Publications

Wetting induced instabilities in miscible polymer blends. K. R. Thomas, N. Clarke, R. Poetes, M. Morariu, U. Steiner. **Soft Matter** 6: 3517–3523, 2010.

Function of blue iridescence in tropical understory plants. K. R. Thomas, M. Kolle, H. M. Whitney, B.J. Glover, U. Steiner. **J. R. Soc. Interface** 7:1699-1707, 2010.

Magnetic properties of ceramics from the pyrolysis of Polyferrocenylethylmethylsilane films doped with palladium nanoparticles and palladium(II) acetylacetonate.

K. R. Thomas, A. Ionescu, J. Gwyther, I. Manners, C. H. W. Barnes, U. Steiner, E. Sivaniah. **Submitted.**

Non-equilibrium behaviour of thin polymer films. K. R. Thomas, A. Chenneviere, G. Reiter, U. Steiner. **In preparation.**